

REPORT DOCUMENTATION PAGE			Form Approved OMB NO. 0704-0188		
<p>The public reporting burden for this collection of information is estimated to average 1 hour per response, including the time for reviewing instructions, searching existing data sources, gathering and maintaining the data needed, and completing and reviewing the collection of information. Send comments regarding this burden estimate or any other aspect of this collection of information, including suggestions for reducing this burden, to Washington Headquarters Services, Directorate for Information Operations and Reports, 1215 Jefferson Davis Highway, Suite 1204, Arlington VA, 22202-4302. Respondents should be aware that notwithstanding any other provision of law, no person shall be subject to any penalty for failing to comply with a collection of information if it does not display a currently valid OMB control number.</p> <p>PLEASE DO NOT RETURN YOUR FORM TO THE ABOVE ADDRESS.</p>					
1. REPORT DATE (DD-MM-YYYY) 22-07-2014		2. REPORT TYPE Ph.D. Dissertation		3. DATES COVERED (From - To) -	
4. TITLE AND SUBTITLE SYNTHESIS AND FUNCTIONALIZATION OF ATOMIC LAYER BORON NITRIDE NANOSHEETS FOR ADVANCED MATERIAL APPLICATIONS			5a. CONTRACT NUMBER W911NF-13-1-0138		
			5b. GRANT NUMBER		
			5c. PROGRAM ELEMENT NUMBER 206022		
6. AUTHORS Muhammad Sajjad			5d. PROJECT NUMBER		
			5e. TASK NUMBER		
			5f. WORK UNIT NUMBER		
7. PERFORMING ORGANIZATION NAMES AND ADDRESSES University of Puerto Rico at Rio Piedras P. O. Box 21790  San Juan, PR 00931 -1790			8. PERFORMING ORGANIZATION REPORT NUMBER		
9. SPONSORING/MONITORING AGENCY NAME(S) AND ADDRESS (ES) U.S. Army Research Office P.O. Box 12211 Research Triangle Park, NC 27709-2211			10. SPONSOR/MONITOR'S ACRONYM(S) ARO		
			11. SPONSOR/MONITOR'S REPORT NUMBER(S) 62826-MS-REP.8		
12. DISTRIBUTION AVAILABILITY STATEMENT Approved for public release; distribution is unlimited.					
13. SUPPLEMENTARY NOTES The views, opinions and/or findings contained in this report are those of the author(s) and should not be construed as an official Department of the Army position, policy or decision, unless so designated by other documentation.					
14. ABSTRACT Besides graphene, hexagonal boron nitride nanosheets (BNNSs) are playing an excellent role for the next generation of 2-dimensional (2D) functional nanomaterials. Due to the similar lattice parameter and identical crystalline structure to that of graphene, BNNSs are often known as white graphene. These nanosheets exhibit several unique properties that make them preferable to graphene in some ways. Unlike graphene, there was no established method for obtaining large scale of single- or few-layer BNNSs.					
15. SUBJECT TERMS synthesis, functionalization, BN, application					
16. SECURITY CLASSIFICATION OF:			17. LIMITATION OF ABSTRACT UU	15. NUMBER OF PAGES	19a. NAME OF RESPONSIBLE PERSON Peter Feng
a. REPORT UU	b. ABSTRACT UU	c. THIS PAGE UU			19b. TELEPHONE NUMBER 787-764-0000

## Report Title

# SYNTHESIS AND FUNCTIONALIZATION OF ATOMIC LAYER BORON NITRIDE NANOSHEETS FOR ADVANCED MATERIAL APPLICATIONS

## ABSTRACT

Besides graphene, hexagonal boron nitride nanosheets (BNNSs) are playing an excellent role for the next generation of 2-dimensional (2D) functional nanomaterials. Due to the similar lattice parameter and identical crystalline structure to that of graphene, BNNSs are often known as white graphene. These nanosheets exhibit several unique properties that make them preferable to graphene in some ways. Unlike graphene, there was no established method for obtaining large scale of single- or few-layer BNNSs.

In our current research, we installed and upgraded CO<sub>2</sub>-pulsed laser plasma deposition system and introduced new experimental parameters in order to achieve large amount of high quality, few atomic layers BNNSs at significantly low substrate temperature down to 300 oC and at short interval of deposition time (e.g. 3-5 sec). With the variation of deposition parameters such as using H<sub>2</sub> gas as deposition environment, we controlled the thicknesses of nanosheets down to 1.5 nm, while quality and purity of the sample were still very high. Moreover, the depositions performed in H<sub>2</sub> environment effectively prevented nanosheets from sputtering through high energy boron (B) and nitrogen (N) ions, as result, large amount of single-crystal and polycrystalline nanosheets were obtained. The size, shape, thickness, density, and alignment of the BNNSs were well-controlled by appropriately changing the deposition conditions. TEM images showed large area, flat and transparent BNNSs while, high resolution transmission electron microscopy (HRTEM) showed the sheets to be mostly defect-free and to have the characteristic honeycomb crystal lattice structure based on six-membered B<sub>3</sub>-N<sub>3</sub> hexagon. From HRTEM measurements, one can clearly distinguish between the bright and slightly dull dots related to B and N atoms arranged in a typical honeycomb network structure, similar to C-C atoms in graphene. HRTEM, electron diffraction, X-ray diffraction, Raman scattering, fast Fourier transform and Fourier transform infrared spectroscopy clearly identified hexagonal BN (h-BN).

Leading BNNSs towards advanced material applications, we investigated how nanostructuring of composite BNNSs can be used to provide new electronic and optical functionalities. We focused on three different areas of nano-electronic device technology, e.g. fabrication of BNNSs-based prototype Schottky diode, deep ultraviolet (DUV) photo detector and resistance based gas sensor. Doping with carbon elements functionalized BNNSs and current versus voltage (I-V) characteristics of Schottky diode were recorded at different temperatures (25 oC, 50 oC, 75 oC) which represented slight doping into BNNSs brought a significant change in the output current of diode. BNNSs were also treated with hydrogen plasma, which exhibit distinct and pronounced changes in its electronic properties after the plasma treatment. The band-gaps of the few layers BNNSs reduced from ~5.6 eV (at 0 s without hydrogen treatment) to 4.25 eV (at 250s with hydrogen treatment), which is a signature of transition from the insulating to the semi-conductive regime. It was concluded that with the engineering of 2D materials by attaching other atoms or molecules significantly changes their electronic properties.

Data obtained from BNNSs-based DUV photo-detector device indicates that BNNSs are highly sensitive to deep UV light source. Response time and recover time are around 5s and 150s, respectively. Actual response time and recover time should be shorter because time delay for reaching full intensity for UV lamps after switch on lamp, or florescence after switch off the lamp affects the measurement results. Gas sensing properties of BNNSs-based gas sensor indicated that BNNSs are truly an effective material that can be used as resistance based gas sensor operates in extreme high temperature and toxic environment where properties of conventional sensors fall short. It is therefore concluded that BNNSs are highly attractive for range of applications in material science and nano-electronic device technology.

Similar to diamond like carbon, BN is also fashionable in cubic structure. To synthesize cubic BN (c-BN), high temperature and high pressure condition are required. Synthesis at low temperature and low pressure was a challenge. In our study, we synthesized cubic BN at significantly low substrate temperature (450 oC) using ferrous oxide nanoparticles as catalyst. While by using nickel and cobalt nano-particles as catalyst helped in producing BN nanotubes.

**UNIVERSITY OF PUERTO RICO  
RIO PIEDRAS CAMPUS  
NATURAL SCIENCES FACULTY  
DOCTORAL PROGRAM IN CHEMICAL PHYSICS**

**SYNTHESIS AND FUNCTIONALIZATION OF ATOMIC LAYER BORON NITRIDE  
NANOSHEETS FOR ADVANCED MATERIAL APPLICATIONS**

By

Muhammad Sajjad

A thesis submitted in partial fulfillment of the requirements for the degree of  
Doctor of Philosophy

June 5, 2014

# **SYNTHESIS AND FUNCTIONALIZATION OF ATOMIC LAYER BORON NITRIDE NANOSHEETS FOR ADVANCED MATERIAL APPLICATIONS**

Accepted by the Faculty of the Doctoral Program in Chemical Physics  
of the University of Puerto Rico in partial fulfillment of the  
requirements for the degree of

Doctor of Philosophy

---

Dr. Peter X. Feng  
Professor of the Department of Physics  
Thesis Advisor

---

Dr. Gerardo Morell  
Professor of the Department of Physics  
Thesis Committee Member

---

Dr. Chen Zhongfang  
Professor of the Department of Chemistry  
Thesis Committee Member

June 5, 2014

## **DEDICATION**

This thesis is dedicated to my family, particularly to my mother for her great support, love patience and understanding. Also this thesis is dedicated to my father (late) from who I learned to achieve goals in life.

## Table of Contents

<b>Acknowledgement</b> .....	vii
<b>Abstract</b> .....	ix
<b>List of Figures</b> .....	xii
<b>List of Tables</b> .....	xv
<b>Chapter 1 Introduction and Motivation</b> .....	<b>1</b>
1.1 Introduction and Motivation.....	1
1.2 Low Dimensional BN Nanostructures.....	3
1.3 Carbon and BN Nanostructures.....	5
1.4 Monolayer Boron Nitride; Analogue of Graphene.....	6
1.5 Boron Nitride Solid State Phase.....	9
1.6 Energy Band Gap Modification in BNNSs.....	10
1.7 Applications of BNNSs.....	11
1.7.1 BNNSs-based Deep UV Photo Detector.....	12
1.7.2 BNNSs-based Schottky Diode.....	13
1.7.3 Gas Sensing Properties of BNNSs.....	17
1.8 Boron Nitride Nanosheets Science Developed in this Thesis.....	18
1.9 Overview of Dissertation.....	19
1.10 References.....	21
<b>Chapter 2 Synthesis and Characterization Techniques</b> .....	<b>25</b>
2.1 Introduction.....	25
2.2 Chemical Vapor Deposition Method .....	26
2.3 Sputtering Technique.....	26
2.4 Pulsed Laser Deposition Technique.....	28
2.5 Installation of CO <sub>2</sub> -Pulsed Laser Plasma Deposition System.....	29
2.5.1 Experimental Parameters.....	30
2.5.1.1 Substrate to Target Distance.....	31
2.5.1.2 Angle of Incidence.....	32
2.5.1.3 Substrate Holder.....	32
2.6 Crystalline Structure Analysis.....	33
2.7 Other Characterization Techniques (SEM, TEM, AFM, Raman, FT-IR, XRD, XPS, SAED).....	34
2.8 Additional Related Techniques and Experiments.....	35
2.8.1 Optical and Electrical Characterizations.....	35
2.8.1.1 Cathodoluminescence Spectroscopy.....	36
2.8.1.2 Field Emission Characteristics.....	37
2.9 Conclusion.....	38
2.10 References.....	39
<b>Chapter 3 Synthesis and Electron Microscopic Characterization of BNNSs</b> .....	<b>41</b>
3.1 Single crystal and Polycrystalline BNNSs.....	41

3.2	Effect of Deposition Environment in the Synthesis of BNNSs.....	42
3.3	Results.....	45
3.3.1	Electron Microscope Results.....	45
3.3.2	TEM and SAED Results.....	46
3.3.3	XRD Results.....	48
3.3.4	Raman Results.....	48
3.3.5	FT-IR Results.....	49
3.3.6	EDS Results.....	50
3.3.7	XPS Analysis of BNNSs.....	51
3.3.8	Mechanism for the Formation of BNNSs.....	52
3.3.9	Vertically Aligned BNNSs.....	54
3.4	Conclusion.....	55
3.5	References.....	57
<b>Chapter 4</b>	<b>Nanoscale Structure Study of BNNSs.....</b>	<b>59</b>
4.1	Layered Structure Characterization of BNNSs by TEM.....	59
4.2	Nanoscale Structure Study of BNNSs.....	61
4.2.1	Monolayer BNNS.....	62
4.2.2	SAED and FFT Pattern of Monolayer BNNS.....	64
4.2.3	Nanoscale Structure of Single BNNS.....	64
4.2.4	Thickness of Single BNNS.....	65
4.2.5	Thickness of Multilayer BNNSs.....	66
4.2.6	Wrinkles in BNNSs.....	67
4.2.7	Knock on Damage in BNNSs.....	68
4.3	Conclusion.....	70
4.4	References.....	71
<b>Chapter 5</b>	<b>Applications of BNNSs.....</b>	<b>72</b>
5.1	Electronic Applications.....	72
5.1.1	Development of BNNSs-Based Prototype Schottky Diode.....	73
5.1.2	I-V Characteristics of Carbon Doped BNNSs-Based Schottky Diode.....	74
5.1.3	Effect of Temperature in the I-V Characteristics of Schottky Diode.....	75
5.2	Hydrogen Plasma Modification in BNNSs.....	76
5.2.1	I-V Characteristics of Surface Modified BNNSs.....	78
5.2.2	Sideways and Top Down Measurements of I-V Characteristics.....	79
5.2.3	I-V Measurements of BNNSs/ Mo and BNNSs/AlN.....	81
5.2.4	Resistivity Calculations.....	83
5.2.5	Effect of Temperature on I-V Characteristics of BNNSs/AlN.....	84
5.2.6	Effects of Temperatures on Resistivity of BNNSs of Different Thickness...	85
5.3	Optical Measurements of BNNSs.....	86
5.3.1	Cathodoluminescence Spectroscopy of BNNSs.....	86
5.3.2	Fabrication of DUV Photo Detector.....	89

5.3.3	Sensitivity of DUV Photo Detector.....	92
5.3.4	BNNSs/Mo and BNNSs/Si based Prototypic DUV Photo Detectors .....	92
5.3.5	DUV Detector based on Thin BNNSs.....	93
5.3.6	DUV Detector based on Thick BNNSs.....	95
5.4	Gas Sensing Properties of BNNSs.....	96
5.5	Field Emission Characteristics of BNNSs.....	99
5.6	Conclusion.....	102
5.7	References.....	104
<b>Chapter 6</b>	<b>Other Research Developed in This Thesis .....</b>	<b>106</b>
6.1	Introduction.....	106
6.2	Preparation of Catalyst for the Synthesis of c-BN Films.....	107
6.3	Experimental Conditions.....	108
6.4	Low temperature synthesis of c-BN films.....	108
6.4.1	SEM and TEM Results.....	108
6.4.2	Raman, XRD and FT-IR Spectroscopy of c-BN Films.....	110
6.4.3	Elemental Analysis in c-BN Films.....	112
6.5	Synthesis Techniques for 1D Nanostructures .....	113
6.6	Experimental Conditions Applied.....	114
6.7	Nanostructures Characterizations.....	114
6.7.1	BN Nanowires.....	115
6.7.2	BN Nanorods.....	116
6.7.3	BNNTs.....	117
6.8	Effect of Experimental Parameters in the Synthesis of BN Nanostructures .....	118
6.8.1	Effect of Substrate Temperature.....	118
6.8.2	Substrate Material Effect.....	120
6.9	Other Characterizations.....	121
6.9.1	Raman Spectroscopy of BN Nanorods.....	121
6.9.2	XRD Analysis .....	124
6.9.3	EDS Spectroscopy.....	125
6.10	Conclusion.....	126
6.11	References.....	127
<b>Chapter 7</b>	<b>Summary and Future Work.....</b>	<b>129</b>
7.1	Summary of Contributions.....	129
7.1.1	Synthesis Ultrathin Boron Nitride Nanosheets.....	129
7.2	Future work.....	132
7.2.1	Overview.....	132
7.2.2	Existing Research.....	134
7.3	Closing Remarks.....	136
7.4	References.....	137



## **Acknowledgements**

First of all, thanks to Almighty Allah with His help I completed my PhD research.

I would like to give very special thanks to my thesis advisor and mentor Dr. Peter X. Feng, who offered me an opportunity to start doctoral study and the current research, for the constant supports and guidance throughout my Ph.D study.

I would also like to appreciate Professor Gerardo Morell and Professor Chen Zhongfang for generously serving as the members of his thesis committee and for correcting his research proposal, thesis, and valuable suggestions. Thanks to Professor Brad Weiner and Professor Gerardo Morell, on providing plenty of support during my Ph.D study, such as the electron field emission experiment. Thanks to Dr. Vladimir Makarov for his assistance in laser system and Dr. Zhang for his valuable suggestions and help in choosing graduate courses at the beginning of my graduate study. Thanks to Professor Antonio Martinez and Professor Luis F. Fonseca for their kind instructions in the enrollment process of graduate courses during the entire Ph.D study.

Thanks also go to the personnel of the Department of Physics, the Resource Center for Science and Engineering and the Decanato de Estudios Graduados e Investigacion, especially Ms. Ileana Desiderio, Marilyn Rodriguez, Karem Camacho, Maria Vargas and Josefa Font for doing all the paperwork regarding academic matters, purchase orders of scientific equipment, and scholarship matters.

Thank to lab fellow, friends, and the staff from Materials Characterization Center and IFN facility, for SEM and TEM measurements.

Finally, I would like to thank to all my family members particularly my mother for her great support, love, patience and understanding during my years of PhD study.

The financial supports through NSF-EPSCoR, DEGI-FIPI for two years, DEGI-PEAF Merit Scholarship for one year, are of great help in making the thesis possible.

## Abstract

Besides graphene, hexagonal boron nitride nanosheets (BNNSs) are playing an excellent role for the next generation of 2-dimensional (2D) functional nanomaterials. Due to the similar lattice parameter and identical crystalline structure to that of graphene, BNNSs are often known as white graphene. These nanosheets exhibit several unique properties that make them preferable to graphene in some ways. Unlike graphene, there was no established method for obtaining large scale of single- or few-layer BNNSs.

In our current research, we installed and upgraded CO<sub>2</sub>-pulsed laser plasma deposition system and introduced new experimental parameters in order to achieve large amount of high quality, few atomic layers BNNSs at significantly low substrate temperature down to 300 °C and at short interval of deposition time (e.g. 3-5 sec). With the variation of deposition parameters such as using H<sub>2</sub> gas as deposition environment, we controlled the thicknesses of nanosheets down to 1.5 nm, while quality and purity of the sample were still very high. Moreover, the depositions performed in H<sub>2</sub> environment effectively prevented nanosheets from sputtering through high energy boron (B) and nitrogen (N) ions, as result, large amount of single-crystal and polycrystalline nanosheets were obtained. The size, shape, thickness, density, and alignment of the BNNSs were well-controlled by appropriately changing the deposition conditions. TEM images showed large area, flat and transparent BNNSs while, high resolution transmission electron microscopy (HRTEM) showed the sheets to be mostly defect-free and to have the characteristic honeycomb crystal lattice structure based on six-membered B<sub>3</sub>-N<sub>3</sub> hexagon. From HRTEM measurements, one can clearly distinguish between the bright and slightly dull dots related to B and N atoms arranged in a typical honeycomb network structure, similar to C-C atoms in graphene. HRTEM, electron diffraction, X-ray diffraction, Raman scattering, fast

Fourier transform and Fourier transform infrared spectroscopy clearly identified hexagonal BN (*h*-BN).

Leading BNNSs towards advanced material applications, we investigated how nanostructuring of composite BNNSs can be used to provide new electronic and optical functionalities. We focused on three different areas of nano-electronic device technology, e.g. fabrication of BNNSs-based prototype Schottky diode, deep ultraviolet (DUV) photo detector and resistance based gas sensor. Doping with carbon elements functionalized BNNSs and current versus voltage (I-V) characteristics of Schottky diode were recorded at different temperatures (25 °C, 50 °C, 75 °C) which represented slight doping into BNNSs brought a significant change in the output current of diode. BNNSs were also treated with hydrogen plasma, which exhibit distinct and pronounced changes in its electronic properties after the plasma treatment. The band-gaps of the few layers BNNSs reduced from ~5.6 eV (at 0 s without hydrogen treatment) to ~4.25 eV (at 250s with hydrogen treatment), which is a signature of transition from the insulating to the semi-conductive regime. It was concluded that with the engineering of 2D materials by attaching other atoms or molecules significantly changes their electronic properties.

Data obtained from BNNSs-based DUV photo-detector device indicates that BNNSs are highly sensitive to deep UV light source. Response time and recover time are around 5s and 150s, respectively. Actual response time and recover time should be shorter because time delay for reaching full intensity for UV lamps after switch on lamp, or florescence after switch off the lamp affects the measurement results. Gas sensing properties of BNNSs-based gas sensor indicated that BNNSs are truly an effective material that can be used as resistance based gas sensor operates in extreme high temperature and toxic environment where properties of

conventional sensors fall short. It is therefore concluded that BNNSs are highly attractive for range of applications in material science and nano-electronic device technology.

Similar to diamond like carbon, BN is also fashionable in cubic structure. To synthesize cubic BN (c-BN), high temperature and high pressure condition are required. Synthesis at low temperature and low pressure was a challenge. In our study, we synthesized cubic BN at significantly low substrate temperature (450 °C) using ferrous oxide nanoparticles as catalyst. While by using nickel and cobalt nano-particles as catalyst helped in producing BN nanotubes.

## List of Figures

<b>Figure 1.1</b> Schematics of (a) Carbon pencil, (b) graphene layers, and (c) BNNSs; a comparison between the graphene and the BNNSs.....	2
<b>Figure 1.2</b> Structural model for low dimensional BNNSs: (a) a piece of BN nanosheet, (b) BN nanoribbons, (c) nanotube, and (d) fullerene type BN nanoballs.....	4
<b>Figure 1.3</b> A Schematic illustrates the structure similarity between the carbon nanostructures and the boron nitride nanostructures.....	5
<b>Figure 1.4</b> Schematic of BN monolayer.....	8
<b>Figure 1.5</b> Schematic of c-BN Structure.....	9
<b>Figure 1.6</b> (a) Schematic of doped single layer BNNS, (b) hybridized BNNSs structures with carbon elements.....	11
<b>Figure 1.7</b> I-V characteristics of graphene placed on SiO <sub>2</sub> and BNNSs.....	12
<b>Figure 1.8</b> A typical symbol of a Schottky diode.....	13
<b>Figure 1.9</b> Schottky barrier formation on p-type semiconductor. Top: isolated charge-neutral bulk materials. Center: dipole layer formed as materials interact; Fermi level difference is reduced. Bottom: final configuration following charge transfer to reach equilibrium with no applied voltage. The neutral (shaded) region in the semiconductor moves away from the interface, leaving a charged depletion region (unshaded) near the interface.....	16
<b>Figure 1.10</b> The superb class of nanosystem explored in this thesis is the atomic thin sheet of boron nitride. a) An artistic rendition of the single boron nitride layer. b) TEM image of experimentally obtained BNNSs transferred on a lacey carbon grid. Such nanosheets are obtained by the method developed in this thesis.....	19
<b>Figure 2.1</b> Schematic of the sputtering process for nano-materials deposition.....	27
<b>Figure 2.2</b> (a) photograph of the CO <sub>2</sub> -PLD installed in our laboratory, b) inside view of deposition chamber, c) schematic illustration of the deposition mechanism, and d) photograph of plasma plume formed in our CO <sub>2</sub> -PLD system.....	31
<b>Figure 2.3</b> Schematic diagram of the cathodoluminescence process.....	36
<b>Figure 2.4</b> Illustration of field electron emission from a tip.....	38
<b>Figure 3.1</b> Synthesis of BNNSs at different atmosphere, (a) in vacuum, (b) in H <sub>2</sub> respectively.....	43
<b>Figure 3.2</b> SEM images recorded from samples (a) S <sub>1</sub> and (b) S <sub>4</sub> .....	45
<b>Figure 3.3</b> TEM images of BNNSs recorded from sample S <sub>1</sub> (a) and sample S <sub>4</sub> (b). The insets show electron diffraction patterns, indexed to <i>h</i> -BN. A HRTEM image recorded from a BNNSs of sample S <sub>4</sub> is shown in (c) where the hexagonal structure is clearly visible: the inset is a FFT also indexed to <i>h</i> -BN. Using HRTEM images for synthesized samples in vacuum (d) and hydrogen (e) atmospheres, the thicknesses of the BNNSs clusters were measured and the statistical results are displayed in (f, vacuum) and (g, hydrogen).....	47

<b>Figure 3.4</b> A comparison of XRD patterns recorded from BNNSs (a) S <sub>4</sub> and S <sub>1</sub> , (b) S <sub>5</sub> and S <sub>2</sub> , (c) S <sub>6</sub> and S <sub>3</sub> .....	48
<b>Figure 3.5</b> A comparison of Raman spectra recorded from samples (a) S <sub>4</sub> and S <sub>1</sub> , (b) S <sub>5</sub> and S <sub>2</sub> , (c) S <sub>6</sub> and S <sub>3</sub> .....	49
<b>Figure 3.6</b> A comparison of FT-IR spectra of BNNSs (a) S <sub>1</sub> and S <sub>4</sub> , (b) S <sub>2</sub> and S <sub>5</sub> (c) S <sub>3</sub> and S <sub>6</sub> .....	50
<b>Figure 3.7</b> EDS spectrum of BNNSs.....	50
<b>Figure 3.8</b> (a) XPS spectra of BNNSs samples prepared in Vacuum (Si/V, Mo/V, AlN/V) and H <sub>2</sub> (Si/H, Mo/H, AlN/H) environment respectively.....	51
<b>Figure 3.9</b> (a,b) SEM images of horizontally and partially vertically aligned BNNSs. (c) AFM micrographs; indicating vertically aligned BNNSs. Scalar bars are shown on images...	55
<b>Figure 4.1</b> Electron microscopic images of BNNSs, (a) SEM, (b) TEM, (c,d) magnified TEM images of the edge of nanosheet. (e) ED pattern of BNNSs. The scalar bars are shown on the image.....	60
<b>Figure 4.2</b> (a-d) HRTEM images of nanoscale structured BNNSs.....	62
<b>Figure 4.3</b> (a) Experimentally obtained single layer BNNS, (b) Magnified HRTEM image.....	63
<b>Figure 4.4</b> (a) SAED and (b) FFT pattern of BNNSs; clearly identifying hexagonal structure.....	64
<b>Figure 4.5</b> (a-d) HRTEM images of BNNSs with slight aberrations at different locations. ....	65
<b>Figure 4.6</b> (a,b) HRTEM images of the edge of BNNSs indicating few layer thickness.	66
<b>Figure 4.7</b> Morphology of atomic BNNSs. (a-c) TEM images of the surface of a single-, double-, and multi- BN sheets. (d-f) HRTEM images of the edge of the nanosheets. Scale bars are shown on the images.....	67
<b>Figure 4.8</b> (a-d) HRTEM images of BNNSs with different magnifications.....	68
<b>Figure 4.9</b> Morphology change in atomic BNNSs during TEM measurement (a) before and (b) after beam. Time between the images is 8 s. Also visible in the sequence is the generation of vacancies within the single-layer BNNS membrane. (c-d) Topological defects are incorporated during this edge reconstruction. On the other edge of the same hole, atoms are removed by the electron beam. Scale bars shown on the images are 1 nm. ....	69
<b>Figure 4.10</b> Scanning TEM images recorded from BNNSs at 30 kV using TED (in the SEM) for the samples (a) S <sub>1</sub> and (b) S <sub>4</sub> , respectively.....	70
<b>Figure 5.1</b> (a) Schematic illustration of BNNSs segment with a large amount of gaps over substrate, (b) heavily overlapped BNNSs.....	73
<b>Figure 5.2</b> Block diagram of the device prepared to analyze the characteristics of BNNSs-based Schottky diode.....	73
<b>Figure 5.3</b> I-V characteristics of BNNSs-based Schottky diode at room temperature...	75
<b>Figure 5.4</b> Effect of temperature on I-V characteristics of Schottky diode based on (a) un-doped BNNSs, (b) doped BNNSs.....	76

<b>Figure 5.5</b> (a) In situ measurement of resistance of the BNNSs with hydrogen plasma treatment as a function of time. Inset: illustration of the setup for measuring the electronic properties of BNNSs. (b) Logarithm of the electric conductivity of BNNSs plotted against the reciprocal temperature during hydrogen plasma treatment. The scale bars in the inset of a are 5 $\mu\text{m}$ .	78
<b>Figure 5.6</b> I–V characteristics of a hydrogen plasma-treated h-BN membranes measured at room temperature, 100 $^{\circ}\text{C}$ and 200 $^{\circ}\text{C}$ , respectively. Inset: Temperature dependence of the I–V characteristics before plasma. From bottom to top: T = 200 $^{\circ}\text{C}$ , 100 $^{\circ}\text{C}$ , and room temperature.	79
<b>Figure 5.7</b> Typical I-V properties of different thickness of BNNSs characterized from (a) longitudinal and (b) transversal directions. <b>Th</b> : thickness, <b>I</b> : electrical current; and <b>R</b> : resistance of the samples.	81
<b>Figure 5.8</b> Experimental setup for characterization of electrical properties of BNNSs on Mo (a) and AlN (b), respectively, typical I-V properties of BNNSs with (a1) membrane thickness of 7 nm and (a2) 30 nm on Mo substrates, and with membrane thickness of (b1) 2 nm and (b2) 30 nm on AlN substrates at different temperature.	82
<b>Figure 5.9</b> Effects of temperatures on resistivity of different thickness (a11) and (a21) of BNNSs characterized using setup (Fig. 5.8a), and (a11) and (a21) by using setup (Fig. 5.8b), respectively.	86
<b>Figure 5.10</b> CL spectrum of BNNSs excited by electron accelerated with 6 keV at 300 K. Inset shows comparison between normalized deep UV CL spectra of BNNSs measured at 12 K (a) and 300 K (b). Vertical arrows indicate excitonic recombination peaks and a deep level related emission band centered at 270 nm, respectively.	89
<b>Figure 5.11</b> (a) A photograph of the setup installed for DUV measurements. (b) Assembly of a four-pin detector probe/system, (c) A diagram of electrical circuit used for DUV tests, (d) Typical responses of a BNNSs-based DUV-photo detector prototype under selected UV photos radiation.	90
<b>Figure 5.12</b> (a-c) Schematics for different electronic setup used to collect DUV data...	93
<b>Figure 5.13</b> Response curves for, (a) BNNSs/Si DUV detector and (b) BNNS/Mo-based DUV detectors are cycled between “on” and “off” 254 nm UV light source. Comparison made between the responses of the detectors based on (c) fresh BNNSs samples and (d) 6-months old BNNSs samples.	95
<b>Figure 5.14</b> Response of BNNSs-based gas sensor to, (a) O and, (b) CH <sub>4</sub> gas.	99
<b>Figure 5.15</b> Field emission characteristics of BNNSs emission current density (a) and F-N plot of nanosheets (b).	101
<b>Figure 6.1</b> c-BN films synthesized on S <sub>1</sub> , S <sub>2</sub> and S <sub>3</sub> substrate; (a-c) SEM cross sectional view, (d-f) top view SEM micrographs. The scalar bars are shown on the images.	110
<b>Figure 6.2</b> (a-c) Raman spectra (d-f) X-Ray diffraction patterns and (g-i) FTIR spectra of c-BN films synthesized on S <sub>1</sub> , S <sub>2</sub> and S <sub>3</sub> substrates, respectively.	112
<b>Figure 6.3</b> EDS spectrum of c-BN film prepared on S <sub>3</sub> substrate.	113

<b>Figure 6.4</b> SEM micrographs of BN nanowires synthesized on Si substrates (a) at 550 °C (b) at 650 °C. The scale bars are shown as 1 μm for deposition at 550 °C and 20 μm for the deposition at 650 °C substrate temperatures.....	116
<b>Figure 6.5</b> SEM micrographs of BN nanorods synthesized on Si substrates (a) at 550 °C and (b) at 650 °C. The scale bars are shown as 1 μm for deposition at 550 °C and 20 μm for the deposition at 650 °C substrate temperatures.....	117
<b>Figure 6.6</b> (a) SEM images of BN nanotubes synthesized on Si substrate at 300 °C substrate temperatures, (b) magnified SEM image of BNNTs. (c,d) corresponding TEM and magnified TEM images of BNNTs.....	118
<b>Figure 6.7</b> SEM micrograph of BN nanostructure on Mo substrate at (a) 400 °C and (b) at 500 °C and (c) at 600 °C. The scale bars are 1 μm.....	120
<b>Figure 6.8</b> Raman spectroscopy of BN nanostructure at (a) 400 °C, (b) 500 °C, and (c) 600 °C, respectively. (d) The peak intensity ratio ( $I_{cBN}/I_{hBN}$ ) as a function of substrate temperature.....	122
<b>Figure 6.9</b> X-Ray diffraction pattern of BN nanostructure on Mo substrate (a) at 500 °C (b) at 600 °C.....	125
<b>Figure 8.1</b> Schematics illustration of graphene on BNNS. ....	133
<b>Figure 8.2</b> I-V characteristics of graphene placed on SiO <sub>2</sub> and BNNSs.....	135
<b>Figure 8.3</b> (a) Schematic of SSP–LPP technique. (b) Electron microscopic images of BNNSs prepared by PLD technique.....	135

## List of Tables

<b>Table-I</b> Summary of the experimental conditions under which the CO <sub>2</sub> -PLD was carried out.....	42
---	----



# Chapter 1

## Introduction and Motivation

### 1.1 Introduction and Motivation

Discovery of graphene [1] has brought a new revolution in the material science due to its many charming, unusual properties and practical applications in nano-electronic device technology [2-6]. This stimulated the interest in atomically thin sheets of other 2D layers materials e.g. silicon carbide, molybdenum disulfide, tungsten disulfide, tungsten diselenide, molybdenum diselenide, and hexagonal-BNNSs. Due to crystalline structure similarity to that of graphene, BNNSs has been considered the most prominent member of the family of 2D layered materials [1]. BNNSs are 2D wide band gap semiconductor material fashionable in hexagonal structure solely made of alternating boron (B) and nitrogen (N) atoms which construct a characteristic honey-comb network of  $B_3-N_3$  hexagon [7,8]. The B and N atoms are bound by covalent bonds ( $sp^2$  bonds), whereas weak van der Waals forces hold the layers together. The inter-planar spacing between two consecutive layers is 0.334 nm which is very close to that of graphene (0.333 nm) while with in a layer, the bond length between two consecutive B and the N atoms is 1.44 Å as shown in Fig. 1. Due to crystal structure similarity of BNNSs to that of graphene; this material can possess enormous potential in the development of complementary electronic and composite devices. For example, BNNSs have been considered ideal dielectric and substrate material to graphene-based nano-electronic devices because it has an atomically smooth surface that is relatively free of dangling bonds and charge traps [9]. The excellent

thermal and chemical stability, and superb resistance to oxidation properties, soon lead this material to the new applications in high performance functional nano-electronic devices.

The intra-layer interactions between the layers of a single BNNS are often well characterized. These inter-layer interactions are determined by a delicate balance between dispersion forces, electrostatic interactions and Pauli repulsions. Understanding the relative contribution of each of these interactions to the inter-layer binding is therefore essential for the characterization of their mechanical, electronic, and electromechanical properties and for the design of new materials with desired functionality.

Figure 1.1 describes an example of carbon pencil indicating similarity between the graphene and BNNSs. If we slide the tip of carbon pencil on the piece of a paper, we can see the gray color line. The microscopic analysis of the line can show us large number of carbon sheets stacked on top of one another. Within the sheets, carbon atoms are bonded with  $Sp^2$  bonding while weak Vander wall force holds the layer together. When we slide the tip of pencil on paper, due to friction weak bonding between the carbon sheets breaks and layers goes on the paper.

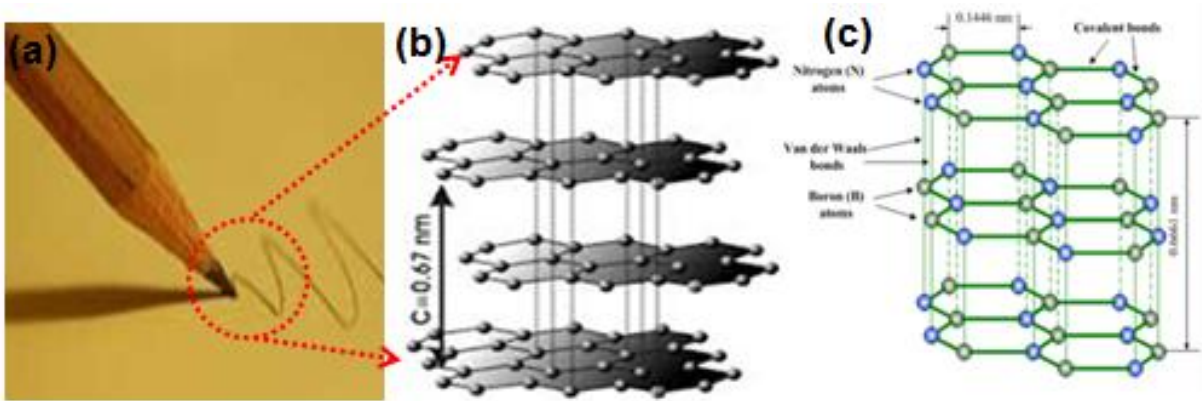


**Figure 1.1** Schematics of (a) Carbon pencil, (b) graphene layers, and (c) BNNSs; a comparison between the graphene and the BNNSs.

In BNNSs, adjacent sheets differ in stacking sequences of atomic planes with respect to C atoms in few layers graphene as shown in Fig. 1.1. In general, electron deficient B atoms are located directly above or beneath corresponding electron-rich N atoms, whereas in graphite, hexagons are offset and alternating C atoms lie above and beneath hexagon centers. The ionic nature of the B–N bond results in ABAB stacking geometry. The interlayer attractive forces are mediated by pseudo delocalized out-of-plane  $\pi$  orbital and weak van der Waals interactions as stated earlier. This highly stable and mechanically strong structure exhibits extremely high chemical stability and resistance to oxidation until temperatures of over 800 °C, thus making BNNSs highly attractive for a range of applications in the bulk phase where chemical stability and structural integrity are demanded. It is therefore particularly challenging to initiate chemical reactions involving atoms in the bulk BN lattice while retaining the intrinsic properties of the material. In view of the recent advances in the area of 2D nanosheets, it has become apparent that for the application of BN nanosheets, alternative chemical strategies will be necessary to integrate and utilize BNNSs in applications such as surface coatings and nanocomposites.

## **1.2 Low Dimensional Boron Nitride Nanostructures**

“Low-dimensional nanostructured materials [10] refers to a new class of material with reduced dimensionality, i.e., with one or more physical dimension(s) constrained to the nanometer scale. Two-dimensional (2D) nanosheets [1] and nanoribbons, one-dimensional (1D) nanotubes [11,12], and zero-dimensional (0D) fullerenes [13] represent typical examples of such materials. When compared to three-dimensional (3D) bulk substances, low-dimensional structures are anticipated to exhibit new properties due to quantum confinement and/or surface and interfacial effects. Therefore in recent years, scientists have drawn particular attention to

grow such nanostructures in order to enhance their unusual physical and chemical properties that can promote novel applications of material in engineering and applied physics.

Similar to carbon nanostructures, low-dimensional BN nanostructure e.g. BN nanotubes (BNNTs), nanowires, nanoribbons, nanofibers, and nanorods were successfully synthesized. Four years after the identification of carbon nanotubes (CNTs) [14], BNNTs [15] were synthesized and characterized. Subsequently other 1D BN nanomaterials such as nanowires, nanoribbons, nanofibers, and nanorods were also identified. Moreover, inspired by C60 buckyballs, 0D nested and single-layered octahedral BN fullerenes were produced. In addition, after the rise of graphene and the research progress on layered 2D nanostructures, free-standing 2D BN flakes were peeled off from a BN crystal. However, the initial growth of BN nanosheets (BNNs) in the form of so-called nanomeshes on metallic substrates had been reported a year earlier. Structural models of 0D, 1D, and 2D BN nanomaterials are illustrated in Fig. 1.2.

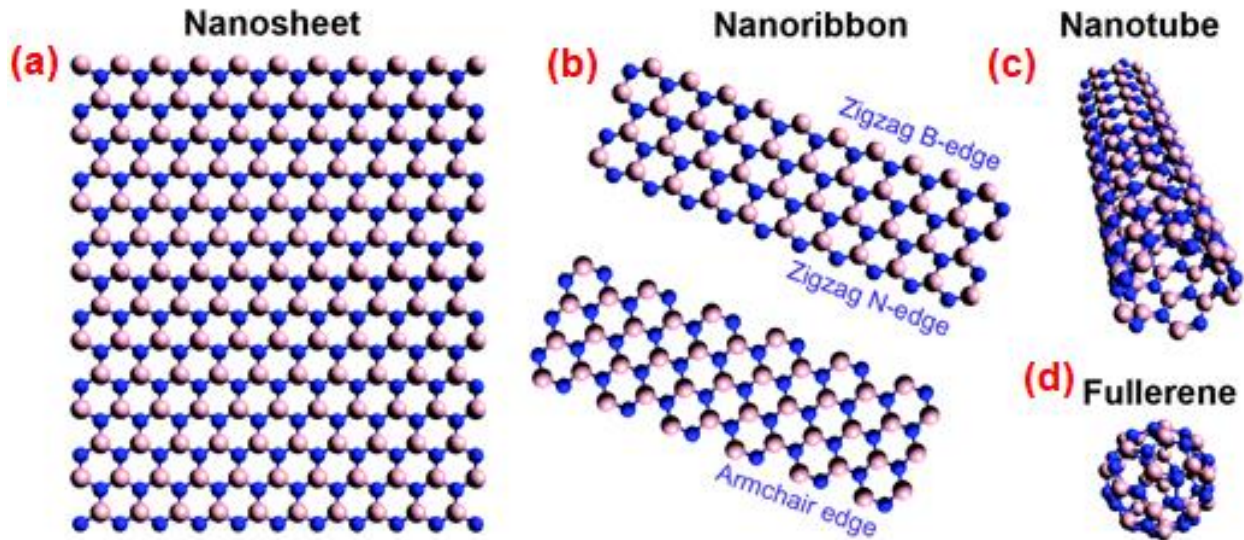


**Figure 1.2** Structural model for low dimensional BNNs: (a) a piece of BN nanosheet, (b) BN nanoribbons, (c) BNNT, and (d) fullerene type BN nanoballs.

### 1.3 Carbon and BN Nanostructures

The comparison between carbon nanostructures and boron nitride nanostructures is particularly helpful for the understanding of their functionality. Figure 1.3 shows a schematic view of carbon nanostructures and BN nanostructures. All carbon nanostructures are solely made of carbon atoms arranged in a typical honeycomb crystal lattice structure while BN nanostructures are composed alternating B and N atoms. Among all these existing nanostructures introduced so far, monolayer system is getting a superb research interest. For developments in nanotechnology it is useful to have single layer systems which are inert, remain clean at ambient conditions and are stable up to high temperatures. In this field  $sp^2$  hybridized graphene and BNNSs are outstanding examples. Both these two materials have  $sp^2$  hybridized layers with about the same lattice constant, but, on most transition metals graphene is metallic, while BNNSs is an insulator or wide band-gap semiconductor.

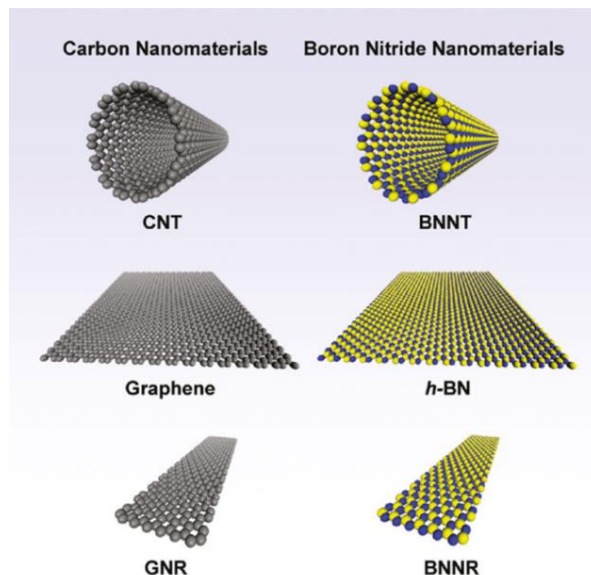


**Figure 1.3** A Schematic illustrates the structure similarity between the carbon nanostructures and the boron nitride nanostructures.

## 1.4 Monolayer Boron Nitride; Analogue of Graphene

The experimental isolation of graphene had opened up the possibility of extracting and isolating 2D forms of crystals composed of elements other than carbon. It has been reported that micromechanical cleavage technique can also be applied to obtain thin BN sheets [16].

Mono layer BNNS is a structural analogue of graphene, promising for many applications [17]. An atomic thick sheet of BN (Figure 1.3) offers unique set of properties which can't be realized in graphene system; such as large band-gap, high optical-transparency, tunable photoluminescence [18], high mechanical strength [19], high thermal conductivity, UV cathodoluminescence [20] and atom-thick electron-tunneling-barrier. Its pronounced thermo-chemical stability (stable up to 1000°C in air and up to 1800°C in inert atmosphere) makes it a superior candidate for high-temperature applications and in chemically-hazardous environment [21]. In spite of these rich properties, the 2D form of BN does not yet share the immense progress relished by graphene. This is because the chemically-passive nature and strong bonding h-BN makes its large scale exfoliation in the single-atom thick form challenging. This is the challenge that we have addressed in our work and have developed new experimental parameters using a short pulsed laser plasma deposition to synthesize BNNSs that results in the highest ever reported yields of atomic thin BNNSs. Unlike to nano carbon (graphene and carbon nanotubes), whose non-polar C–C bonds form a uniform and smooth sidewall structure, while in BNNSs, nano BN contains polar B–N bonds with ionic character, which can induce an extra dipole moment within the structure, indicating this material is probably superior to nano carbon materials. The schematic of BN monolayer is shown in Fig. 1.4 [16].

Monolayer BN has strong influence on the physical and chemical properties of a material. Sticking and bonding of atoms and molecules may change by orders of magnitude, as well as the

charge transport properties across and parallel to the interface. Nevertheless, due to the electronegativity differences between the B and the N atoms the electrons tend to localize around the N atomic centers thus forming an insulating material. Furthermore, the polarity of the B-N bond results in formal charges around the atomic centers thus allowing for monopolar inter-layer electrostatic interactions to join higher electrostatic multipoles, dispersion interactions, and Pauli repulsion in dictating the nature of the interlayer binding. This, in turn, stabilizes the AA' stacking mode (Fig. 1.1) where a B atom bearing a partial positive charge in one layer resides on top of the oppositely charged nitrogen atoms on the adjacent layer.

Based on the above considerations, one may generally deduce that electrostatic interactions between partially charged atomic centers may play a crucial role in the interlayer binding of polar layered materials. Specifically, the electrostatic attractions between the oppositely charged atomic centers in adjacent BN layers are expected to result in a considerably shorter interlayer distance than that measured in graphite. Nevertheless, the interlayer distances in graphite (3.33-3.35 Å) and in BNNSs (3.30-3.33 Å) are essentially the same suggesting that monopolar electrostatic interactions, which exist in BN and are absent in graphite, have little effect on the interlayer binding. This is consistent with a recent study showing that van der Waals (vdW) forces, rather than electrostatic interactions, are responsible for anchoring layers at the appropriate interlayer distance.

BN Mono-layer can be synthesized from bulk BN by either mechanical cleavage or using chemical-solution-derived methods [22]. The size of the flake is usually limited which could hinder the possible applications of *h*-BN. Several alternative synthetic routes, e.g. chemical vapor deposition (CVD) [23-25] and physical vapor deposition (PVD) [26-28] have also been developed. These fabrication processes are complicated, time consuming and yielding small



amounts of products. Previously it was also demonstrated that well-ordered monolayers of *h*-BN can be obtained by exposing borazine to Ni(111) or other transition metal surfaces at high temperatures ( $>700\text{ }^{\circ}\text{C}$ ) [29]. However, this method requires ultra-high vacuum (UHV). The *h*-BN growth under UHV conditions appears to be self-limiting to one monolayer, and the growth of multilayers turns out to be difficult [30]. For large scale electronic applications, it is necessary to generate large area, high-quality, well-ordered layer structured BNNSs at low substrate temperature and moderate vacuum levels. So far, it was a challenge to grow high-yield and high-quality BNNSs at low vacuum and low substrate temperature.

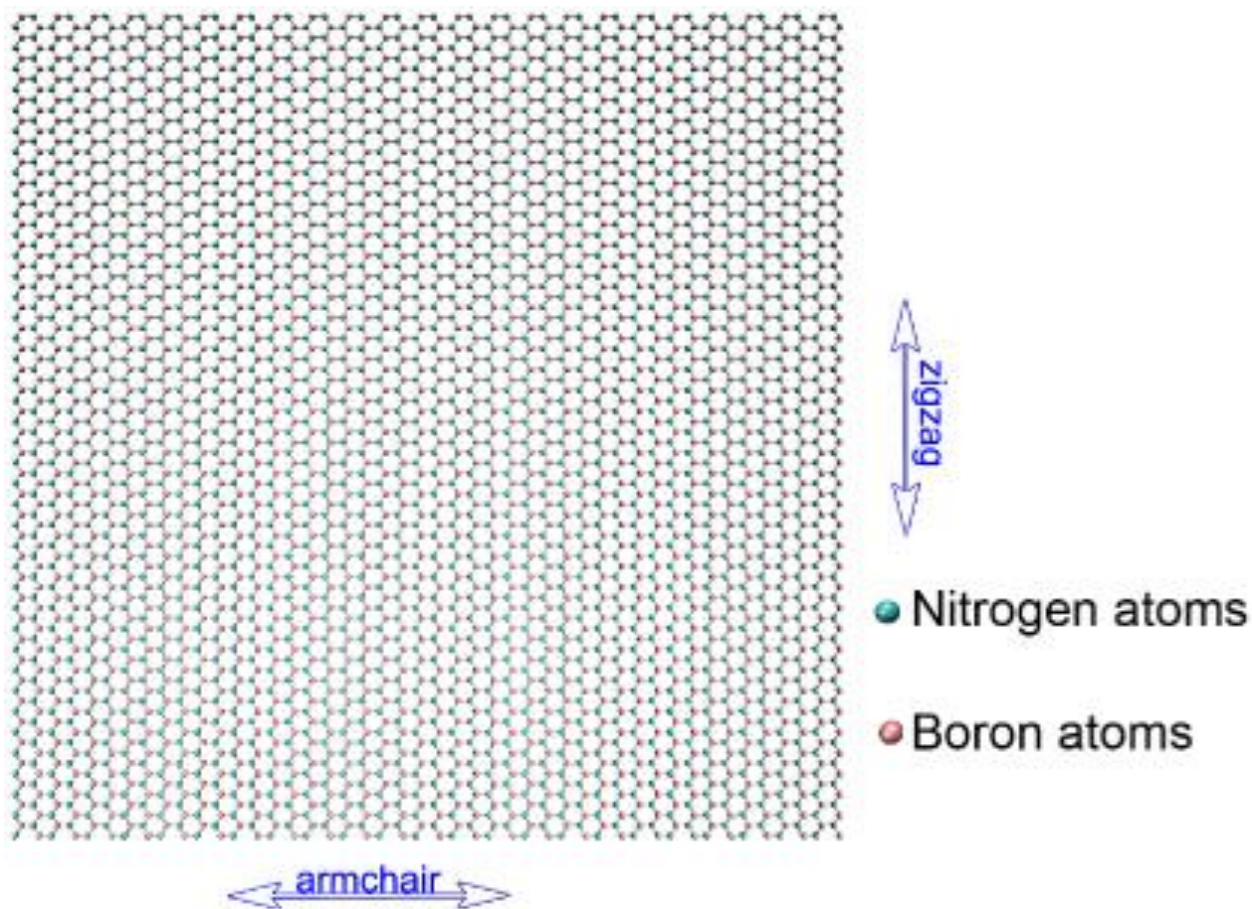


**Figure 1.4** Schematic of BN monolayer.



## 1.5 BN Solid State Phase; c-BN Film

BN can be assumed variety of phases, of which h-BN such as BNNSs and c-BN films are most common [31,32]. Like diamond, c-BN is a chemically resistant, electrically insulating material possessing a high hardness and is used in application where carbon based materials are limited by oxidation. Also, c-BN is a wide, indirect band gap and can be doped with silicon or berkelium to form high temperature n-type and p-type semiconductors. Furthermore, it is nonreactive with ferrous metals at temperature as high as 1500-1600 K.

c-BN has a zinc-blende crystal structure consisting of two independently face centered (FCC) lattices; one comprised of B atoms and other with the N atoms. The crystal structure is similar to diamond except that there are two species in the zinc-blende structure with unlike atoms on different closed-pack planes with ABC stacking sequence. In c-BN, the atoms are bonded with four nearest neighbors of the alternate species through tetrahedral, sigma bonding of  $sp^3$  hybridized orbitals. Illustration of the c-BN crystal structure is shown in Fig. 1.5.

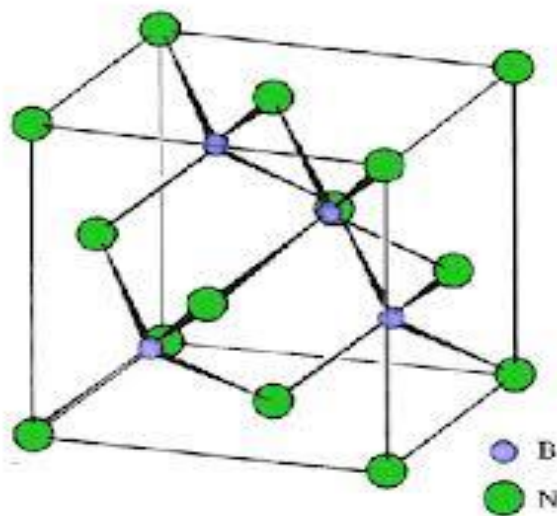


**Figure 1.5** Schematic of c-BN Structure.

## 1.6 Energy Band-Gap Modification in BNNSs

Wide band-gap electronic structure in BNNSs leads to some limitations for their applications in real electronic devices. In order to achieve desired electric and electronic properties, for example, to prepare a practical diode or transistor, one has to perform a doping of BNNSs layers and induce impurities in the electronic structure [33].

So far, doping is a most feasible method to reconstruct the energy band-gap in solids. The doping process can be accomplished via plasma ion implantation technique [34,35]. The dopant atoms incorporate into the BNNSs that could possibly lead to the formation of different layered structure and improve the electronic and semiconducting properties of the material [36].

Generally, BNNSs can be doped p-type with beryllium and n-type with boron, sulfur, and silicon or co-doped with carbon and nitrogen [37]. The best doping concentrations for BNNSs remain to be investigated. So far, it is reported that the combination of C atoms with B and N atoms could possibly lead to the formation of different ( $B_x-C_y-N_z$ ) layered structure. Theoretical studies have also anticipated that the electronic structure and band gap of  $B_x-C_y-N_z$  will depend on composition and electronic arrangement of B, C and N elements in the lattice [38]. The dopant atoms incorporate in the crystalline structure and improve the electronic and semiconducting properties of the material.

Several possible structures can be constructed via doping in BNNSs as shown in Fig. 1.6 (a-b). It is obvious that advanced semiconductor devices in integrated circuits are smaller than 20 nm in length and width, and continue to shrink at a rapid pace. At such small size, addition of a single atom in the active region of the device can drastically change the device behavior. Figure 1.6 (b) shows several possible hybridized nanostructures BNNSs formed by doping carbon

elements. For example a single  $B_3-N_3$  ring can be hybridized into several possible ways, for example  $B_2-C_2-N_2$ ,  $B_1-C_3-N_2$ ,  $B_2-C_3-N_1$ ,  $B_3-C_1-N_2$  etc as shown in Fig. 1.6 (b) [38].

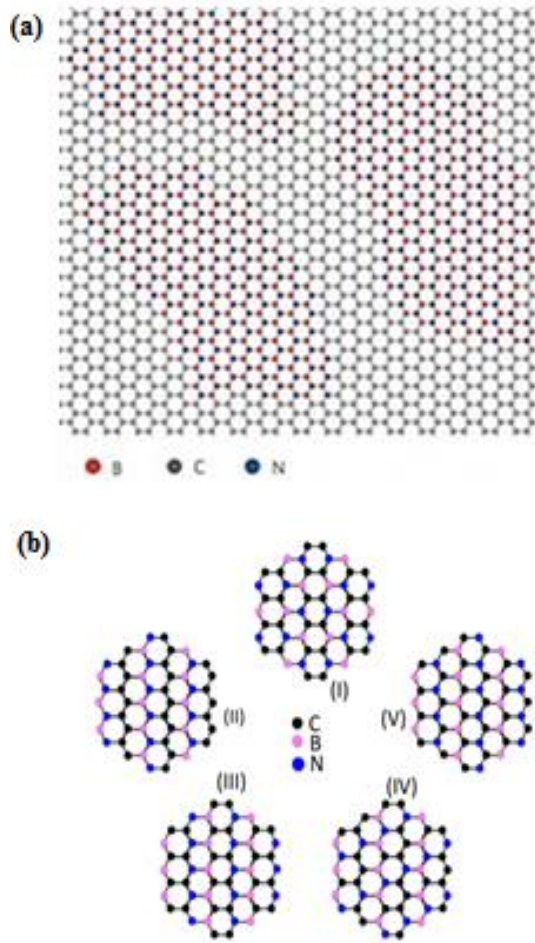


**Figure 1.6** (a) Schematic of doped single layer BNNS, (b) hybridized BNNSs structures with carbon elements.

## 1.7 Application of BNNSs

BNNSs have been tested for numerous applications in electronics and optoelectronics. For example, BNNSs are considered an excellent dielectric material. Moreover, BNNSs have also been reported as superb substrate material for graphene based electronic devices. An

example is shown in Fig. 1.7 in which significant increase in output current recorded when graphene deposited on BNNSs substrate [39].

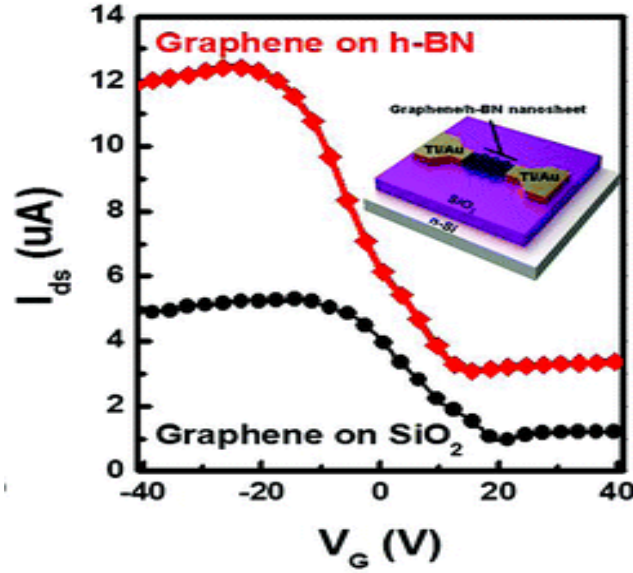


**Figure 1.7** I-V characteristics of graphene placed on  $SiO_2$  and BNNSs.

### 1.7.1 BNNSs-Based Deep UV Photo Detectors

DUV photo detectors have been widely used in various commercial and military applications, such as environmental protection, pollutions monitoring, water purification, secure space-to-space communications, NASA aerospace applications, information storage technology, flame sensing and early missile plume detection [40]. Many wide-band-gap semiconductors with good optical properties such as doped gallium nitride (GaN) [41,42], zinc oxide (ZnO) [43,44] silicon carbide (SiC) [45,46] and diamond [47,48] have been used for UV detectors, but few concerns with BNNSs for DUV detectors as BNNSs have large energy-band gaps, chemically and thermally more stable than that of traditional semiconductors used for UV applications. The flat surface of nanosheets has enormous potential to absorb UV light and transform it into signal. Moreover, BNNSs-based DUV optical sensor show good response to UV light with wavelengths

below 254 nm, therefore they can operate for aerospace communication and devices operating in extreme environments where properties of other material such as GaN, ZnO and diamond fall short.

### 1.7.2 BNNSs-Based Schottky Diode

A metal–semiconductor junction can be formed between a metal and a semiconductor, creating a Schottky barrier (instead of a semiconductor–semiconductor junction in conventional diodes). The metal side acts as the anode and n-type semiconductor acts as the cathode of the diode. A typical symbol of Schottky diode is shown in Fig. 1.8. Traditional materials used are molybdenum, platinum, chromium or tungsten, and certain silicides, e.g. palladium silicide and platinum silicide; and the semiconductor would typically be n-type silicon [49,50].

BNNSs are wide band-gap materials that could be used as Schottky diode after doping. With doped semiconductors, the width of the depletion region drops. Below certain width, the charge carriers can tunnel through the depletion region. At very high doping levels the junction does not behave as a rectifier anymore and becomes an Ohmic contact. This can be used for simultaneous formation of Ohmic contacts and diodes, as diodes form between the silicide and lightly doped n-type region and Ohmic contacts form between the metal and a heavily doped n- or p-type region in semiconductor.

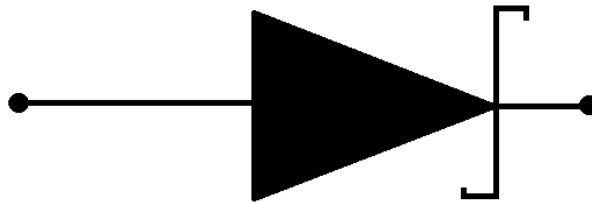


**Figure 1.8** A typical symbol of a Schottky diode.

Generally, different materials have different Fermi levels. When they are brought into electrical contact, enabling electron transfer between the materials, the work done in removing an electron from one material and placing it in the other is equal to the energy difference in the Fermi levels. Consequently, energy is released upon contact by electron transference from the material with the higher Fermi level to the material with the lower Fermi level. This charge transfer continues until the electrical charge difference means the energy gain from transfer is countered by the electrical work required against the charge difference. At this point the two Fermi levels are brought into coincidence at a common level  $E_F$  and no further charge transfer occurs. This flat Fermi level situation corresponds to thermal equilibrium and no net current flows once equilibrium is reached.

The final potential barrier between the metal Fermi level and the majority carrier band edge in the semiconductor is called the Schottky barrier, traditionally labels as  $\phi_B$ . It is a form of contact potential. The potential drop across the semiconductor depletion layer is called the built-in potential, labeled  $\phi_{bi}$  in the Fig. 1.9.

The formation of a Schottky barrier is shown schematically in the figure 1.9, beginning with the isolated materials (top), an intermediate dipole formation stage (center), and the completed configuration with formation of a depletion layer (bottom). The top panel shows a charge-neutral, partly filled metal energy band and a charge-neutral semiconductor valence and conduction band, chemically and electrically isolated from each other. The Fermi level in the p-type semiconductor  $E_{Fp}$  (assumed to be in units of eV) is near its valence band edge, as set by its acceptor impurity doping. The Fermi level in the metal  $E_{Fm}$  marks the half-occupancy energy level in the partly filled band of the metal.

The center panel shows schematically the formation of an immobile interfacial dipole layer that alters the Fermi level difference, and adjusts how much mobile charge transfer occurs to form the depletion layer. This dipole formation is not only a result of quantum mechanics at a discontinuity between solids, but chemical processes involving the atomic layers in what is sometimes called the interface specific region. The interfacial dipole layer reflects the fact that properties of the bulk materials by themselves do not determine the charge transfer that occurs. Rather, the chemistry of the interface, defects at the interface, and the mechanical adaptation to new atomic positions near the interface that are differently spaced than those found in bulk material, all conspire to alter the amount of charge transfer from that expected from bulk properties. This interface dipole contribution is specific to the interface materials, and is different for (say) a material interface cleaved in vacuum and that for the same material mated to some other material. This interface dipole also is different for differently oriented or differently structured crystal planes. But whatever the final amount of charge transfer, charge transfer occurs and the two adjoined materials each acquire a charge.

The bottom panel shows the final configuration following mobile charge transfer between the materials. The transfer of electrons from the metal results in a very thin layer of positive charge in the metal very near the interface. Because the electron density in the metal is extremely large, the band bending in the metal is negligible in the diagram. On the other hand, the density of holes in the semiconductor is not nearly as large as the electron density in the metal, so the charging of the semiconductor is spread deeply into the material (the field effect). The semiconductor gains electrons, as indicated by the bending of the valence band edge away from the Fermi level, which increases the valence band occupancy by electrons. Differently stated, the vacancies (holes) in the valence band are reduced in number, and the charge balance in the band-

bending region is lost. In this depletion layer, the holes or majority carriers are depleted (the unshaded surface region in the figure), exposing the immobile negative acceptor dopant ions to make this region charge-negative. This dopant charge results in a potential according to Poisson's equation. The potential decreases with distance toward the bulk semiconductor, and at some distance (the depletion width) the bulk properties of the semiconductor are regained and the semiconductor bulk is charge neutral.

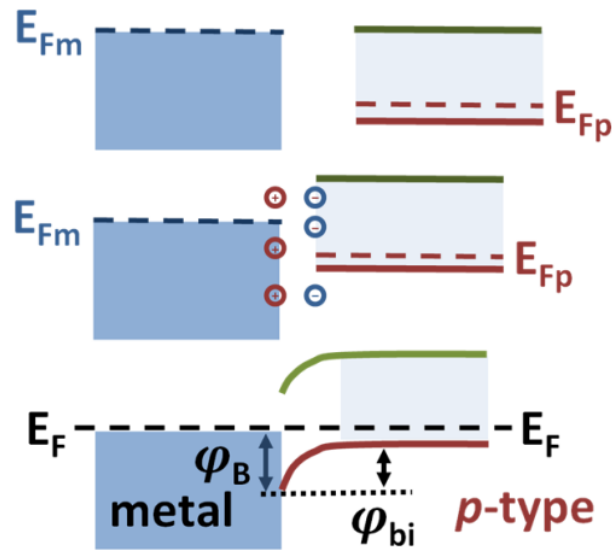


**Figure 1.9** Schottky barrier formation on p-type semiconductor. Top: isolated charge-neutral bulk materials. Center: dipole layer formed as materials interact; Fermi level difference is reduced. Bottom: final configuration following charge transfer to reach equilibrium with no applied voltage. The neutral (shaded) region in the semiconductor moves away from the interface, leaving a charged depletion region (unshaded) near the interface.

At zero bias there is no net current, because the current from the semiconductor is balanced by that from the metal. According to the model of thermionic emission, the current flowing over an energy barrier is proportional to the carrier density next to the barrier. One can imagine the carriers in rapid thermal motion randomly directed. The carriers approaching the barrier with energies lower than the barrier height bounce off the barrier and do not cross it.



Some fractions of those that are more energetic escape backward scattering to succeed in surmounting the barrier, and are lost to the far side. On the metal side, hole injection from the metal Fermi level into the semiconductor valence band is small as it requires surmounting a large energy barrier. On the semiconductor side, hole injection into the metal requires surmounting the built-in barrier height,  $\phi_{bi}$ . Although the barrier on the semiconductor side is smaller than the Schottky barrier  $\phi_B$  on the metal side, so is the carrier density. The two currents balance at zero bias, so no net current flows. These balancing current flows are much larger than in the pn-diode because thermionic emission results in larger currents than the diffusion-recombination mechanism of the pn-diode.

### **1.7.3 Gas Sensing Properties of BNNSs**

The development of gas-sensor devices with optimized sensitivity has been gaining prominence interest in material technology. The use of a semiconductor fabrication line is a preferred manufacturing process because of the potential to reduce cost. However, fundamental materials and processing issues which are critical for a high-performance gas sensor operating in harsh environment need to be addressed. Recently, graphene-based nano-electronic devices and gas-sensors [51] have been used successfully that brought great interest toward the nano-technological devices using other ultra-thin nanomaterials such as boron nitride nanosheets (BNNSs). Nanocrystalline boron nitride (BN) offers immense promise for improve sensitivity of the sensor for different working gasses. Previously, the gas sensing properties of BNNTs, and C-doped BNNTs for some small gas molecules, such as  $\text{CH}_4$ ,  $\text{CO}_2$ ,  $\text{H}_2$ ,  $\text{N}_2$ ,  $\text{NO}_2$ ,  $\text{O}_2$ , and  $\text{F}_2$ , have been investigated by using the density functional theory calculations [52-56]. However, BNNTs present a low sensitivity to the various gaseous molecules, while few atomic layer BNNSs are fascinating for high-performance gas-sensor. Morphologically alike to the honeycomb graphene, the chemical alternation of boron (B) and nitrogen (N) atoms causes the ionic nature of this crystal that could be highly sensitive for various gasses e.g.  $\text{CH}_4$ ,  $\text{H}_2$ ,  $\text{N}_2$  etc. Electronic

properties of BNNSs are strongly affected with slight interaction (adsorption on the surface of BNNSs) of gas molecules, a prerequisite for nanomaterial based gas-sensor. Two-dimensional flat layers of BNNSs allow total exposure of all its atoms to the adsorbing gas molecules, providing the large sensor area per unit volume and increase the sensitivity. Due to its high thermal stability and chemical inertness of BNNSs, the sensors can be used in harsh environment where properties of other material fall short.

### **1.8 BNNSs Science Developed in this Thesis**

The current research based on the synthesis of thin BNNSs on large scale for practical applications. The Ultra-thin boron nitride sheets obtained so far with different methods exhibit small sizes [57]. In this thesis we applied CO<sub>2</sub>-pulsed laser deposition technique for the synthesis of atomic layers BNNSs on practical scale and investigated the fundamental study related to electronic and opto-electronics. For example, a superb class of nanosystem explored in this thesis is the synthesis of atomic thin sheet of BN material. An artistic rendition of the single BN layer is shown in Fig. 1.10 a while, TEM image of atomic layer BNNS obtained experimentally clearly interprets honey comb crystal lattice structures so far reported by theoretical models. It has similar crystalline structure to that of graphene exfoliated mechanically using scotch tape method [1]. These nanosheets have several potential applications that have not been realized from graphene so far [58]. The obtained material and method used has been discussed in this thesis in detail.

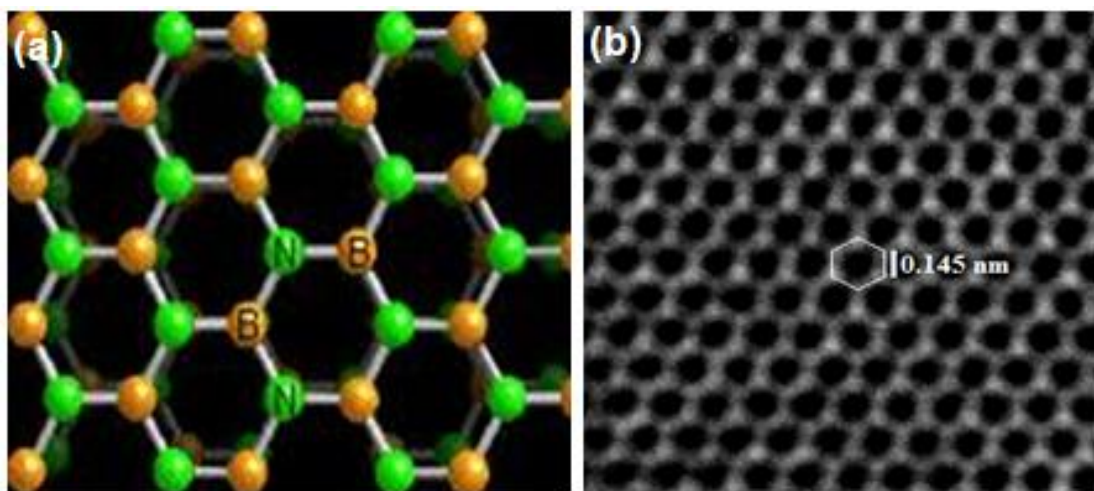


**Figure 1.10** The superb class of nanosystem explored in this thesis is the atomic thin sheet of boron nitride. a) An artistic rendition of the single boron nitride layer. b) TEM image of experimentally obtained BNNSs transferred on a lacey carbon grid. Such nanosheets are obtained by the method developed in this thesis.

## 1.9 Overview of Dissertation

**Chapter 1** introduces the current state of knowledge available on low-dimensional nanomaterials and presents an overview of the experimental projects that are discussed ahead in Chapters.

**Chapter 2** presents a detailed study on the introduction of the synthesis and characterization techniques used in this thesis. The development of system used to deposit monolayer and few layers BNNSs is presented in detail. The work presented in this chapter has been published as an article in Journal of Material Research.

**In Chapter 3**, large-scale synthesis and electron microscopic characterizations of BNNSs has been explained. First time we experimentally realized honeycomb crystal lattice structure by using HRTEM study of our samples prepared in our laboratory. Layered structures and thickness of the nanosheets were investigated utilizing HRTEM measurements results. This work has appeared as an article in Journal of Material Science.

The work presented in **Chapter 4** is the continuity of our investigations on nanoscale structure study of BNNSs by using electron microscope. Important insights into the crystalline structural, layers and thickness of the samples more precisely targeted. Starting from monolayer layer BNNS, its features based on honeycomb network of B and N atoms and few-layer characterization to obtain thickness of nanosheets has been demonstrated in detail. Imaging of the edges of several BNNSs are taken to identify clear picture related to thickness of our samples. This work has been published as an article in the Journal of Nanoscale.

In **Chapter 5**, different applications of BNNSs e.g. Schottky diode, UV detector and gas sensor have been studied. Doping makes BNNSs a functional material to electronic and optoelectronic application has identified in detail. The work composed in this chapter can be found out in several journal e.g. Journal of Nanoscale, ACS; Applied Materials and Interfaces, Material Research Bulletin, and Material Letters.

**Chapter 6** provides detail how to synthesize c-BN films and BN nanostructures at low substrate temperature. Our investigations include detail role of catalyst in the transformation of hexagonal base layer to cubic BN film. The effect of deposition parameters in the synthesis of BN nanostructures is describes in detail. This work has been published in Journal of Applied Physics Letters and Physics Scripta.

At the end, **Chapter 7** summarizes the key contributions of this research towards the field of nanotechnology and it also presents the potential of 2D BNNSs for future research directions. As a whole, this dissertation describes classes of novel experiments on nanosystems and provides experimental framework of carrying out such detailed measurements in 2D layered materials.

## 1.10 References

- [1] K. S. Novoselov, A. K. Geim, S. V. Morozov, D. Jiang, Y. Zhang, S. and I. V. Grigorieva, A. A. Firsov, Electric field effect in atomically thin carbon films, *Science* 306, p. 666, 2004. doi:10.1126/science.1102896.
- [2] A. S. Mayorov, R. V. Gorbachev, S. V. Morozov, L. Britnell, R. Jalil, L. A. Ponomarenko, P. Blake, K. S. Novoselov, K. Watanabe, T. Taniguchi, A. K. Geim, Micrometer-scale ballistic transport in encapsulated graphene at room temperature, *Nano Lett.* 11, p. 2396, 2011. doi:10.1021/nl200758b.
- [3] J. Moser, A. Barreiro, A. Bachtold, Current-induced cleaning of graphene, *Appl. Phys. Lett.* 91, p. 163513, 2007. doi:10.1063/1.2789673.
- [4] C. Lee, X. D. Wei, J. W. Kysar, J. Hone, Measurement of the elastic properties and intrinsic strength of monolayer graphene, *Science* 321, p. 385, 2008. doi:10.1126/science.1157996.
- [5] A. A. Balandin, Thermal properties of graphene and nanostructured carbon materials, *Nat. Mater.* 10, p. 569-581, 2011. doi:10.1038/nmat3064.
- [6] R. R. Nair, P. Blake, A. N. Grigorenko, K. S. Novoselov, T. J. Booth, T. Stauber, N. M. R. Peres, A. K. Geim, Fine structure constant defines visual transparency of graphene, *Science* 320, p. 1308, 2008. doi:10.1126/science.1156965.
- [7] Y. Lin, T. V. Williams, J. W. Connell: Soluble, Exfoliated Hexagonal Boron Nitride Nanosheets. *J. Phys. Chem. Lett.* 1, 277 (2010).
- [8] Y. Lin, T. V. Williams, W. Cao, H. E. E Ali, J. W. Connell: Defect Functionalization of Hexagonal Boron Nitride Nanosheets. *J. Phys. Chem. C* 114, 17434 (2010).
- [9] J. C. Meyer, A. Chuvilin, G. Algara-Siller, J. Biskupek, U. Kaiser: Selective sputtering and atomic resolution imaging of atomically thin boron nitride membranes. *Nano Lett.* 9, 2683 (2009).
- [10] Amir Pakdel, Chunyi Zhi, Yoshio Bando, and Dmitri Golberg; *Materials Today*, JUNE 2012 | VOLUME 15 | NUMBER 6.
- [11] S. Iijima, *Nature* 354, 56 (1991).
- [12] D Golberg, Y Bando, W Han<sup>1</sup>, K Kurashima, T Sato; *Chemical Physics Letters*, Volume 308, Issues 3–4, 23 July 1999, Pages 337–342; Single-walled B-doped carbon, B/N-doped carbon and BN nanotubes synthesized from single-walled carbon nanotubes through a substitution reaction.
- [13] H. W. Kroto, J. R. Heath, S. C. O'Brien, R. F. Curl and R. E. Smalley, *Nature* 318, 162 (1985).
- [14] Sander J. Tans<sup>1</sup>, Alwin R. M. Verschueren<sup>1</sup> & Cees Dekker ; *Nature* 393, 49-52 (7 May 1998) | doi:10.1038/29954; Received 6 January 1998; Accepted 2 April 1998 Room-temperature transistor based on a single carbon nanotube.

- [15] Chunyi Zhi, Yoshio Bando, Chengchun Tan, Dmitri Golberg; Solid State Communications Volume 135, Issues 1–2, July 2005, Pages 67–70 Cover image Effective precursor for high yield synthesis of pure BN nanotubes.
- [16] Withers, N. 2D nanostructures: Inorganic graphene. Nat Chem 2010.
- [17] Ki Kang Kim, Allen Hsu,<sup>†</sup> Xiaoting Jia, Soo Min Kim, Yumeng Shi, Mario Hofmann, Daniel Nezich, Joaquin F. Rodriguez-Nieva, Mildred Dresselhaus, Tomas Palacios, and Jing Kong; Nano Lett. 2012, 12, 161–166; dx.doi.org/10.1021/nl203249a; Synthesis of Monolayer Hexagonal Boron Nitride on Cu Foil Using Chemical Vapor Deposition.
- [18] Muser, L.; Kanaev, A. Near band-gap photoluminescence properties of hexagonal boron nitride. Journal of Applied Physics 2008, 103, 103520-103520-7.
- [19] Chun Li, Yoshio Bando, Chunyi Zhi, Yang Huang and Dmitri Golberg; Nanotechnology 20 385707. doi:10.1088/0957-4484/20/38/385707.
- [20] Watanabe, K.; Taniguchi, T.; Niiyama, T.; Miya, K.; Taniguchi, M. Far-ultraviolet plane-emission handheld device based on hexagonal boron nitride. Nat Photon 2009, 3, 591-594.
- [21] Chen, Y.; Zou, J.; Campbell, S. J.; Le Caer, G. Boron nitride nanotubes: Pronounced resistance to oxidation. Appl. Phys. Lett. 2004, 84, 2430-2432.
- [22] Zhi C, Bando Y, Tang C, Kuwahara H, Golberg D (2009) Large-Scale Fabrication of Boron Nitride Nanosheets and Their Utilization in Polymeric Composites with Improved Thermal and Mechanical Properties Adv. Mater 21: (28), 2889–2893. doi: 10.1002/adma.200900323.
- [23] Song L, Ci L, Lu H, Sorokin P B, Jin C, Ni J, Kvashnin A G, Kvashnin D G, Lou J, Yakobson B I, Ajayan P M (2010); Large scale growth and characterization of atomic hexagonal boron nitride layers. Nano Lett. 10: 3209—3215. doi: 10.1021/nl1022139
- [24] Ismach A, Chou H, Ferrer D A, Wu Y, McDonnell S, Floresca H C, Covacevich A, Pope C, Piner R, Kim M J, Wallace R M, Colombo L, Ruoff R S (2012) Toward the Controlled Synthesis of Hexagonal Boron Nitride Films. ACS nano. 6: 6378–6385. doi: 10.1021/nn301940k.
- [25] Kim K K, Hsu A, Jia X, Kim S M, Shi Y, Hofmann M, Nezich D, Rodriguez-Nieva J F, Dresselhaus M, Palacios T, Kong J (2012) Synthesis of Monolayer Hexagonal Boron Nitride on Cu Foil Using Chemical Vapor Deposition. Nano Lett., 12: 161–166. dx.doi.org/10.1021/nl203249a.
- [26] Zhu D M, Jakovidis G, Bourgeois L (2010) Catalyst-free synthesis of carbon and boron nitride nanoflakes using RF-magnetron sputtering. Materials Letters 64: 918–920. doi:10.1016/j.matlet.2010.01.058
- [27] Anzai A, Nishiyama F, Yamanaka S, Inumaru K (2011) Thin film growth of boron nitride on a-Al<sub>2</sub>O<sub>3</sub> (0 0 1) substrates by reactive sputtering. Materials Research Bulletin 46: 2230–2234. doi:10.1016/j.materresbull.2011.09.006.
- [28] Moussa B B, Haen J D, Borschel C, Barjon J, Soltani A, Mortet V, Ronning C, Olieslaeger M D, Boyen H-G, Haenen K (2012) Hexagonal boron nitride nanowalls:

- physical vapour deposition, 2D/3D morphology and spectroscopic analysis. *J. Phys. D: Appl. Phys.* 45: 135302 (8pp) doi:10.1088/0022-3727/45/13/135302.
- [29] Nagashima A, Tejima N, Gamou Y, Kawai T, Oshima C (1995) Electronic dispersion relations of monolayer hexagonal boron nitride formed on the Ni(111) surface. *Phys. Rev. B* 51: 4606–4613. doi: 10.1103/PhysRevB.51.4606
  - [30] Shi Y, Hamsen C, Jia X, Kim K K, Reina A, Hofmann M, Hsu A L, Zhang K, Li H, Juang Z-Y, Dresselhaus MS, Li LJ, Kong J (2010) Synthesis of Few-Layer Hexagonal Boron Nitride Thin Film by Chemical Vapor Deposition. *Nano Lett.* 10: 4134–4139. doi: 10.1021/nl1023707.
  - [31] P. B. Mirkarimi, K.F. McCarty, D.L. Medlin; *Materials Science and Engineering: R: Reports*, Volume 21, Issue 2, 15 December 1997, Pages 47–100
  - [32] P. B. Mirkarimi, D. L. Medlin, K. F. McCarty and J. C. Barbour; *Appl. Phys. Lett.* 66, 2813 (1995); <http://dx.doi.org/10.1063/1.113484>.
  - [32] C. Ronning, E. Dreher, H. Feldermann, M. Gross, M. Sebastian, H. Hofsäss; *Diamond and Related Materials* Volume 6, Issue 9, July 1997, Pages 1129–1134.
  - [33] H. X. Zhang, and P. X. Feng; *ACS Appl. Mater. Interfaces* 2012, 4, 30–33; [dx.doi.org/10.1021/am201435z](http://dx.doi.org/10.1021/am201435z).
  - [34] Xianlong Wei, Ming-Sheng Wang , Yoshio Bando , and Dmitri Golberg; *ACS Nano*, 2011, 5 (4), pp 2916–2922; DOI: 10.1021/nn103548r
  - [35] Yang, B. Q.; Kumar, A.; Upia, N.; Feng, X. P.; Katiyar, R. S. *Journal of Raman Spectroscopy* 2010, 41, 88.
  - [36] Rubio, A. *Nat. Mater* 2010, 9, 379.
  - [37] Haibo Zeng, Chunyi Zhi, Zhuhua Zhang, Xianlong Wei, Xuebin Wang, Wanlin Guo, Yoshio Bando, and Dmitri Golberg; *Nano Lett.*, 2010, 10 (12), pp 5049–5055; DOI: 10.1021/nl103251m
  - [38] Rubio, A. *Nat. Mater* 2010, 9, 379] [Rubio, A.; Corkill, J. L.; Cohen, M. *Phys. Rev. B* 1994, 49, 5081.
  - [39] Kang Hyuck Lee, Hyeon-Jin Shin, Jinyeong Lee, In-yeal Lee, Gil-Ho Kim, Jae-Young Choi, and Sang-Woo Kim; *Nano Lett.*, 2012, 12 (2), pp 714–718; DOI: 10.1021/nl203635v.
  - [40] M. S. Shur, A. Zukauskas, *UV Solid-State Light Emitters and Detectors*. Nano Science Series, Springer 2004, 144, 1.
  - [41] X. Sun, D. Li, H. Jiang, Z. Li, H. Song, Improved performance of GaN metal-semiconductor-metal ultraviolet detectors by depositing SiO<sub>2</sub> nanoparticles on a GaN surface”, *Appl. Phys. Lett.* 2011, 98, 121117.
  - [42] Q. Chen, J. W. Yang, A. Osinsky, S. Gangopadhyay, B. Lim, M. Z. Anwar, M. Asif Khan, D. Kuksenkov, and H. Temkin, “Schottky barrier detectors on GaN for visible–blind ultraviolet detection”, *Appl. Phys. Lett.* 1997, 70, 2277.
  - [43] J. Cheng, Y. Zhang, R. Guo, “ZnO microtube ultraviolet detectors’, *Journal of Crystal Growth*, 2008, 310, 57.

- [44] Y. Jin, J. Wang, B. Sun, J. C. Blakesley, N. C. Greenham, *Nano Lett.* 2008, 8, 1649.
- [45] J. W. Palmour, J. A. Edmond, H. S. Kong, C. H. Carter Jr. *Physica B: Condensed Matter* 1993, 185, 461.
- [46] M. Bruzzi, F. Nava, S. Russo, S. Sciortino, P. Vanni, *Diamond and Related Materials* 2001, 10, 657.
- [47] W. Jiang, J. Ahn, C. Y. Chuen, L. Y. Loy, *Rev. Sci. Instrum.* 1999, 70, 1333.
- [48] J. F. Hochedeza, P. Bergonzob, M. C. Castex c, P. Dhez d, O. Hainaute, *Diamond and Related Materials* 2001, 10, 673.
- [49] Jeramy D. Zimmerman<sup>1</sup>, Iliott R. Brown and Arthur C. Gossard; *J. Vac. Sci. Technol. B* 23, 1929 (2005); <http://dx.doi.org/10.1116/1.2013312>.
- [50] T. L. Poteat, B. Lalevic, B. Kuliye v, M. Yousuf, M. Chen; *Journal of Electronic Materials*; January 1983, Volume 12, Issue 1, pp 181-214.
- [51] E. Massera, V. L. Ferrara, M. Miglietta, T. Polichetti, I. Nasti, G. D. Francia, *chimica oggi/Chemistry Today* 29 (2011) 39-41.
- [52] C. Z. Hu, F. Li, X. D. Liu, *Acta Chim Sinica.* 66 (2008) 1641-1646.
- [53] L. Wang, C. Sun, L. Xu, Y. Qian, *Catal. Sci. Technol* 1 (2011) 1119-1123.
- [54] A. Rubio, J. L. Corkill, M. L. Cohen, *Phys. Rev. B* 49 (1994) 5081-5084.
- [55] N. G. Chopra, R. J. Luyken, K. Cherrey, V. H. Crespi, M. L. Cohen, S. G. Louie, A. Zettl, *Science* 269 (1995) 966-967.
- [56] D. Golberg, Y. Bando, M. Eremets, K. Takemura, K. Kurashima, H. Yusa, *Appl. Phys. Lett.* 69 (1996) 2045-2047.
- [57] Coleman J N, Lotya M, O'Neill A, Bergin S D, King P J, Khan U, Young, K.; Gaucher, A.; De, S.; Smith, R. J.; Shvets, I. V.; Arora, S. K.; Stanton, G.; Kim, H.; Lee, K.; Kim, G. T.; Duesberg, G. S.; Hallam, T.; Boland, J. J.; Wang, J. J.; Donegan, J. F.; Grunlan, J. C.; Moriarty, G.; Shmeliov, A.; Nicholls, R. J.; Perkins, J. M.; Grievson, E. M.; Theuwissen, K.; McComb, D. W.; Nellist, P. D.; Nicolosi, V. Two-Dimensional Nanosheets Produced by Liquid Exfoliation of Layered Materials. *Science* 2011, 331, 568.
- [58] K. Jasuja PhD Thesis; Department of Chemical Engineering College of Engineering Kansas State University, Manhattan, Kansas 2011. Designing nanoscale constructs from atomic thin sheets of graphene, boron nitride and gold nanoparticles for advanced material applications.



## Chapter 2

### Synthesis and Characterization Techniques

This chapter is divided into two major sections; first section describes synthesis techniques with the brief overview of the limitations and second section defines characterization techniques used in present study. A physical explanation along with detail description of newly installed CO<sub>2</sub>-PLD system used to synthesize large area BNNSs is also provided in this chapter.

#### 2.1 Introduction

Over the past several years, considerable efforts have been placed on the synthesis of BN nanostructures and thin films using different synthesis routes e.g. chemical vapor deposition (CVD) method, split furnace tube method, sputtering technique, and laser ablation [1-3]. BN is one of the most interesting non-oxide materials with a bright future in advance material design. This material has great potential for the applications in high performance electronic devices, insulating nanotubular shields, hydrogen storage media, gas absorbents, and reinforcing agents. Like in the case of carbon, different types of BN nanostructures have been produced: For example, Cho et al. [4] prepared BN nano-tubes, Bernard et al. [5] synthesized and characterized nano-particles and fullerenes and very recently, Zhi et al. [6] and Lin et al. [7,8] prepared exfoliated graphene like boron nitride nanosheets, and these inorganic sheets were utilized to improve thermal and mechanical properties of the polymeric composites. Meyer et al. [9] synthesized single-layer hexagonal boron nitride (hBN) and reported atomic resolution imaging. Furthermore, boron nitride polymers have been proposed as new building blocks for electronic devices. Based upon quantum-mechanical simulations, BN can be formulated to tune electronic

properties. Such materials would be much cheaper than conventional semiconductors reported by Cote et al. [10].

The detail description of these synthesis techniques are following.

## **2.2 Chemical Vapor Deposition Method**

Chemical vapor deposition (CVD) is a technique used to produce high-performance solid materials [11]. This technique is often used in the semiconductor industry to produce thin films. The process in this technique comprises the adsorption and reaction of the educts i.e. precursor molecules on the surface where a new material shall grow. The process often involves the cracking or decomposition of the precursor molecules and a partial release of products into the gas phase which react and/or decompose on the substrate surface to produce the desired deposit. Frequently, volatile by-products are also produced, which are removed by gas flow through the reaction chamber. BN single layers have been synthesized on Ru(0001) and Pt(111) surfaces by CVD of benzene like borazine (HBNH)<sub>3</sub> [12]. The process comprises the hydrogen abstraction from the borazine molecules, the assembly of hexagonal boron nitride and the desorption of H<sub>2</sub> gas. The BN growth rate drops after the formation of the first layer by several orders of magnitude. This has the practical benefit that it is easy to prepare few layers BNNSs.

## **2.3 Sputtering Technique**

Sputtering is a physical process where atoms in a solid target material are ejected into the gas phase due to bombardment of the material surface by energetic ions [13-15]. Sputtering process is driven by momentum exchange between the energetic ions and atoms in the material, due to collisions as shown in Fig. 2.5. The number of atoms ejected from the target surface per incident ion is called the sputter yield, which is an important parameter of the efficiency of the sputtering process [16]. The sputter yield depends on the energy of the incident ions, mass of the ions and

target atoms, and binding energy of atoms in the solid target. To discharge the plasma on the target surface, DC (direct current) and RF (radio frequency) alternating current can be used respectively [16-18]. In order to control the plasma properties (ion /electron density) to achieve the optimum sputtering conditions, a variety of techniques are used including magnetic fields and a bias voltage to the target.

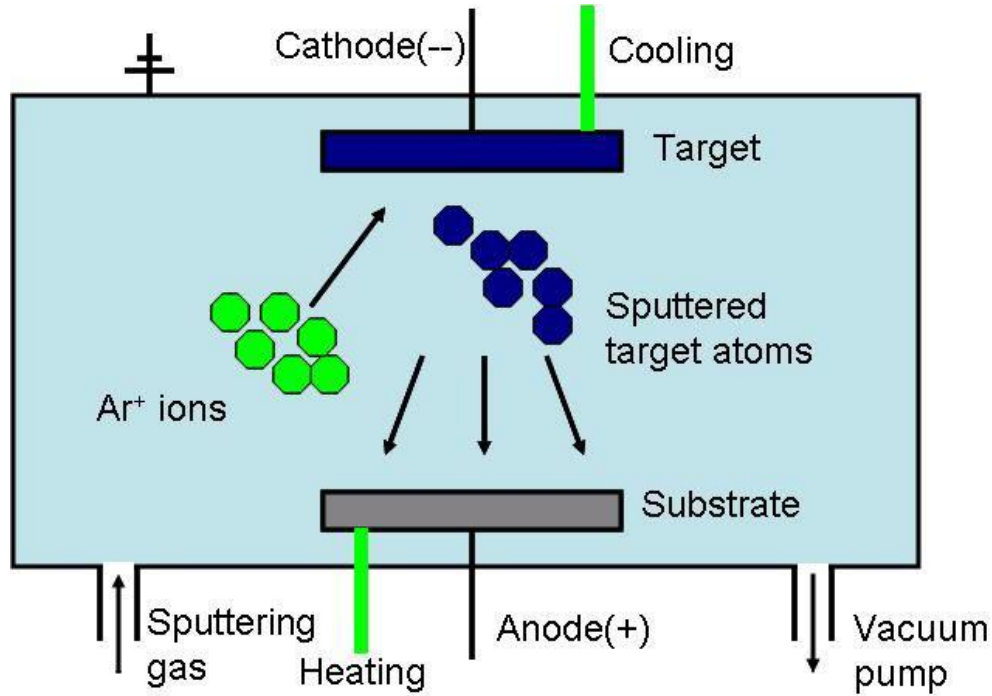


**Figure 2.1** Schematic of the sputtering process for nano-materials deposition.

Sputter coating is a cold process whereby atoms are liberated from a target by ion impacts. The atoms are cool, consequently no thermally induced damage results. Sputtering is a microscopic process involving clouds of atoms, as opposed to the "spray" of relatively large macroscopic clumps of evaporated materials used in evaporative coating. As a result the uniformity and thickness of the coatings are easily controlled. In general, the quality and repeatability obtained by sputter coating are superior to that obtained through evaporative means [19].

In most of the above techniques used for BNNSs growth, growth rate was low even deposition time was long enough and material produced would unavoidably yield impurities in the samples. To achieve high growth rate, these synthesis techniques carries out at very high temperature (1100 °C to 2700 °C) and high pressure that ultimately cause several defects in the samples. For industrial and fundamental practical applications; it is necessary to grow high quality materials on large scale. So far it is a challenging task to fabricate high purity mass product nanostructures and thin films on large scale. Therefore, to increase growth rate and achieve high yield of nanomaterial, it was necessary to develop higher power laser plasma deposition system. In our laboratory, we installed CO<sub>2</sub>-PLD system for the quick synthesis of large area nanostructures and thin films. The growth rate in CO<sub>2</sub>-PLD increased more than 10 times. Moreover, within few minutes of the activation process, we achieved uniform deposition of materials on entire surfaces of the substrates.

## **2.4 Pulsed Laser Plasma Deposition Technique**

Pulsed laser deposition (PLD) has been regarded as a versatile method to grow ceramic thin films such as BNNSs [20-22]. PLD technique seems economic and provides quick method for the growth of BNSS at comparatively low substrates temperature and low pressure. It is a conceptually simple technique that generates reactive species of target material under highly non-equilibrium conditions, which cannot be produced by any other technique. This leads the way to the growth of the materials having unique properties, and indeed, this technique proving to be one of the most attractive methods to synthesize high yield of thin films [23,24]. One of the advantages of our PLD system is that it can largely avoid contamination, also because laser installed outside the chamber; consequently, operation of laser plasma deposition is much flexible. Here, we should also consider the critical role of carbon dioxide (CO<sub>2</sub>) in PLD system.

The CO<sub>2</sub> laser produces radiations in the far infrared part of the spectrum. Light in this part of the spectrum generally produces larger heating effect upon impact on the surface of target material. It ablates target material and produce plasma plume composed of high energy ions and reactive species of the material to be deposited. The geometry of plasma plume is cylindrical or spherical, depends on the deposition environment inside the deposition chamber, and it is highly forward directed towards the substrates. This plasma plume can reach on the substrates surface and deposits mass products nanostructures and thin films. Finally, growth rate of the samples increases enormously.

In our previous report, Feng et al. [24] synthesize various nanomaterials of carbon and carbon related materials using ArF Lambda Physics 1000 plasma deposition technique. However, due to low power density of ArF Lambda excimer laser, it was difficult to increase the growth rate to obtain mass product nanostructures and thin films. This deficiency has been removed after installing CO<sub>2</sub>-PLD system in our laboratory.

## **2.5 Installation of CO<sub>2</sub>-Pulsed Laser Plasma Deposition System**

We installed and up-graded a CO<sub>2</sub>-pulsed laser plasma deposition (CO<sub>2</sub>-PLD) system and used it for the quick synthesis of various BN nanostructures and nanosheets. Each part of CO<sub>2</sub>-PLD system such as focusing of laser beam onto the target surface, sample holder, shutter, heater, type of the gas and gas flow rate can be easily control independently to fit different experimental conditions. After installation of the system, a series of experiments were conducted using *h*-BN target. SEM images showed that entire surface (2×2 cm<sup>2</sup>) of the substrate is covered with the conical and disk shape BN nanostructures; indicating a significantly short time approach to grow large scale material.

### 2.5.1 Experimental Parameters

Different experimental parameters were set to install CO<sub>2</sub>-PLD system. Figure 2.2a shows the photograph of the system. Figure 2.2b shows the inside view of the deposition chamber where different equipment are installed. The dimensions of the deposition chamber and deposition mechanism are well integrated in the schematic diagram shown in Fig. 2.2c. Figure 2.2d shows plasma plume formed with a single short pulse. The detail of the equipment and parameters fitted are listed as followed.

1. Heater and thermocouple for controlling temperature.
2. 2D adjustable substrate holder with multi clamps that can hold 3-6 different substrates at the same time.
3. 3D adjustable target holder together with the motor for controlling rotational velocity of target, direction and location. The distance between the target and the substrate holder is flexible than can be adjusted from 2 cm to 8 cm for controlling plasma density on surface of substrates that determines the growth rate.
4. Shutter for blocking the plasma beam or impurities.
5. 3 gas inlets and controllers for controlling types of gasses and gas pressure.
6. Long focal length lens was selected so that we can install the lens outside the chamber in order to avoid it from plasma contamination. It is also noted that with longer focal lens, laser would produce a plasma beam with smaller spread angle.
7. High power rotary pump and turbo molecular pump for controlling vacuum down to  $10^{-7}$  Torr.
8. Various power supplies.
9. 3 vacuum gauges used for detecting different range of vacuum in the chamber.

10. Several optical windows installed to monitor deposition process.

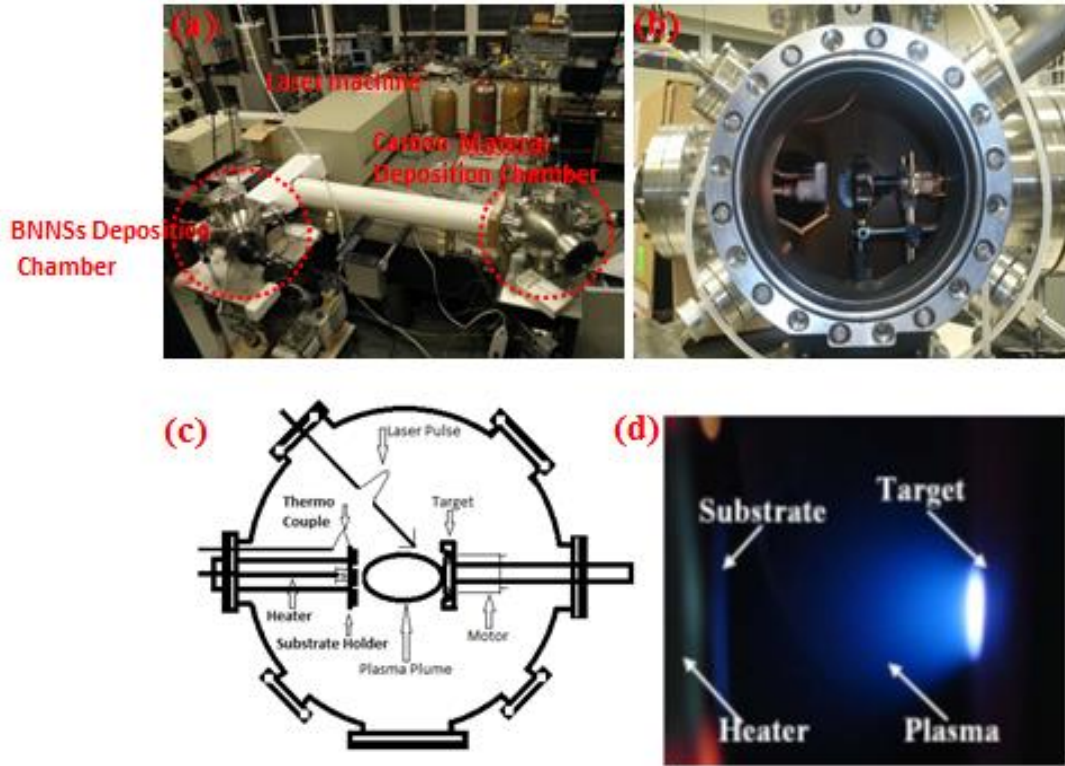


**Figure 2.2** (a) photograph of the CO<sub>2</sub>-PLD installed in our laboratory, b) inside view of deposition chamber, c) schematic illustration of the deposition mechanism, and d) photograph of plasma plume formed in our CO<sub>2</sub>-PLD system.

#### 2.5.1.1 Substrate to Target Distance

Most of the experiments were performed with the target to substrate distance ranging from 2 cm to 5 cm. The longer or shorter distance could be desired based on the fact that the deposition with laser plasma consists of two processes, ionic deposition and molecular deposition. If longer distance will be selected, it might be possible that boron and nitrogen ions recombine into molecule before reaching to the substrate surface that will affect the boron/nitrogen (B/N) ratio in the samples. Therefore, for stoichiometric nanostructure growth

process, short distance is required for atomic deposition so that B/N ratio could be 1 or near to 1. Meanwhile, to control the growth rate and achieve large areas of the coated films, longer distance could be desired. For the case of higher beam energy, larger distance between substrates and target is necessary so that the high energy plasma ions would not destroy the surface of the initially grown layers or nanostructures. This fact also been reported by Noorhana et al. [25]. Considering all above parameters into account, we optimized the substrate to target distance 3 cm. It was noticed that tip of cylindrical plasma plume was lying directly onto the surface of the substrates. In such way, uniform and optimized depositions could be possible.

#### **2.5.1.2 Angle of Incidence**

The laser incidence angle related to the target surface is an important parameter. When laser interact the target surface, it generates plasma plume perpendicular to target surface. The substrates should directly face the target surface in order to get maximum yield. Therefore, the laser incident angle ' $\theta$ ' with respect to the target plane was set at 45 degree. If the angle will be too small, the size and the location of the spot will be difficult to control. In contrast, if the angle is too large, the substrate holder will be an obstruction.

#### **2.5.1.3 Substrate Holder**

The new design of the substrate holder can easily hold multi substrates. The manner in which the substrates were held and their location and orientation relative to the target were important parameters in the CO<sub>2</sub>-PLD system. We designed locally the substrate holder based on ceramic cup. The base of the substrate holder was of molybdenum plate which screwed four metal clamps to hold the substrates in vertical position directly facing the target. The purpose of the number of clamps was to place different materials as substrates at the same time to study the substrate material effect on nanostructure growth rate under the same experimental conditions.



When the laser ablates the target, the evaporants eject highly forward directed plume along the target normal. Therefore, the substrate must be held directly opposite to the target. Aluminum plate was also inserted to cover the base port of the chamber (where turbo pump was installed). The plate protects the turbo pump from any kind of contamination or piece fall down from the substrate holder, target or from the chamber.

During the deposition process, the evaporants from the target moves to all surfaces with in the chamber including the direction of laser window. The material deposited on the window will interact with the laser beam resulting permanently damage to the window. Therefore, we adjusted the window to target distance up to 25 cm such that the material reach to the window is to be greatly reduced.

Target was installed to easily access within the chamber so that mounting and demounting should be as simple as possible. To get uniform and large area deposition of the sample, a motor was connected to the target holder to rotate the target during deposition. In this manner, plasma plume produced on the surface of the target also rotates with the target and covers entire substrate surface. Two special lenses were arranged; one for focusing purpose and other was used as CO<sub>2</sub> laser window so that the laser pulses hit the target accurately.

## **2.6 Crystalline Structure Analysis**

The crystalline structure of the samples was analyzed by Raman spectroscopy using triple monochromator with an excitation wavelength of 514 nm (Ar<sup>+</sup> ion Laser). The microscope focused the laser beam onto the surface of samples. Raman spectrum recorded from all BN samples deposited on different substrates identified Raman active E<sub>2g</sub> mode related to hexagonal or c-BN approximately at 1365 cm<sup>-1</sup>, indicates dominating hexagonal phase in BN nanostructure [28-30]. Almost similar trend in the peak profile is observed from Si substrate. The extremely

narrow Raman active  $E_{2g}$  peak probably suggests that the obtained sample has less defect concentrations. Compared with a traditional CVD method that in most cases yields high level of impurity inside the samples, the present plasma pulse beam deposition technique could produce high purity of BN nanostructures. No carbon and other impurities were detected.

## **2.7 Other Characterization Techniques (SEM, TEM, AFM, Raman, FT-IR, XRD, XPS, SAED)**

This section provides the description of the nanosheets and nanostructures characterization techniques used in this study to analyze the as-grown samples. The development of an overall understanding of bonding nature and physical nature of the nanosheets required several independent sources of data. Each of the characterization technique provides a mean by which an overall picture could be acquired. For example, in current research, different characterization techniques have been used to examine the properties of BNNSs and their crystalline structure. To obtain the sample's morphology information, the electron microscopic characterization techniques have been employed. Scanning electron microscopy (SEM) has been used to inspect surface morphology of the nanosheets. Atomic force microscope (AFM) has been employed to reveal the detail surface information such as the roughness, the high resolution morphology and so on. AFM can easily map out both the surface detail as well as the 3-D profile of the sample; therefore the residual resist can be estimated by observing the samples's top-down image and cross-section profile. The material properties of the nanosheets and nanostructures have been studied using transmission electron microscope (TEM), electron energy loss spectroscopy (EELS), selected area electron diffraction (SAED), x-ray energy dispersive spectroscopy (EDS), Raman spectroscopy and x-ray photoelectron spectroscopy (XPS) in this thesis. TEM is an important means for high resolution materials analysis and often equipped with

EELS and SAED capabilities. The detail crystalline structure of nanosheets, specially the grain structure and grain boundaries have been investigated by HRTEM and SAED. The crystalline structures of BNNSs were analyzed by Raman spectroscopy using triple monochromator (ISA J-Y Model T64000) with an excitation wavelength of 514 nm ( $\text{Ar}^+$  ion Laser). The microscope focused the laser beam onto the surface of samples. Raman scattering is the powerful, semi-quantitative method to examine the structure at global level. The  $\text{sp}^2$  and  $\text{sp}^3$  are very sensitive to Raman scattering; by analyzing the Raman spectra, the diamond signature can be easily identified. In typical Raman spectrum of BNNSs, a clear Raman active  $\text{E}_{2g}$  mode of the BN film at  $\sim 1365 \text{ cm}^{-1}$  was identified throughout the measurements, indicating the hexagonal phase dominates in BNNSs. Compared with a traditional CVD method that in some cases yields impure samples, the obtained sample via pulsed plasma beam technique could produce high purity of atomic layer BN materials.

## **2.8 Additional Related Techniques and Experiments**

Besides these techniques that are mentioned above, the electron field emission (EFE) measurements, cathodoluminescence measurements have been conducted in thesis work.

### **2.8.1 Optical and Electrical Characterization Techniques for BNNSs**

Optical characterization of BNNSs was done by measuring cathodoluminescence (CL) spectra. In a typical CL experiment, samples were mounted on the cold finger of a closed-cycled helium refrigerator operating down to 6 K. The CL was generated by the Staib Instruments, Inc. electron gun EK-20-R system being in common vacuum (of  $1 \times 10^{-7}$  Torr) with the cryostat. The electron beam was incident upon the sample at a  $45^\circ$  angle from an electron gun. The CL depth of the excitation could be easily varied by varying the electron acceleration voltage between 500 eV up to 20 keV. Samples were excited with an electron acceleration voltage of 6 keV and

current density of  $1.2 \mu\text{A}/\text{mm}^2$ . The resulting CL spectra were dispersed by a 0.3 m Acton spectrograph and analyzed by a Princeton Instrument PI-MAX CCD camera equipped with UV intensifier, operating in the spectral region 190–950 nm.

### 2.8.1.1 Cathodoluminescence Spectroscopy

Cathodoluminescence is an optical and electromagnetic phenomenon in which electrons impacting on a luminescent material such as a phosphor, cause the emission of photons which may have wavelengths in the visible spectrum. A familiar example is the generation of light by an electron beam scanning the phosphor-coated inner surface of the screen of a television that uses a cathode ray tube. Cathodoluminescence is the inverse of the photoelectric effect in which electron emission is induced by irradiation with photons. The block diagram of the process is shown in Fig. 2.3.

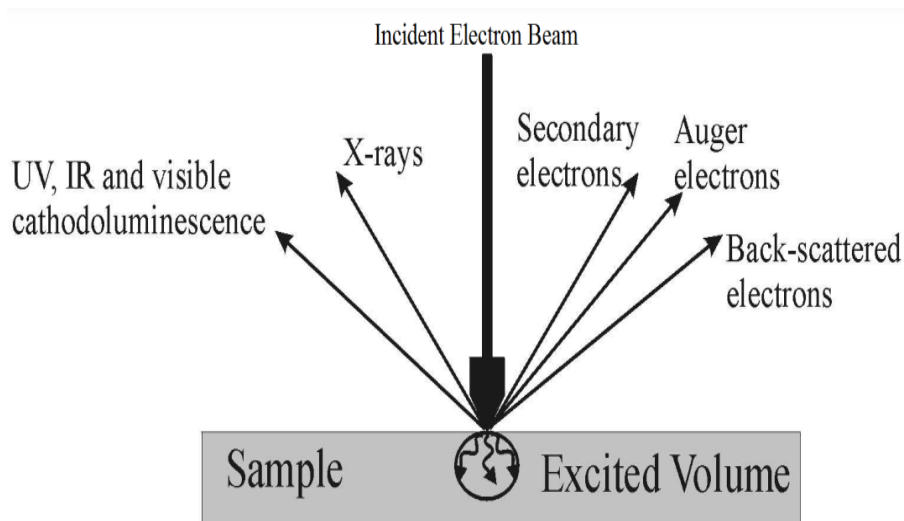


**Figure 2.3** Schematic diagram of the cathodoluminescence process.

Cathodoluminescence occurs because the impingement of a high energy electron beam onto a semiconductor will result in the promotion of electrons from the valence band into the conduction band, leaving behind a hole. When an electron and a hole recombine, it is possible

for a photon to be emitted. The energy (color) of the photon, and the probability that a photon and not a phonon will be emitted, depends on the material, its purity, and its defect state. In this case, the "semiconductor" examined can, in fact, be almost any non-metallic material. In terms of band structure, classical semiconductors, insulators, ceramics, gemstones, minerals, and glasses can be treated the same way.

#### **2.8.1.2 Field Emission Characterization**

The energy required to extract an electron from the Fermi level  $E_f$  of a neutral solid to a rest position in the vacuum not too far away from the surface is termed the work function, and is usually given in electron volts (eV) [26,27]. The work function has values 2-5 eV for metals and is different for different materials arises from two effects. The first, or inner potential, is the intrinsic partial free energy of "solution" of electrons in the metal and is the difference between the chemical potential (Fermi level) of the electron in the metal and that at a very large distance from it in a field free vacuum. The second component arises from electrostatic effects due to spill-out of electrons at the surface and decays slowly with distance. This spill-out causes an electron deficiency on the metal side of the solid-vacuum interface and gives rise to a condenser or dipole layer, with the negative end outermost. If the surface is rough there is a second spill-over in addition with electrons owing into the concave portions of steps and produces an opposite dipole with the positive end outward. The surface structure is therefore responsible for the crystallographic anisotropy in  $\phi$ . Similar effects can occur for adsorbed molecules on the surface. In thermionic emission and photoemission electrons are given sufficient energy to overcome the potential step of at the surface of a solid. In field emission (FE) on the other hand, the step is deformed into a potential barrier so that the unexcited electrons can leak or tunnel out it. This situation is depicted in Fig. 2.4 [28].

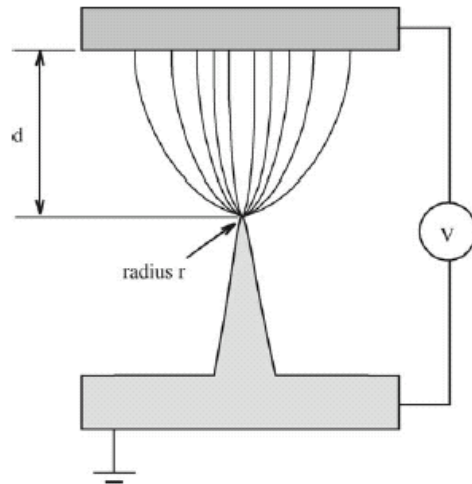


**Figure 2.4** Illustration of field electron emission from a tip.

When a field  $E$  is applied to the surface, electrons close to the Fermi level  $E_f$  will see a barrier height and thickness  $d = \phi / eE$  (to a first approximation). If this is thin (2 nm) enough, the electrons of the conducting material will have a finite probability of tunneling. However the electrons do not terminate sharply at the interface so the triangular potential barrier is only a first approximation to the shape of  $V(x)$  at the surface. Besides the potential  $V(x)$  near the surface is decreased by an image term  $1/(4\epsilon_0) e^2 / 4x$  which lowers the effective potential barrier. The typical distribution of the field emitted electrons as a function of the normal energy is indicated in Fig. 2.4. The intensity of the FE electrons is higher close to  $E_f$  as a result of the increased thickness of the barrier for energies below  $E_f$ .

## 2.9 Conclusions

In summary, CO<sub>2</sub>-PLD system was successfully installed for the quick synthesis of high purity mass product nanostructures and thin films. The best vacuum of the system achieved down to  $10^{-7}$  Torr, and substrate temperature was controlled up to  $(1 \pm 10\%) \times 1000$  °C.

## 2.10 References

- [1] Song L, Ci L, Lu H, Sorokin P B, Jin C, Ni J, Kvashnin A G, Kvashnin D G, Lou J, Yakobson B I, Ajayan P M (2010) Large scale growth and characterization of atomic hexagonal boron nitride layers. *Nano Lett.* 10: 3209—3215. doi: 10.1021/nl1022139.
- [2] Ismach A, Chou H, Ferrer D A, Wu Y, McDonnell S, Floresca H C, Covacevich A, Pope C, Piner R, Kim M J, Wallace R M, Colombo L, Ruoff R S (2012) Toward the Controlled Synthesis of Hexagonal Boron Nitride Films. *ACS nano.* 6: 6378–6385. doi: 10.1021/nn301940k
- [3] Kim K K, Hsu A, Jia X, Kim S M, Shi Y, Hofmann M, Nezich D, Rodriguez-Nieva J F, Dresselhaus M, Palacios T, Kong J (2012) Synthesis of Monolayer Hexagonal Boron Nitride on Cu Foil Using Chemical Vapor Deposition. *Nano Lett.*, 12: 161–166. dx.doi.org/10.1021/nl203249a.
- [4] Y. J. Cho, C. H. Kim, H. S. Kim, J. Park, H. C. Choi, H. J. Shin, G. Gao, H. S. Kang: Electronic Structure of Si-Doped BN Nanotubes Using X-ray Photoelectron Spectroscopy and First-Principles Calculation. *Chem. Mater* 21, 136 (2009).
- [5] S. Bernard, V. Salles, S. Foucaud, P. Miele: Boron Nitride Nanoparticles: One-Step Synthesis from Single-Source Pre-ceramic Precursors. *Advances in Science and Technology* 62, 1 (2010).
- [6] C. Zhi, Y. Bando, C. Tang, H. Kuwahara, D. Golberg: Large-Scale Fabrication of Boron Nitride Nanosheets and Their Utilization in Polymeric Composites with Improved Thermal and Mechanical Properties. *Advanced Materials* 21, 2889 (2009).
- [7] Y. Lin, T. V. Williams, J. W. Connell: Soluble, Exfoliated Hexagonal Boron Nitride Nanosheets. *J. Phys. Chem. Lett.* 1, 277 (2010).
- [8] Y. Lin, T. V. Williams, W. Cao, H. E. E Ali, J. W. Connell: Defect Functionalization of Hexagonal Boron Nitride Nanosheets. *J. Phys. Chem. C* 114, 17434 (2010).
- [9] J. C. Meyer, A. Chuvilin, G. Algara-Siller, J. Biskupek, U. Kaiser: Selective sputtering and atomic resolution imaging of atomically thin boron nitride membranes. *Nano Lett.* 9, 2683 (2009).
- [10] M. Cote, P. D. Haynes, C. Molteni: Material design from first principles: the case of boron nitride polymers. *J. of Physics-Condensed Matter* 14(42), 9997 (2002).
- [11] Akiyoshi Chayahara, Haruki Yokoyama, Takeshi Imura and Yukio Osaka; *Jpn. J. Appl. Phys.* 26 L1435 doi:10.1143/JJAP.26.L1435.
- [12] K. Kyoungwon, S. Yong-Won, C. Seongpil, K. In-Ho, K. Sangsig, Y. L. Sang: Fabrication and characterization of Ga-doped ZnO nanowire gas sensor for the detection of CO. *Thin Solid Films* 518, 1190 (2009).
- [13] U. Ozgur, Ya.I. Alivov, C. Liu, A. Teke, M.A. Reshchikov, S. Dogan, V. Avrutin, S.-J. Cho, and H. Morkoc, *Journal of Applied Physics* 98, 041301 (2005).
- [14] Operations & Service Manual, Hummer 8.3 RF & DC Power Supplies Deposition System, Anatech Ltd. Union City, CA, 2006.

- [15] E. Kay, J. Appl. Phys. 34, 760 (1963).
- [16] U. Ozgur, Ya.I. Alivov, C. Liu, A. Teke, M.A. Reshchikov, S. Dogan, V. Avrutin, S.-J. Cho, and H. Morkoc, Journal of Applied Physics 98, 041301 (2005).
- [17] Operations & Service Manual, Hummer 8.3 RF & DC Power Supplies Deposition System, Anatech Ltd. Union City, CA, 2006.
- [18] E. Kay, J. Appl. Phys. 34, 760 (1963).
- [19] Harish Kumar Yadav, Ph.D Thesis, chapter 2, 2008.
- [20] S.M. Metev and V.P. Veiko, Laser Assisted Microtechnology, Springer, Berlin, Heidelberg, 1994.
- [21] D.B. Chrisey and G.K. Hubler, Pulsed Laser Deposition of Thin Film, John Wiley & Sons, Inc., New York, 1994.
- [22] Vinay Gupta and K. Sreenivas, Pulsed laser deposition of Zinc Oxide, Chapter 4, Edited by C. Jagadish and S. Pearton, Elsevier Limited, 2006.
- [23] J. F. M. Cillessen, R. M. Wolf, J. B. Giesbers, P. W. M. Blom, K. O. Grosse-Holz, E. Pastoor, Applied Surface Science, 96-98, 744 (1996).
- [23] B. L. Zhu, X. Z. Zhao, F. H. Su, G. H. Li, X. G. Wu, J. Wu and R. Wu, Vacuum, 84, 1280 (2010).
- [24] P. X. Feng, H. X. Zhang: Properties of nanostructured cubic boron nitride films prepared by the short-pulse laser plasma deposition techniques. Int. Journal of Refractory Metals and Hard Materials 27, 823 (2009).
- [25] Y. Noorhana, H. G. Beh, H. Mansor: Development of pulsed laser deposition system for the formation of Web-like carbo nanotubes. American Journal of Applied Sciences 2(11), 1546 (2005).
- [26] G. N. Fursey, Applied Surface Science 215, 1 (2003).
- [27] V. I. Merkulov, D. H. Lowndes, L. R. Baylor and S. Kang, Solid-State Electronics 45, 949 (2001).
- [28] N.S. Xu, S.Ejaz Huq, Materials Science and Engineering, R 48, 47-189(2005).



## CHAPTER 3

### Synthesis and Electron Microscopic Characterization of BNNSs

So far, significant theoretical and experimental efforts have been made to synthesize 1-dimensional (1D) and 2D and 3D atomic structures of BN material; e.g. BN nanotubes, nanoribbons (BNNRs) [1], mono-layer BN nanosheets [2-4], and c-BN thin films [5]. The interest in growing large area 2D mono-layer or few-layers BNNSs is at the forefront of material science research due to the fact that BNNSs has potential to graphene in some applications. However, growing quality BNNSs consisting of only several atomic layers remains a challenge. In this chapter, we report on the synthesis of large scale single crystal and polycrystalline BNNSs and their electron microscopic characterizations.

#### 3.1 Experimental Method to Obtain Single Crystal and Polycrystalline BNNSs

To obtain single crystal and polycrystalline nanosheets, we set specific experimental parameters in the present experiment. A pyrolytic hexagonal boron nitride target irradiated using a CO<sub>2</sub> laser beam operated at 10.6  $\mu\text{m}$  wavelength, pulse width of 1  $\mu\text{s}$  to 5  $\mu\text{s}$ , frequency of 5 Hz and energy of 5 Joules per pulse. The laser beam was focused onto the target with a 30 cm focal length ZnSe lens and incident angle 45 degrees relative to the surface of the rotating target (about 200 rpm). The power density of the laser on the target was controlled at  $2 \times 10^8 \text{ W/cm}^2$  per pulse. The first experiment was conducted in low vacuum (0.20 Pa) and the second experiment was conducted in H<sub>2</sub> environment (26 Pa). The other experimental parameters (substrate temperature, substrate to target distance, substrates material and laser power) were kept identical in each experiment. Three materials were used as substrates: aluminum nitride (AlN), silicon (Si)

and molybdenum (Mo). Prior to the deposition, Mo disks were polished with diamond paste and cleaned with acetone and rinsed with deionized water. The commercial Si and AlN wafers were cleaned with acetone. For each experiment, the set of three different substrates (AlN, Si, Mo) was placed in the chamber at once. The distance between the substrates and the target was fixed at 3 cm. The substrates were heated upto 350 °C and the deposition process was carried out for 10 minutes. The first set of three samples (S<sub>1</sub> with AlN, S<sub>2</sub> with Si and S<sub>3</sub> with Mo) was prepared in vacuum and the second set of three samples (S<sub>4</sub> with AlN, S<sub>5</sub> with Si and S<sub>6</sub> with Mo) was prepared in H<sub>2</sub> atmosphere. The description of the sample codes and experimental parameters are given in Table I.

**Table I. Summary of the experimental conditions under which the CO<sub>2</sub>-PLD was carried out.**

Sample ID	Preparation Conditions		
	Substrate Material	Deposition atmosphere	Pressure (Pa)
S <sub>1</sub>	AlN	Vacuum	0.2
S <sub>2</sub>	Si	Vacuum	0.2
S <sub>3</sub>	Mo	Vacuum	0.2
S <sub>4</sub>	AlN	Hydrogen	26
S <sub>5</sub>	Si	Hydrogen	26
S <sub>6</sub>	Mo	Hydrogen	26

### 3.2 Effect of Deposition Environment in the Synthesis of BNNSs

In PLD technique, deposition environment plays a critical role in the synthesis of BNNSs. In order to analyze effect of deposition environment in the synthesis, morphology and crystallization of BNNSs, we performed different experiments in low vacuum and H<sub>2</sub> atmosphere. The deposition performed in vacuum at a pressure of 0.2 Pa, from which we

obtained polycrystalline BNNSs, and in  $H_2$  atmosphere at a pressure of 26 Pa, we obtained single-crystal BNNSs. The presence of  $H_2$  seems to minimize the side effects of sputtering and the material shows higher purity and better crystallinity. It is obvious that during ablation process, large amount of high energy ions and clusters generate in highly forward direction as shown in Fig. 3.1a. These ions and clusters can directly interact with the substrate surface and damage the substrate surface or initially grown nanosheets. This mostly happens when the deposition is performed in vacuum as shown in Fig. 3.1a. However, in the present study, we minimized the side effects of sputtering using background gas as deposition environment as shown in photograph Fig. 3.1b. The laser induced plasma ions and heavy clusters, first passed through the collisions with the background gas molecules, eliminated or lost their energy, consequently, high quality atomically thin BNNSs were obtained.

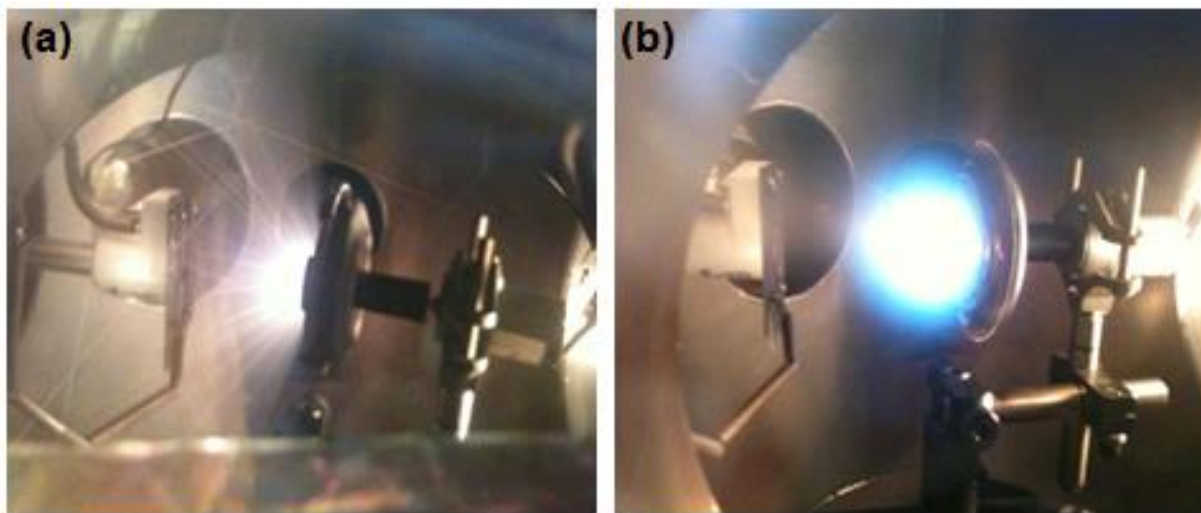


**Figure 3.1** Synthesis of BNNSs at different atmosphere, (a) in vacuum, (b) in  $H_2$  respectively.

Generally, for an ion impacting to surface to do damage to that surface it must have incident energy large enough to displace surface atoms and cause an irreversible change to the

lattice. The change of the lattice is usually termed as radiation damage. If the incident energy is not large enough, the energy of the ions transfer to surface through collision with the surface atom dissipated as heat through excitation of lattice phonons. This collision process is known as knock on momentum transfer. Because the ion does not follow the line of least resistance through the solid after impact, and because atoms in the lattice neighboring the displaced atom do not have time to relax out of the way of the displacing atom the ion energy has to be several time larger than the sublimation energy in order to displace surface atom. Therefore the displacement of the atoms creates defects with in the lattice.

The synthesis process carried out in vacuum, laser produced high-energy plasma ions interact directly with the substrates surfaces which possibly knock out atoms from initially deposited layers resulting in atomic defects in BNNSs. While, synthesis in  $H_2$  environment, collision or interaction of plasma ions with  $H_2$  gas molecules are taken in to account from which two possible results would be raised, 1) sputtering effect would be greatly reduced because collision would moderate particles energy in plasma beam, 2) due to collisions and plasma ions and electron impact ionization of  $H_2$  gas,  $H^+$  ions created and their interaction would help to etch the oxygen from the substrates surfaces. This explains the drastically diminution of oxygen impurities within BNNSs. Consequently, the obtained samples have much less oxygen content; as a result atomic defect free nanosheets could be obtained. A similar effect of hydrogen etching was reported for the formation of defects free carbon nanosheets produced by radio frequency plasma enhanced CVD [6]. Ben Moussa et al. [7] also used pure hydrogen plasma before the deposition process to remove possible oxygen residuals in the deposition chamber to grow pure 2D nanowall structures. Based on obtained experimental data and above discussion, we can conclude that synthesis in  $H_2$  environment could yield high-quality BNNSs.

### 3.3 Results

As synthesized BNNSs were surveyed using X-ray diffraction (Siemens- Bruker Diffractometer D5000) and examined using SEM and TEM. The SEM images were recorded using a JEOL JSM-7500F equipped with a transmission electron detector (TED). TEM data were recorded using a Carl Zeiss LEO 922 EFTEM and a JEOL JEM-2200FS HRTEM. Nanosheets were also characterized using a Raman spectrometer (triple monochromator: ISA J-Y Model T64000) and a Fourier transform infrared spectrometer (FT-IR: Bruker Tensor 27).

#### 3.3.1 Electron Microscopic Results

Figure 3.2 show two SEM images recorded from samples  $S_1$  (prepared in vacuum) and  $S_4$  (prepared in  $H_2$ ). The image of sample  $S_1$  is shown in Fig. 3.2 (a), whereas a sample  $S_4$  is shown in Fig. 3.2 (b). In each case, the entire surface of the substrates was covered with a large amount of BN flakes. The BN flakes of sample  $S_1$  were bended, curled and sometimes were flat as marked with arrows shown in Fig. 3.2 (a). In contrast, sample  $S_4$  (Fig. 3.2 (b)) seemed to have most BN flakes flat. Moreover, the edges of the samples are usually bended and curled making it difficult to determine their accurate thicknesses using SEM micrographs. SEM images recorded from other four samples also show similar contrast in morphologies.

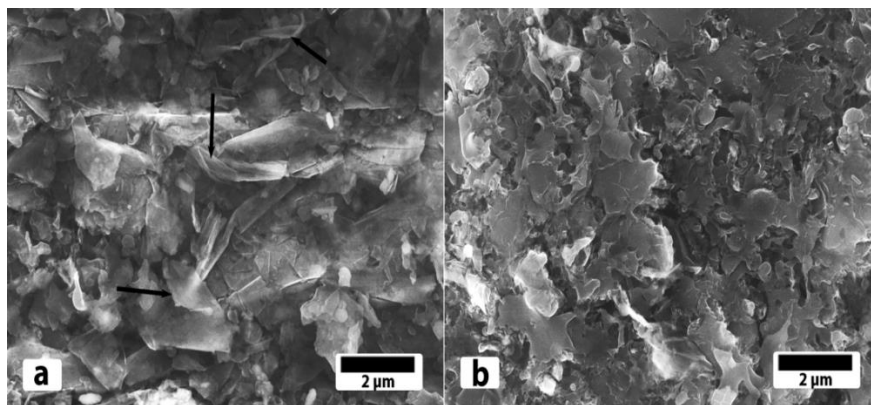


**Figure 3.2** SEM images recorded from samples (a)  $S_1$  and (b)  $S_4$ .

### 3.3.2 TEM and SAED Results

TEM images recorded from the samples  $S_1$  and  $S_4$  are shown in Fig. 3.3 (a,b). Both samples ( $S_1$  synthesized in vacuum and  $S_4$  synthesized in  $H_2$  environment) show that BN flakes are composed of several BNNSs. These nanosheets have a layered structure. Sample  $S_4$  is mainly composed of flat BNNSs that are transparent to electron beam (Fig. 3.3 b). The insets in Fig. 3.3 (a,b) show the corresponding electron diffraction (ED) patterns. They are single-crystalline or polycrystalline and both were indexed to the  $h$ -BN structure. The ED of sample  $S_1$  shows five diffraction rings indexed to  $\{002\}$ ,  $\{100\}$ ,  $\{101\}$ ,  $\{004\}$  and  $\{110\}$  planes (Fig. 3.3 a). The pattern of sample  $S_4$  is indexed to  $h$ -BN with the zone axis along the  $[-1\ 1\ -1]$  direction (Fig. 3.3b). High resolution TEM (HRTEM) studies were conducted to further identify the morphology, crystallinity and phase of the as-synthesized BN nanosheets. A bright field HRTEM image recorded from a thin BNNSs cluster prepared in  $H_2$  environment is shown in Fig. 3.3c. The inset is a Fast Fourier Transform (FFT) of this same image, also indexed to  $h$ -BN structure. The hexagonal honeycomb structure of six membered  $B_3-N_3$  hexagons is easily identifiable. The measured B-N distance was 0.14 nm, which is in good agreement with the value reported in literature [8]. The lattice is easily interpretable only when the BNNSs are oriented exactly perpendicular to the electron beam. The B-N distance measured was shorter than the point resolution of the microscope (0.19 nm for the JEM-2200FS when fitted with an ultra-high resolution pole piece) but remained interpretable. The average spacing between each BNNS was measured to  $0.340 \pm 0.02$  nm, corresponding to the (002) interplanar distance of  $h$ -BN (0.330 nm). Also the thicknesses of numerous BNNSs clusters were measured using several HRTEM images as shown in Fig. 3.3 (d,e). A similar method has been used previously for the measurement of average thickness of BNNSs clusters [9]. The image (Fig. 3.3 e) also shows a

thin BNNSs cluster of four stacked layers with 1.7 nm thickness. The statistical results obtained from the measurements of more than 50 BNNSs are displayed in the two histograms shown in Fig. 3.3 (f,g). The average values were estimated around 3.0 nm (representing less than 10 BNNSs) for samples prepared in  $H_2$  and around 5.0 nm for samples prepared in vacuum, respectively. Using a hydrogen environment for the synthesis of BNNSs therefore tends to produce thinner clusters.

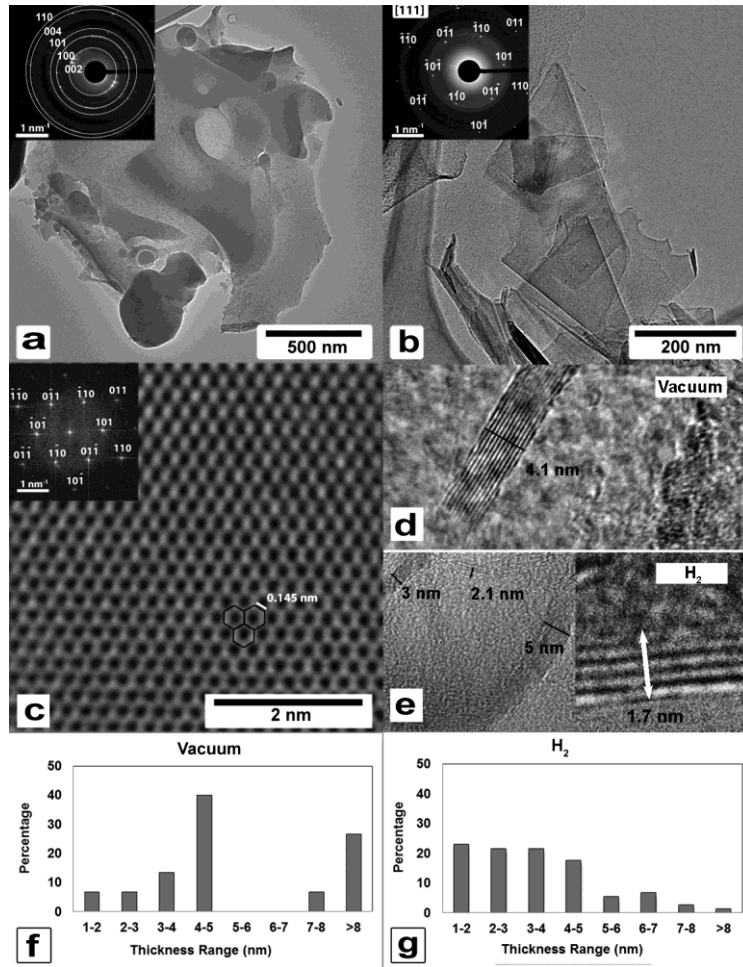


**Figure 3.3** TEM images of BNNSs recorded from sample S<sub>1</sub> (a) and sample S<sub>4</sub> (b). The insets show electron diffraction patterns, indexed to *h*-BN. A HRTEM image recorded from a BNNSs of sample S<sub>4</sub> is shown in (c) where the hexagonal structure is clearly visible: the inset is a FFT also indexed to *h*-BN. Using HRTEM images for synthesized samples in vacuum (d) and hydrogen (e) atmospheres, the thicknesses of the BNNSs

clusters were measured and the statistical results are displayed in (f, vacuum) and (g, hydrogen).

### 3.3.3 XRD Results

XRD were recorded from all six samples and the results are shown in Fig. 3.4: samples  $S_1$  and  $S_4$  (a), samples  $S_2$  and  $S_5$  (b) and samples  $S_3$  and  $S_6$  (c). The black lines represent the spectra recorded from BNNSs grown in vacuum and the red ones correspond to the spectra of BNNSs prepared in  $H_2$  environment. A high intensity peak centered at  $2\theta \approx 26.9^\circ$  was present in all XRD, identified to  $h$ -BN (002) phase [10-12]. However, for samples grown in  $H_2$  atmosphere, the  $h$ -BN (002) peaks were more intense suggesting better crystallinity. The XRD pattern also contains (100) and (101) peaks indicating the presence of different phases of  $h$ -BN as identified in ED patterns. A peak positioned at  $2\theta \approx 27.8^\circ$  is also identified. This is related to  $B_2O_3$  content present in the BNNSs. The other high intensity peaks in the spectra belong to the AlN substrates.

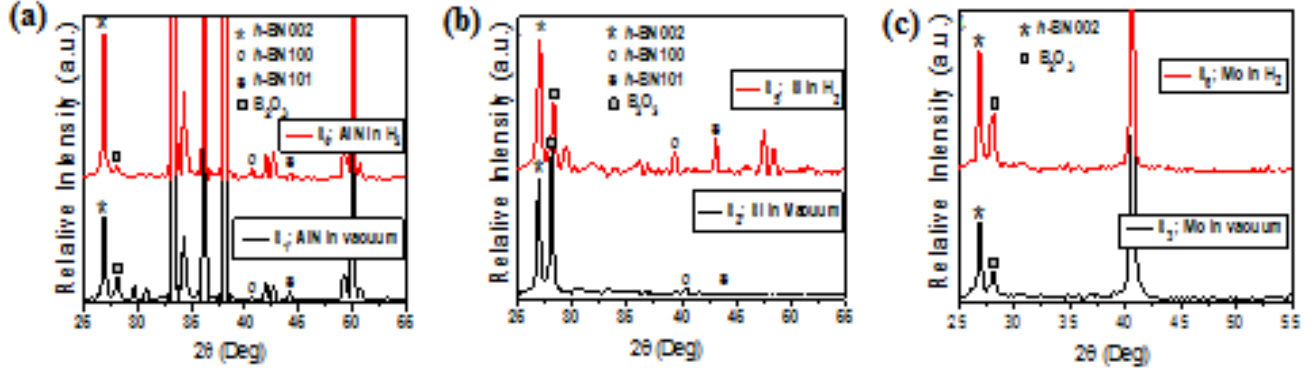


**Figure 3.4** A comparison of XRD patterns recorded from BNNSs (a)  $S_4$  and  $S_1$ , (b)  $S_5$  and  $S_2$ , (c)  $S_6$  and  $S_3$ .

### 3.3.4 Raman Results

The results obtained from Raman spectroscopy are presented in Fig. 3.5(a-c). A Raman active  $E_{2g}$  mode at approximately  $1365\text{ cm}^{-1}$  corresponding to  $h$ -BN [13-15] could be identified in all samples. However,  $h$ -BN peaks were more intense for samples grown in the  $H_2$  atmosphere



as evidenced from XRD patterns. The results obtained from Raman spectroscopy are in good agreement with XRD measurements. Therefore, we concluded that the deposition environment has a significant effect on the crystalline structure of BNNSs.

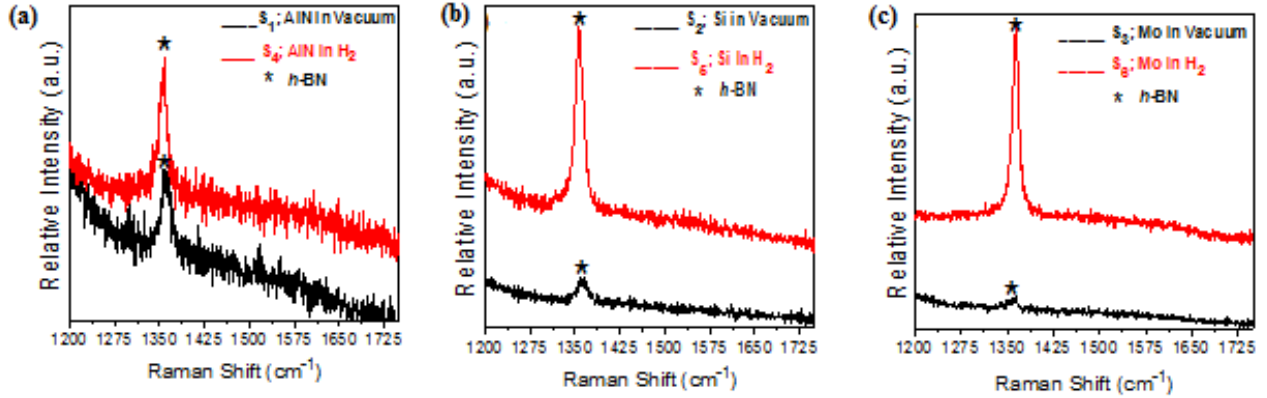


**Figure 3.5** A comparison of Raman spectra recorded from samples (a) S<sub>4</sub> and S<sub>1</sub>, (b) S<sub>5</sub> and S<sub>2</sub>, (c) S<sub>6</sub> and S<sub>3</sub>.

### 3.3.5 FT-IR Results

The typical FT-IR spectra of BNNSs recorded in attenuated total reflectance (ATR) in the transmission mode are shown in Fig. 3.6 (a-c). Samples grown in H<sub>2</sub> atmosphere showed a sharp absorption peak at 1365 cm<sup>-1</sup> which can be ascribed to the E<sub>1u</sub> (B-N stretching vibration mode perpendicular to the c-axis) modes of *h*-BN [16,17]. However, FT-IR spectra from the samples grown in vacuum showed a broad band in the range 1370-1440 cm<sup>-1</sup> associated with in-plane E<sub>1u</sub> B-N bond stretching vibration in *h*-BN phase which is similar to the results obtained from polycrystalline *h*-BN by Yu *et al.* [18]. A strong absorption peak positioned at ~1190 cm<sup>-1</sup> related to B<sub>2</sub>O<sub>3</sub> deformation mode [19] is identified in the vacuum samples indicating high B<sub>2</sub>O<sub>3</sub> content in the samples. It might be possible that the peak broadening of *h*-BN, as we noticed in vacuum samples is due to stress induced by subsequent B<sub>2</sub>O<sub>3</sub> contents in BNNSs. The peak of B<sub>2</sub>O<sub>3</sub> deformation mode appeared with less intensity in H<sub>2</sub> samples, indicating that the BNNSs

are relatively well crystallized, which may be a result of the etching effect of  $H^+$  ions in the gas phase.

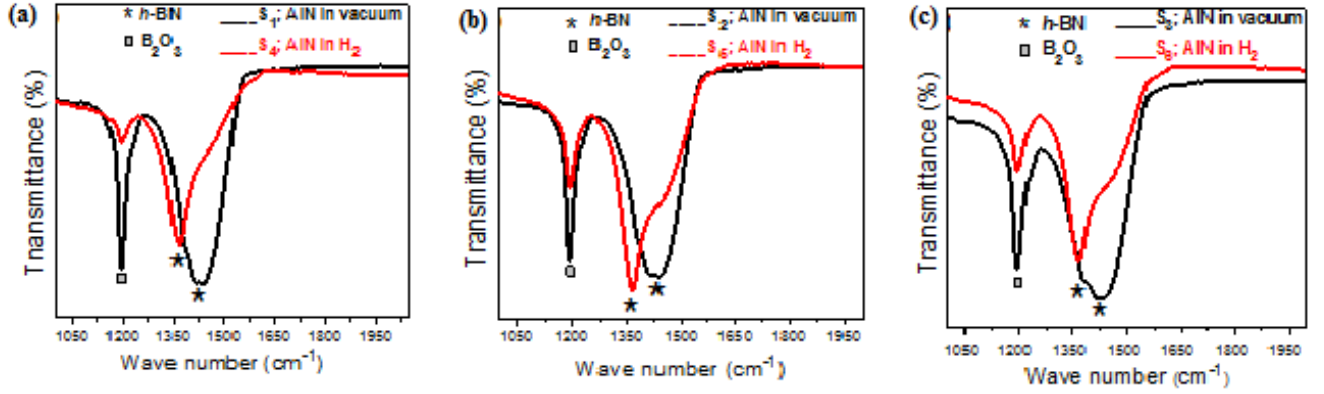


**Figure 3.6** A comparison of FT-IR spectra of BNNSs (a)  $S_1$  and  $S_4$ , (b)  $S_2$  and  $S_5$  (c)  $S_3$  and  $S_6$ .

### 3.3.6 EDS Results

Energy dispersive X-ray spectroscopy (EDS) of selected BNNSs prepared on Si substrate is presented in Fig. 3.7. EDS shows that nanosheets are mainly composed of B and N species. A small amount of oxygen is also detected that could possibly come from air to the surface of nanosheets [20].

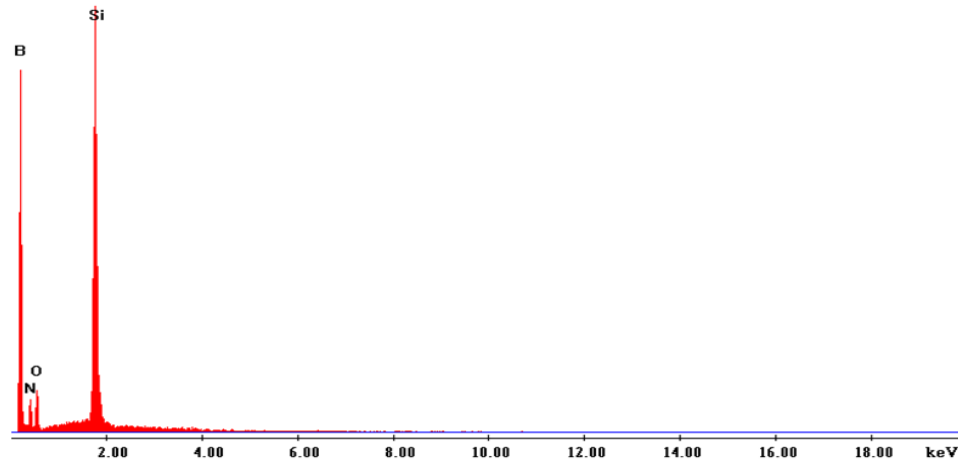


**Figure 3.7** EDS spectrum of BNNSs.

### 3.3.7 XPS Analysis of BNNSs

X-ray photoelectron spectroscopy (XPS) study of each BNNSs sample prepared in vacuum and in H<sub>2</sub> atmosphere is studied independently. Results are shown in Fig. 3.8 in which B 1s and N 1s peaks are clearly observed. As it is clear, the binding energy for B in BNNSs is at 190 eV, while binding energy of N is at 398.1 eV respectively, clearly indicating the elemental composition mostly composed of or totally based on B and respective N elements. Binding of N in BN = 398.1 eV. Besides B and N, additional peaks related to C, O, comes from atmosphere while Si and Mo peaks belong to the substrates. For example peaks at 101eV belong to Si 2p (actual position is at 99eV) and at 153eV belong to Si 2s (actual position is at 151eV). Similarly, peak at 232eV belong to Mo 3d<sub>3/2</sub> actual position is at 231eV and peak at 1064eV belong to Mo auger lines (MNV) actual position is at 1066eV. Peak of Mo 3d<sub>5/2</sub> at is not observed in addition to 3d<sub>3/2</sub> [21].

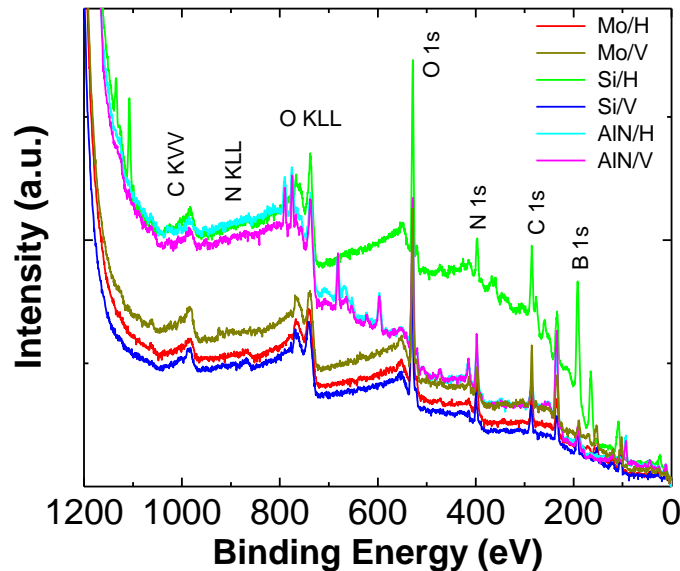


**Figure 3.8** XPS spectra of BNNSs samples prepared in Vacuum (Si/V, Mo/V, AlN/V) and H<sub>2</sub> (Si/H, Mo/H, AlN/H) environment respectively.

XPS which is a quantitative spectroscopic technique for surface characterization was also conducted to investigate the composition of BN membranes before and after plasma treatment. The XPS spectra of the hydrogen plasma-treated BNNSs are presented in Figure 3.8 (b–c). The hydrogen plasma-treated h-BN membranes present a B 1s-core level at 190.6 eV and the N 1s peak is located at 398.2 eV, which is close to the reported position of h-BN [22]. However, the plasma-treated h-BN show broader features than pure h-BN membranes. On the basis of the literature, [22–24] the N 1s and B 1s core of hydrogen plasma-treated h-BN membrane was deconvoluted into two components, shown in Fig. 3.8 (b–c).

### **3.3.8 Mechanism for the Formation of BNNSs**

The formation of BNNSs depends on the dynamics of laser-produced plasma beam, the pressure of the background atmosphere in the chamber, density of plasma species, self-induced electric field inside the plasma, the kinetics of plasma species, the temperature of the substrates, collisions between the active species of BN, the deposition time and other growth conditions such as the distance between the target and the substrates, and the angle of the substrate with plasma beam. Normally, nanosheets grow along the direction where the epitaxial energy of BN species is minimized. Taking these parameters into account, a tentative interpretation of the mechanisms for the formation of BNNSs is following. When the laser beam impacts the target surface, it generates a plasma plume out of the target surface directed toward the surfaces of the substrates. This plasma plume is composed of high-energy BN ions and clusters. These ions and clusters land onto the substrates, the extra thermal activation besides substrates heating provides energy exchange through collisions between the active ions and clusters of BN [25–26]. As a result, B and N ions make covalent bonds and arrange themselves in a honeycomb network of alternative  $B_3-N_3$  hexagonal rings. For further growth process, incoming B and N ions also attach

covalently with the side facet of the  $B_3-N_3$  ring, consequently a 2D orderly repeating pattern of hexagonal rings extends parallel to the substrates surface. Therefore, during first few seconds of the deposition, BN layer grows parallel to the substrate surface unless the edge of BN nanosheet bends and a new layer starts growing on the top of initially deposited layer and so on. The multiple sets of small BN layers grow that coalesce and form finite BN nanosheets. Previously, a mechanism has been proposed for the growth of BNNSs using CVD method [27]. However, our technique for the synthesis of BNNSs using PLD is somewhat different from that of CVD. The plasma plume might contribute in the growth process of nanosheets by providing high concentration of activated BN species and producing strong electric field which may enhance the field-induced surface species migration that helps B and N ions to make covalent bonds [28]. The detailed growth mechanism of BNNSs needs further to be investigated.

It should be mentioned that the synthesis of BNNSs in the normal vacuum condition, the surface of the sample may be contaminated because of the large amount of particles (molecules) from residual gas will collide with the surface, and parts of them will be deposited on the sheets. In order to largely reduce impurities, the growth rate of sheet should be higher. In the present case of synthesis, the growth rate is much faster than that of the reported growth rate for CVD. Yu et al. conducted 180 min of CVD but he was not able to find any BNNSs at the first 30 minutes of deposition [29]. In our case, few seconds of deposition yielded BNNSs fully covering entire surfaces of substrates indicating high growth rate. Moreover, we noticed from HRTEM images that the obtained nanosheets are mostly defects free although the formation of BNNSs is particularly sensitive to the side effects of sputtering as well as the presence of oxide content on the surface of the substrates.

### 3.3.9 Vertically Aligned BNNSs

An SEM image recorded from the surface of a sample is shown in Fig. 3.9 (a). Entire substrate surface was covered with the large number of feather-like BNNSs with mixed vertical and horizontal orientations with respect to the substrate. The alignment of the BNNSs is possibly induced by the electrical field generated in plasma sheath [30]. Area size of BNNSs upto  $100 \times 100 \mu\text{m}^2$  and thickness  $\sim 1 \mu\text{m}$  were estimated from an arbitrarily selected vertically standing BNNSs (Fig. 3.9 (b)). Figure 3.9 (b) shows close view of BNNS indicating compact disk-like morphology where each disk is further composed of several ultra-thin layers of BN nanosheets. These layers are highly flat and transparent to the electron beam; however, at the same time the vertically aligned BNNSs are more clearly visible. The general interpretation of the deposition mechanism is already provided in previous section. This process helps to grow the small BN layers that coalesce and transform into horizontally and vertically aligned BNNSs. However, the process of horizontal and vertical growth of the nanosheets is random. In the case of vertical BNNSs, a planar growth stage can be observed in which the base layer is flat and parallel to the substrate [14]. After the development of sufficient force onto the grain boundaries the leading edge of the top layer curled upward, that is an intrinsic property of 2D structure [31], and the vertical growth of the BNNSs begins. On the other hand, it could also be possible that BN species diffuse towards the surface of initially growing layer instead of the edge of the layers due to weak Van der Waals forces connecting them to the substrate. We believe that the high thermal mobility of the synthesized BNNS accelerates diffusion of adsorbed B and N atoms along the surface towards the edges of the nanosheets and covalently bond them with the BNNSs edge atoms. Consequently, the nanosheets start growing horizontally rather than vertically. So far, SEM measurements were not enough to collect the sufficient information of the geometrical

alignment of nanosheets. Therefore, we used AFM to collect 3-Dimensional image from the surface of sample and result is presented in Fig. 3.9 (c). The surface texture clearly indicates large number of BN nanosheets. These sheets are highly flat and vertically aligned on the substrate surface; distributed in layer by layer and suspended in parallel to each other. Such suspending geometry of the nanosheets can yields substantial improvement in device quality; and impose better device architecture and functionality. Some part of the sample was composed on conical shape with sharp tip on top; that can enhance the emission of charge even at low applied field.

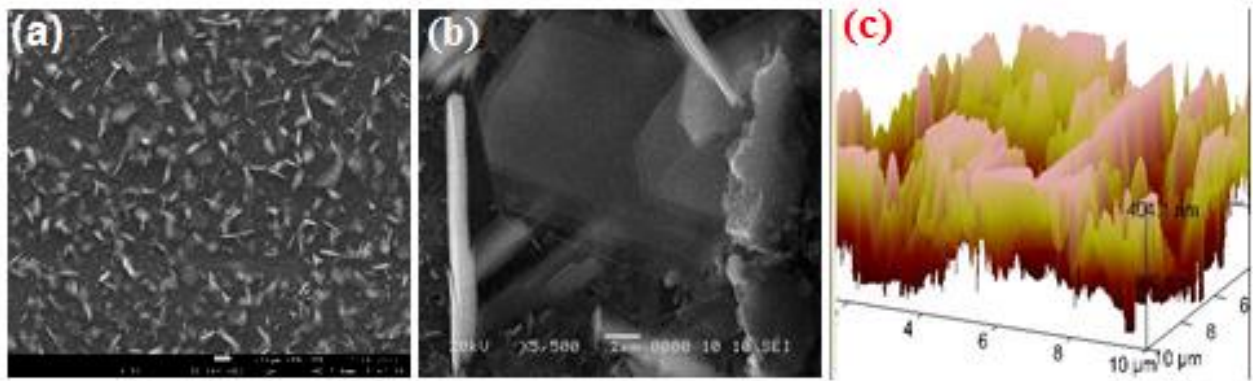


**Figure 3.9** (a,b) SEM images of horizontally and partially vertically aligned BNNSs. (c) AFM micrographs; indicating vertically aligned BNNSs. Scalar bars are shown on images.

### 3.4 Conclusions

In summary, a material assembly of a few atomic layers of BNNSs was synthesized using CO<sub>2</sub>-PLD technique. Digitally controlled pulse deposition techniques produced fast, large-size BNNSs. Two conclusions can be made from the present experiments: 1) the substrate temperature of 300 °C is the critical point in synthesis of high-quality BNNSs. Single crystalline BNNS would be not possibly synthesized at too low temperature; and 2) because of scattering,

effect of temperature on the resistivity/conductivity of 3D bulk materials or thick films is inevitable.

The deposition environment played an important role in obtaining single crystal and polycrystalline of BNNSs. The size, shape, thickness, density, and alignment of the BNNSs were well-controlled by appropriately changing the growth conditions. The synthesis in  $H_2$  environment minimized the side effects of sputtering; consequently atomic defects-free, few atomic layer BNNSs were achieved. The thicknesses of obtained BNNSs were observed 1.5 nm that can further be reduced down to single atomic layer by carefully optimizing the deposition parameters. HRTEM, electron diffraction, XRD, and Raman spectroscopy clearly interprets hexagonal crystalline structure in the nanosheets. XPS identified dominating B and N elements in synthesized BNNSs. Sometimes BNNSs were observed with mixed geometrical shape e.g. horizontal and partially vertical alignment under appropriate synthesis conditions. Though BNNSs are wide band-gap semiconductor and they were barely reported as field emission candidate; the vertically aligned BNNSs could possible emit enough charge as the edges of BNNSs are very sharp.



### 3.5 References

- [1] Zhi-Gang Chen, Jin Zou, Gang Liu, Feng Li, Yong Wang, Lianzhou Wang, Xiao-Li Yuan, Takashi Sekiguchi, Hui-Ming Cheng and Gao Qing Lu; ACS Nano, 2008, 2 (10), pp 2183–2191; DOI: 10.1021/nn8004922; Novel Boron Nitride Hollow Nanoribbons.
- [2] D. Pacile, J. C. Mayer, C. O. Girit, A. Zettl, Appl. Phys. Lett. 92 (2008) 133107-133109.
- [3] D. Golberg, Y. Bando, M. Eremets, K. Takemura, K. Kurashima, H. Yusa, Appl. Phys. Lett. 69 (1996) 2045-2047.
- [4] I. Mohai, M. Mohai, I. Bertoti, Z. Sebestyen, P. Nemeth, I. Z. Babievskaya, J. Szepvolgyew, Diam. Relat. Mater. 20 (2010) 227-231.
- [5] K. Inagawa<sup>1</sup>, K. Watanabe<sup>1</sup>, H. Ohson<sup>1</sup>, K. Saitoh<sup>1</sup> and A. Itoh J. Vac. Sci. Technol. A 5, 2696 (1987); <http://dx.doi.org/10.1116/1.574722>; Preparation of cubic boron nitride film by activated reactive evaporation with a gas activation nozzle.
- [6] Mingyao Z, Jianjun W, Brian C H, Outlaw R A, Xin Z, Kun H, Shutthanandan V, Dennis M M (2007) A mechanism for carbon nanosheet formation. Carbon 45: 2229–2234. doi:10.1016/j.carbon.2007.06.017.
- [7] Moussa B B, Haen J D, Borschel C, Barjon J, Soltani A, Mortet V, Ronning C, Olieslaeger M D, Boyen H-G, Haenen K (2012) Hexagonal boron nitride nanowalls: physical vapour deposition, 2D/3D morphology and spectroscopic analysis. J. Phys. D: Appl. Phys. 45: 135302 (8pp) doi:10.1088/0022-3727/45/13/135302.
- [8] Jin C, Lin F, Suenaga K, Iijima S (2009) Fabrication of a Freestanding Boron Nitride Single Layer and Its Defect Assignments. Phys. Rev. Lett. PRL 102: 195505-1--195508. doi:10.1103/PhysRevLett.102.195505.
- [9] Zeng H, Zhi C, Zhang Z, Wei X, Wang X, Guo W, Bando Y, Golberg D (2010) White Graphenes: Boron Nitride Nanoribbons via Boron Nitride Nanotube Unwrapping. Nano Lett. 10: 5049-5055. doi: 10.1021/nl103251m.
- [10] Zhang, W. J.; Matsumoto, S. Chem. Phys. Lett. 2000, 330, 243.
- [11] Zhang, W. J.; Matsumoto, S. J. Mater. Res. 2000, 15, 2677.
- [12] Jin M S, Kim N O (2010) Photoluminescence of Hexagonal Boron Nitride (h-BN) Film. Journal of Electrical Engineering & Technology 5: 637-639. doi: 10.5370/JEET.2010.5.4.637.
- [13] Nemanich R J, Solin S A, Martin R M (1981) Light scattering study of boron nitride microcrystals. Phys. Rev. B 23: 6348-6356. doi:10.1103/PhysRevB.23.6348
- [14] Hoffman M M, Doll G L, Eklund P C (1984) Optical properties of pyrolytic boron nitride in the energy range 0.05—10 eV. Phys. Rev. B 30: 6051-6056. doi: 10.1103/PhysRevB.30.6051.
- [15] Wu J, Han W Q, Walukiewicz W, Ager J W, Shan W, Haller E E, Zettl A (2004) Raman Spectroscopy and Time-Resolved Photoluminescence of BN and BxCyNz Nanotubes. Nano Lett. 4: 647-650. doi: 10.1021/nl049862
- [16] Paine R T, Narula C K (1990) Synthetic Routes of Boron Nitride. Chem. Rev. 90, 73-91.

- [17] Chen Z G, Zou J, Liu G, Li F, Wang Y, Wang L Z, Yuan X L, Sekiguchi T, Cheng H M, Lu G Q (2008) Novel Boron Nitride Hollow Nanoribbons. *ACS Nano* 2: 2183-2191. doi: 10.1021/nn8004922.
- [18] Yu J, Qin L, Hao Y, Kuang S, Bai X, Chong Y M, Zhang W, Wang E (2010) Vertically Aligned Boron Nitride Nanosheets: Chemical Vapor Synthesis, Ultraviolet Light Emission, and Superhydrophobicity. *ACS NANO* 4: 414-422. doi: 10.1021/nn901204c.
- [19] Moon O M, Kang B C, Lee S B, Boo J H (2004) Temperature effect on structural properties of boron oxide thin films deposited by MOCVD method. *Thin Solid Films* 464: 164–169. doi:10.1016/j.tsf.2004.05.107.
- [20] Chengchun Tang, Yoshio Bando, Yang Huang, Shuanglin Yue, Changzhi Gu, FangFang Xu, and Dmitri Golberg; *J. Am. Chem. Soc.*, 2005, 127 (18), pp 6552–6553; DOI: 10.1021/ja042388u.
- [21] C. Guimon, D. Gonbeau, G. Pfister-Guillouzo, O. Dugne, A. Guette, R. Naslain and M. Lahaye; *Surface and Interface Analysis* Volume 16, Issue 1-12, pages 440–445, July 1990; DOI: 10.1002/sia.740160191.
- [22] Song, L.; Ci, L.; Lu, H.; Sorokin, P. B.; Jin, C.; Ni, J.; Kvashnin, A. G.; Kvashinin, D. G.; Lou, J.; Yakobson, B. I.; Ajavan, P. M. *Nano Lett.* 2010, 10, 3209.
- [23] Sainsbury, T.; Ikuno, T.; Okawa, D.; Pacile, D.; Frechet, J. M. J.; Zettl, A. J. *Phys. Chem. C* 2007, 111, 12992.
- [24] Chen, X.; Gao, X. P.; Zhang, H.; Zhou, Z.; Hu, W. K.; Pan, G. L.; Zhu, H. Y.; Yan, T. Y.; Song, D. Y. *J. Phys. Chem. B* 2005, 109, 11525.
- [25] Sajjad M, Zhang H X, Peng X Y, Feng P X (2011) Effect of substrate temperature in the synthesis of BN nanostructures. *Phys. Scr.* 83: 065601-065604. doi:10.1088/0031-8949/83/06/065601.
- [26] Sajjad M, Feng X P (2011) Low temperature synthesis of cubic boron nitride films. *Appl. Phys. Lett.* 99: 253109-1—253109-4. <http://dx.doi.org/10.1063/1.3671170>.
- [27] Pakdel A, Zhi C, Bando Y, Nakayama T, Golberg D (2011) Boron Nitride Nanosheet Coatings with Controllable Water Repellency. *ACS nano* 5: 6507–6515. doi:10.1021/nn201838w.
- [28] Zhu M, Wang J, Outlaw R A, Hou K, Manos D M, Holloway B C (2007) Synthesis of carbon nanosheets and carbon nanotubes by radio frequency plasma enhanced chemical vapor deposition. *Diamond & Related Materials* 16: 196–201.
- [29] Yu J, Qin L, Hao Y, Kuang S, Bai X, Chong Y M, Zhang W, Wang E (2010) Vertically Aligned Boron Nitride Nanosheets: Chemical Vapor Synthesis, Ultraviolet Light Emission, and Superhydrophobicity. *ACS NANO* 4: 414-422. doi: 10.1021/nn901204c.
- [30] Jie Yu, Li Qin, Yufeng Hao, Shengyong Kuang, Xuedong Bai, Yat-Ming Chong, Wenjun Zhang and Enge Wang; *ACS Nano*, 2010, 4 (1), pp 414–422; DOI: 10.1021/nn901204c.
- [31] Jin M S, Kim N O (2010) Photoluminescence of Hexagonal Boron Nitride (h-BN) Film. *Journal of Electrical Engineering & Technology* 5: 637-639. doi: 10.5370/JEET.2010.5.4.637.

## Chapter 4

### Nanoscale Structure Study of BNNSs

In this chapter, we report on nanoscale structures of as synthesized BNNSs based on electron microscopic characterization. The nanosheets were surveyed using scanning electron microscopy (SEM), transmission electron microscopy (TEM) and high resolution TEM (HRTEM) microscopy. SEM images were recorded using a JEOL JSM-7500F, also equipped with a transmission electron detector (TED). TEM data were recorded using a Carl Zeiss LEO 922 EFTEM and a JEOL JEM-2200FS high resolution TEM (HRTEM). Raman spectroscopy and examined using

#### 4.1 Layered Structure Characterization of BNNSs by TEM

For layered structure characterization, we collected part of as synthesized BNNSs samples and analyzed them applying TEM. Electron microscopic images of layered BNNSs are presented in Fig. 4.1 (a-c). SEM image (Fig. 4.1 (a)) indicates large area, highly flat BN nanosheets. The area of an individual BNNS can be estimated easily from SEM image and it is even greater than  $50 \times 50 \mu\text{m}^2$ . Corresponding TEM images of BNNSs are presented in Fig. 4.1(b-d). TEM data shows several multilayer nanosheets (Fig. 4.1 (b)). In order to interpret the structure and number of layers in nanosheets, we selected a piece of an individual nanosheet as shown in Fig. 4.1 (b) and focused electron beam onto its edge. Three layers can be identified as shown in Fig. 4.1 (c). Continuing to magnify the TEM image, the highly ordered layer structure become obvious, where seven layers can be distinguished (Fig. 4.1 (d)). Such morphology clearly shows that each nanosheet is composed of several layers depends on the thickness of

nanosheet. So far, at this stage it was difficult to predict the accurate thickness and actual number of layers in a single nanosheet due to limited resolution of TEM. In order to identify crystalline structure more precisely and to report the correct number of layers, HRTEM measurements were required. Selected area electron diffraction (ED) pattern represents complicated pattern of several diffraction rings coming from various over-layer structures of BNNSs representing the polycrystalline structure of nanosheets (Fig. 4.1 (e)). Meanwhile, with the careful observation, one can distinguish bright dots displaying hexagonal patterns.

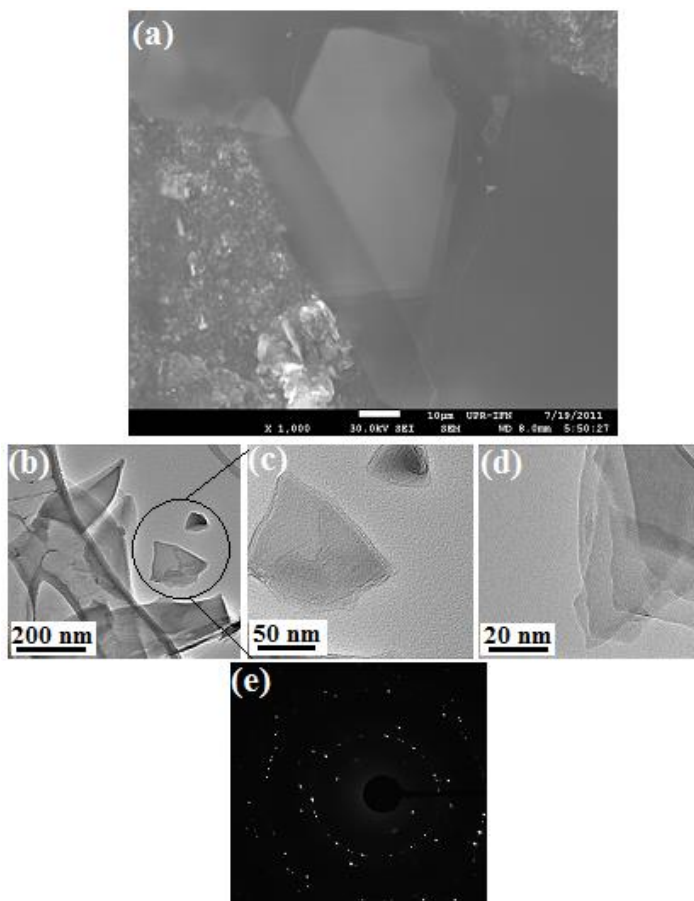


**Figure 4.1** Electron microscopic images of BNNSs, (a) SEM, (b) TEM, (c,d) magnified TEM images of the edge of nanosheet. (e) ED pattern of BNNSs. The scalar bars are shown on the image.

## 4.2 Nanoscale Structure Analysis of BNNSs

In order to further analyze the nanoscale structure within the nanosheets, we selected different samples randomly and recorded HRTEM images as shown in Fig. 4.2 (a-d). A bright field HRTEM image recorded from the center of a thin BNNSs cluster shows honeycomb crystal lattice structure of six membered  $B_3-N_3$  hexagons. The width between each two consecutive B or N atoms is around 0.22 nm as shown in the magnified image in Fig. 4.2 (a). The ratio between the B and N atoms is nearly unit. No carbon and other impurities were detected. We observed the wrinkle in nanosheets possibly caused by perturbation induced by scratching of the BNNSs from the sample to a template for HRTEM measurement. Figure 4.2 (b) shows a HRTEM image of several BNNSs with different orientations. From this image, we selected two different areas as marked with white and black box in the image and magnified them to understand the variation of the nanoscale structure from center (marked with K1) to the edge of nanosheet (marked with K2) as shown in Fig. 4.2 (c) and Fig. 4.2 (d), respectively. Considering the area K1 (in Fig. 4.2 (c)), one can see that the distance between two bright lines is around 0.22 nm as observed in Fig. 2a. It is theoretically well known and experimentally verified that 0.22 nm corresponds to the distance between two consecutive B or N atoms within the surface of a BN nanosheet. On the other hand the area K2 shows that the distance between two bright lines is around 0.35 nm and indicating the distance between two consecutive layers on the edge of a nanosheet. Similar observation was made analyzing the area shown in Fig. 4.2 (d) where the width between two bright lines is 0.22 nm and is the same for entire selected area (*i.e.* it indicates the surface of underneath BN nanosheet). The HRTEM image obtained from the edge of nanosheet relates to atomic multilayer structures, whereas the center area of nanosheet is composed of B and N atoms arranged in periodic honeycomb crystal lattice structures. Moreover, groups of the bright lines

selected from two different nanosheets (marked as K1 area in Fig. 4.2 (c) and Fig. 4.2 (d)) are perfectly matched with each other. This provides an evidence of very high nanoscale crystalline structure of each BN nanosheet regardless of their orientation.

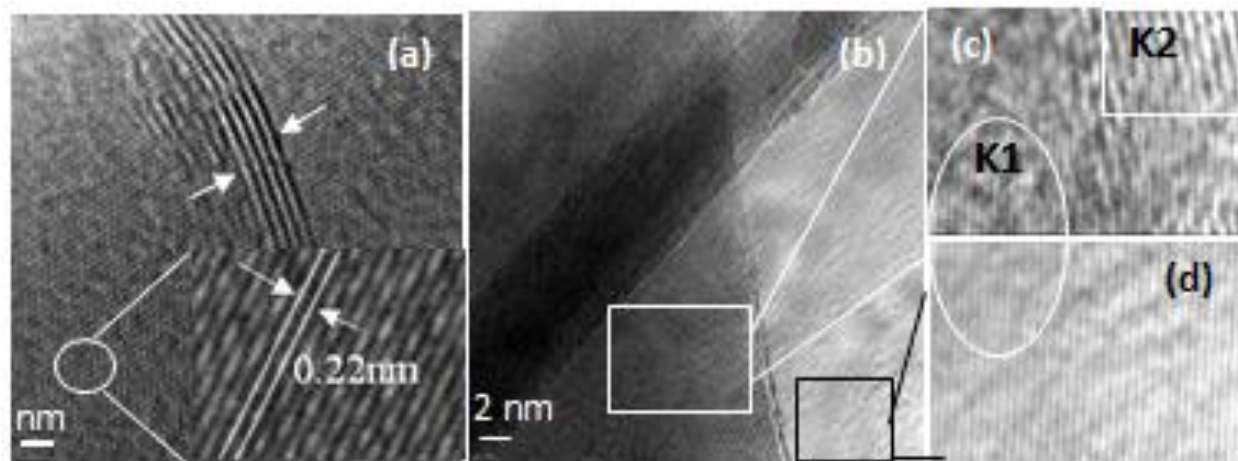


**Figure 4.2** (a-d) HRTEM images of nanoscale structured BNNSs.

#### 4.2.1 Monolayer BNNS

In our current development in the synthesis process, we successfully isolated single layer BNNS from as synthesized BNNSs samples. An example is shown below in Fig. 4.3. In order to analyze crystalline structure of BNNSs precisely, a single ultrathin boron nitride sheet is collected from the sample for further structural characterizations. HRTEM microscope equipped with an imaging aberration corrector, operated at 200 kV to directly characterize the crystalline structures of the single sheet as shown in Fig. 4.3a. The image shows densely packed honeycomb crystal lattice structure of six-membered  $B_3-N_3$  hexagon probably belongs to a single or few atomic layer BNNSs [1-3]. In further magnifying image (Fig. 4.3b),  $B_3-N_3$  rings or two-dimensional benzene-like structures can be identified clearly. No other atomic layers or atoms are visible below  $B_3-N_3$  rings indicating single layer BNNS. The shortest distance between the N and B atoms is estimated around 0.145 nm along the (100) lattice direction that is consistent with

the reported value for h-BN layer [4,5]. Within each layer of h-BN, B and N atoms are bound strongly by covalent bonds, whereas the atomic layers are held together by weak van der Waals forces

No defects from the BNNSs are detected (Fig. 4.3 (b)), though we operated the microscope at 200 keV, from which we could conclude that short pulse laser technique can be used to synthesize high quality, defects free BNNSs. It should be mentioned here that previously reported data shows that the high-energy ( $\geq 80$  keV) electron beam operated in TEM would damage atomic-layer of BNNSs [6-9]. The knock-on damage threshold for B atoms and N atoms in BN nanotubes are reported only 74 keV and 84 keV, respectively [10]. However, in the present work, the sheet was imaged for a very short time with reduced illumination that efficiently avoids any possibility of the knock-on damage of boron and nitrogen atoms within BN sheets. To date there is no report on the solution of the damage problem during atomic-thin film characterization with HRTEM with electron beam energy above 150 keV.

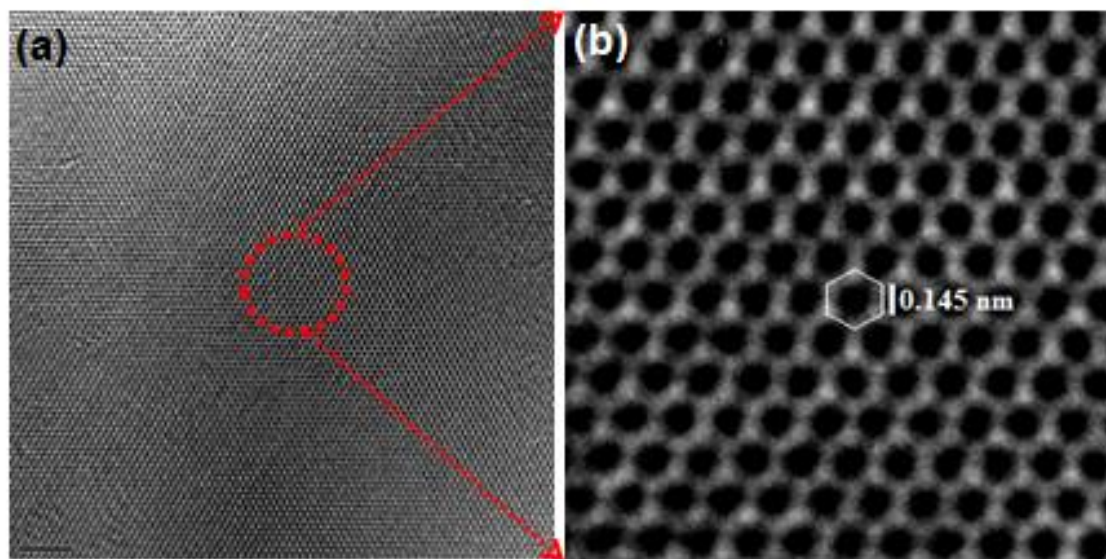


**Figure 4.3** (a) Experimentally obtained single layer BNNS, (b) magnified HRTEM image.

#### 4.2.2 SAED and FFT Pattern of Monolayer BNNS

SAED and Fast Fourier Transform (FFT) pattern of the corresponding sample (Fig. 4.3), also indexed to h-BN structure (Fig. 4.4). The pattern of same sample was indexed to *h*-BN with the zone axis along the  $[-1\ 1\ -1]$  direction (Fig. 4.4 (a,b)). Bright spots arranged in a typical hexagonal honeycomb structure of six membered  $B_3-N_3$  hexagons were easily identifiable. A series of diffraction spots arranged in typical hexagonal pattern indicated a single crystalline structure of synthesized BNNSs [11,12]. This is in good agreement with the data obtained from HRTEM and Raman spectral measurements of BNNSs samples.

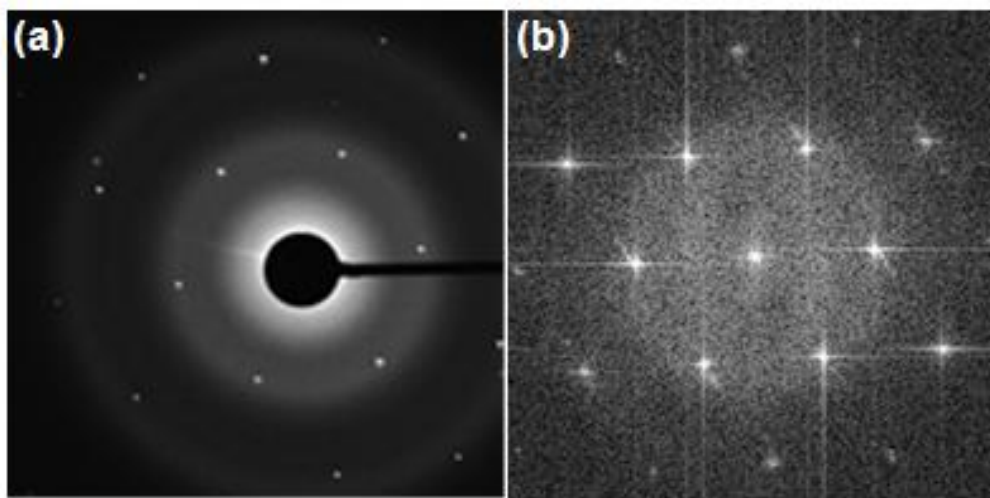


**Figure 4.4** (a) SAED and (b) FFT pattern of BNNSs; clearly identifying hexagonal structure.

#### 4.2.3 Nanoscale Structure of Single BNNS

In order to carry on further investigations on nanoscale structures of BNNSs, we collected different sample and HRTEM measurements were conducted. This time, we selected different areas of BNNS to analyze more precisely the variation of crystalline structure at nanoscale level. Slight aberrations at different locations of HRTEM image of BNNSs have been



identified. Fig. 4.5 (a) shows HRTEM image of BNNS of the area  $40 \times 40 \text{ nm}^2$ . Since slight aberrations, HRTEM images of other areas appear slightly different structures such as, honey comb crystal lattice structure (Fig. 4.5 (b)) rectangular block arrays (Fig. 4.5 (c)) or bright dot arrays (Fig. 4.5 (d)). In the area marked with “K”, ones even can see fringe type of structures that are comparable to the image shown in Fig. 4.2 (a). Therefore, the observed nanosheet is related to multi-structures.

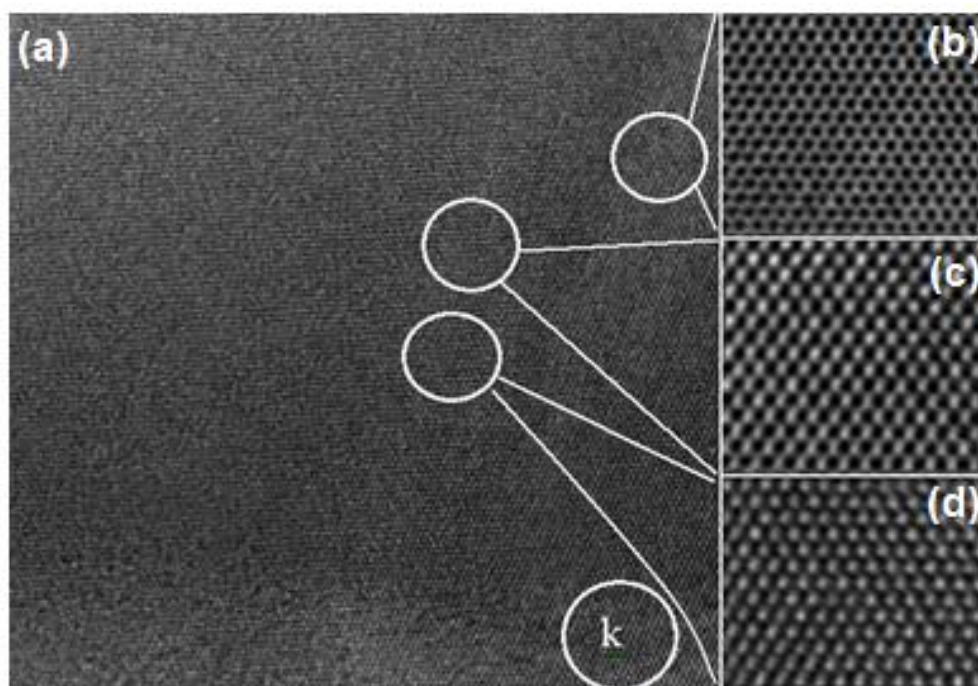


**Figure 4.5 (a-d)** HRTEM images of BNNSs with slight aberrations at different locations.

#### 4.2.4 Thickness of Single BNNS

Thickness of the nanosheets plays a critical role in practical devices technology. It is difficult to analyze accurate thickness of entire synthesized BNNSs sample because of the random orientation of nanosheets. However, thickness of an individual nanosheet can be identified by carefully imaging of the film edge and counting the number of layers. We collected two different BNNSs samples and results are shown in Fig. 4.6(a,b) where multilayers were

examined. The image shows a single BNNS consists of four to five stacked layers with 1.5 nm in thickness. Figure 4.6 also shows few nanometer thick BNNS.

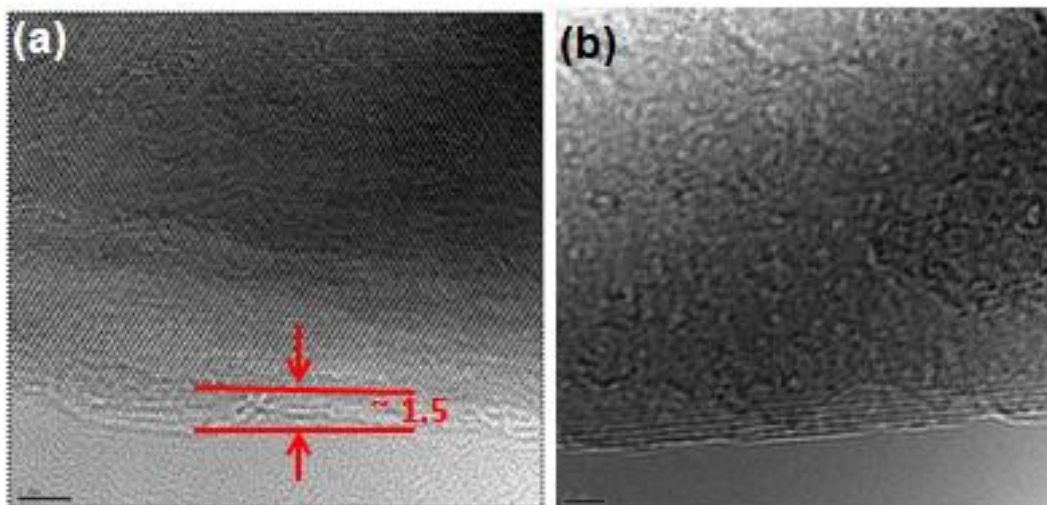


**Figure 4.6** (a,b) HRTEM images of the edge of BNNSs indicating few layer thickness.

#### 4.2.5 Thickness of Multilayer BNNSs

In the previous section (Fig. 4.6) we estimated thickness of an individual BNNS. In this section we will continue our effort to estimate thickness of multilayer BNNSs. It is difficult to analyze accurate thickness of synthesized BNNSs film because of the random orientation of nanosheets. However, thickness of an individual nanosheet can be identified by carefully imaging of the film edge and counting the number of layers as presented in previous section (Fig. 4.6). Figure 4.7 (a) shows TEM of a single nanosheet while Fig. 4.7 (b,c) shows two or more nanosheets simultaneously. TEM images show that most of the as-grown BN nanosheets are more than one atomic layer thick. This is confirmed by focusing TEM microscope on the edge of a nanosheet. We believe that a single BN nanosheet consists of approximately 30 layers which correspond to the total thickness of 10 nm (Fig. 3 (d)). The individual BN layers within the nanosheets assembly are perfectly overlapped as indicated by observed the spherical dots on the

edge of nanosheets. This, in our judgment, confirms that synthesized BNNSs are highly-ordered structures with good crystalline orientation. Figure 4.7e shows a single nanosheet consisting of 10 layers and overall thickness of 3.3 nm. Figure 4.7 (f) shows several nanosheets having different orientation directions and composed of different number of BN layers.

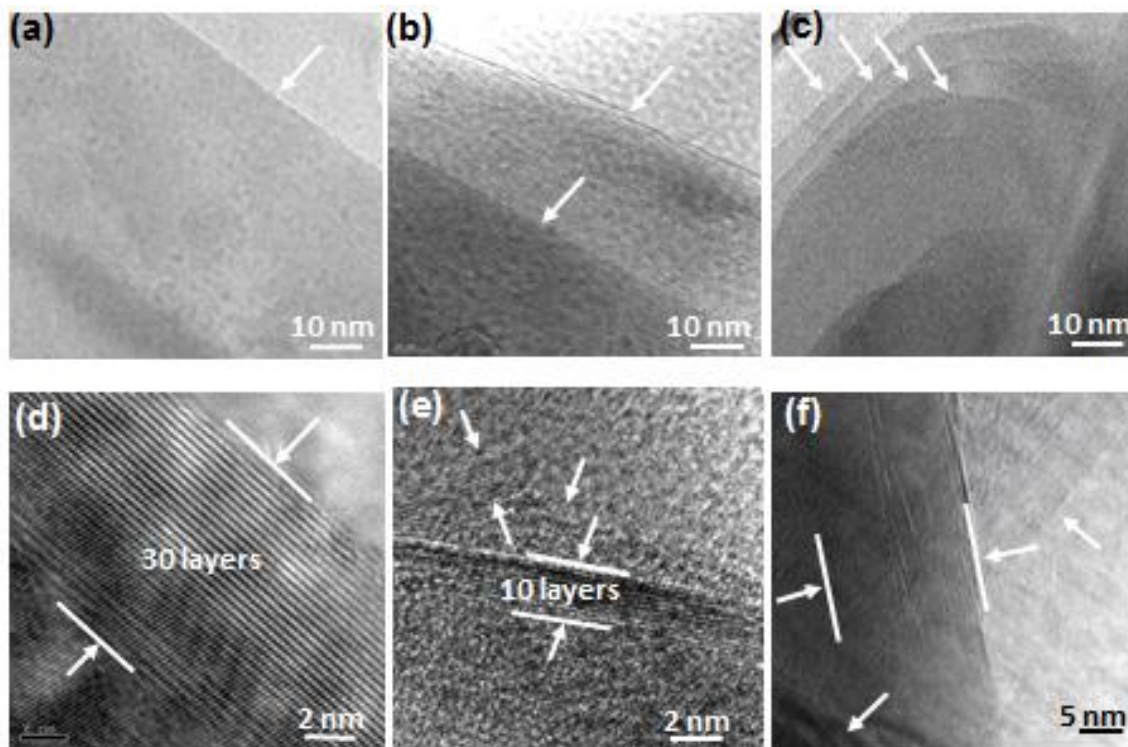


**Figure 4.7** Morphology of atomic BNNSs. (a-c) TEM images of the surface of a single-, double-, and multi- BN sheets. (d-f) HRTEM images of the edge of the nanosheets. Scale bars are shown on the images.

#### 4.2.6 Wrinkles in BNNSs

Fringe structures were also observed from the surface of BNNSs but obviously it was rather related to the sheet wrinkle than to the stacked atomic layers. Generally wrinkles forms due to 2D nature of the sheets [13-15]. In order to identify and understand their differences, TEM images of surface of a single BNNS with different magnifications are presented in Fig. 4.8 (a-d). Because the BNNSs were simply scratched off from the sample and then transferred to the

grids for TEM studies of the nanoscale morphology, such procedure possibly leads to a wrinkle of the sheet as shown in Fig. 4.8 (a). With large magnifications, one can find that the wrinkle actually consists of a large amount of tiny fringes (Fig. 4.8 (b-d)).

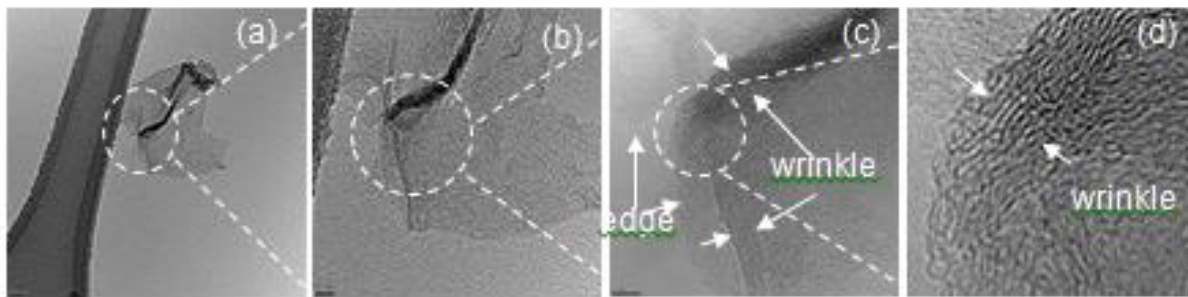


**Figure 4.8 (a-d)** HRTEM images of BNNSs with different magnifications.

Generally understanding is that these fringe structures due to the wrinkle should be random but in fact, it still appeared partially ordered fringe pattern as shown in Fig. 4.8 (b-d), the space/width between the two fringes remains nearly constant, around 0.37 nm that is slightly larger than that the thickness of the single atomic layer.

#### 4.2.7 Knock on Damage in BNNSs

It should be mentioned that because the obtained atomic layer BNNSs are composed of few atomic layer thin, they are easily damaged by high-energy electron beam during TEM measurements. During the TEM measurement, high current density beam (ca.  $1 \times 10^8 \text{ e}/(\text{s} \cdot \text{nm}^2)$ ) was shined on the sample, as result sputtering of BNNSs was observed. Holes “grew” predominantly within a given layer, while the adjacent next layer remains stable for a sufficient amount of time. Using this method, one can reduce few layers nanosheets down to single layer. However, in the present case, our priority was to avoid any damage in nanosheets through high energy electron beam.

Fig. 4.9 (a,b) show the dynamics where the beam damage has just started to form small holes, locally reducing the thickness. After some more irradiation, some “holes” can be found within the irradiated regions (Fig. 4.9 (c,d)). Since the product of such “holes” was observed in real time, the process could easily be stopped by switching off the electron beam after formation of the first hole or potentially at the first vacancy through the entire sheet. Figure 4.8 (b) shows the edge of the atomic BNNSs. The vacancy defect “holes” appeared at the edge area caused by TEM beam sputtering.

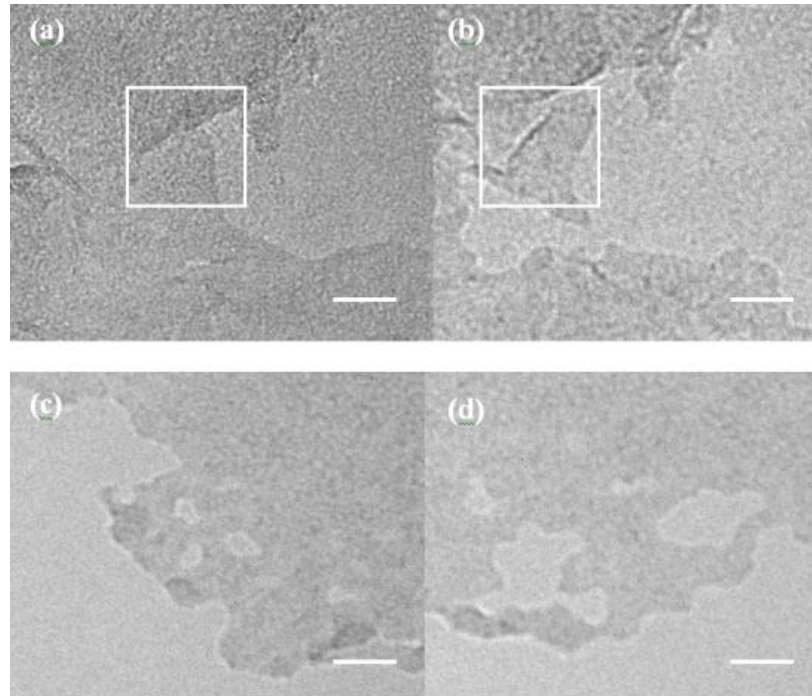


**Figure 4.9** Morphology change in atomic BNNSs during TEM measurement (a) before and (b) after beam. Time between the images is 8 s. Also visible in the sequence is the generation of vacancies within the single-layer BNNS membrane. (c-d) Topological defects are incorporated during this edge reconstruction. On the other edge of the same hole, atoms are removed by the electron beam. Scale bars shown on the images are 1 nm.

In the present case, though we operated the TEM at 200 kV, we mitigated the appearance of defects due to knock-on damage by examining the materials as quickly as possible with



reduced illumination. The knock-on damage threshold of B and N atoms in BN sheets is slightly lower than that of carbon atoms in graphene sheets. The threshold for B atoms and N atoms in BN nanotubes were calculated to be 74 kV and 84 kV, respectively [5]. Scanning TEM images recorded using the TED at 30 kV in the SEM provide ample contrast for examining the samples while avoiding the introduction of potential defects. An example is provided with two images shown in Fig. 4.10 (a,b).

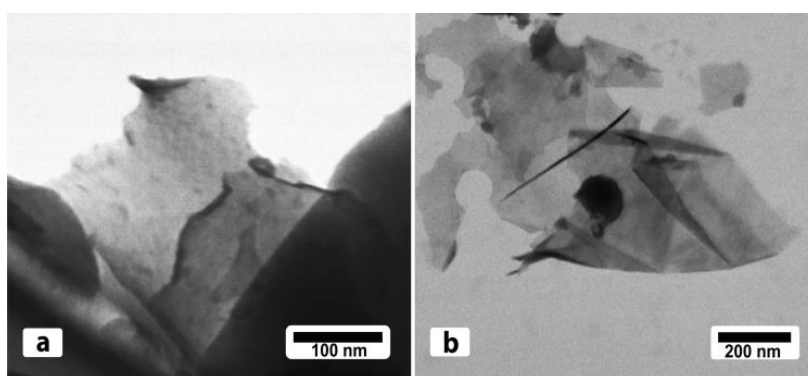


**Figure 4.10** Scanning TEM images recorded from BNNSs at 30 kV using TED (in the SEM) for the samples (a)  $S_1$  and (b)  $S_4$ , respectively.

#### 4.4 Conclusions

In summary, mono layer and few atomic layer BNNSs were synthesized and their nanoscale structures were studied using electron microscope at high resolution. Nanoscale BNNSs structures showed that each sheet is composed of several layers, perfectly packed with honeycomb network of B and N atoms similar to C-C atoms in graphene. From monolayer BNNSs, B and N atoms were identified at eye resolution. The distance (0.145 nm) between two consecutive B and N atoms was estimated by Image J method. This distance is almost equal to C-C atoms in graphene (0.142 nm). At this point we observed that BNNSs were rightly called white graphene.

## 4.5 References

- [1] D. Pacilé, J. C. Meyer, Ç. Ö. Girit, and A. Zettl, *Appl. Phys. Lett.* 92, 133107 2008.
- [2] N. Alem, R. Erni, C. Kisielowski, M. D. Rossell, W. Gannett, and A. Zettl, *Phys. Rev. B* 80, 155425, 2009.
- [3] Zobelli A, Gloter A, Ewels C P, Seifert G, Colliex C (2007) Electron knock-on cross section of carbon and boron nitride nanotubes. *Phys. Rev. B* 75: 245402-1. doi: 10.1103/PhysRevB.75.245402.
- [4] Zhi, Y. C.; Bando, Y.; Tang, C. C.; Kuwahara, H.; Golberg, D. *Adv. Mater.* 2009, 21, 2889.
- [5] Pakdel, A.; Zhi, C.; Bando, Y.; Nakayama, T.; Golberg, D. *ACS NANO* 2011, 5, 6507.
- [6] Meyer, J. C.; Chuvilin, A.; Siller, G. A.; Biskupek, J.; Kaiser, U. *Nano Lett.* 2009, 9, 2683.
- [7] Zobelli, A.; Gloter, A.; Ewels, C. P.; Seifert, G.; Colliex, C. *Phys. Rev. B* 2007, 75, 245402.
- [8] A. V. Krasheninnikov and F. Banhart, *Nature Mater.* 6, 723, 2007.
- [9] A. V. Krasheninnikov and K. Nordlund, *J. Appl. Phys.* 107, 071301 2010.
- [10] J. Kotakoski, C. H. Jin, O. Lehtinen, K. Suenaga, and A. V. Krasheninnikov; *PHYSICAL REVIEW B* 82, 113404, 2010.
- [11] Li Song, Lijie Ci, Hao Lu, Pavel B. Sorokin, Chuanhong Jin, Jie Ni, Alexander G. Kvashnin, Dmitry G. Kvashnin, Jun Lou, Boris I. Yakobson and Pulickel M. Ajayan; *Nano Lett.*, 2010, 10 (8), pp 3209–3215.
- [12] Yi Lin, Tiffany V. Williams and John W. Connell; *J. Phys. Chem. Lett.*, 2010, 1 (1), pp 277–283.
- [13] Weihua Liu, Tao Dang, Zhihao Xiao, Xin Li, Changchun Zhu, Xiaoli Wang; Volume 49, Issue 3, March 2011, Pages 884–889.
- [14] Novoselov KS, Geim AK, Morozov SV, Jiang D, Katsnelson MI, Grigorieva IV, et al. Two-dimensional gas of massless Dirac fermions in graphene. *Nature* 2005;438: 197–200.
- [15] Son YW, Marvin LC, Steven GL. Half-metallic graphene nanoribbons. *Nature* 2006; 444: 34, 7–9.

## Chapter 5

### Applications of BNNSs

New applications using 2D sheets obtained from bulk layered materials are very promising for nano-electronic devices as evidenced from graphene. BNNSs are one example of those 2D nanomaterials that have been used to fabricate nanoelectronic devices. This chapter highlights our approach from synthesis to device applications of BNNSs in three different areas e.g. Schottky diode, DUV photo-detector, and resistance based gas sensor.

#### 5.1 Electronic Applications

In current research, BNNSs have been used for the development of prototype Schottky diode. One of main challenges in the fabrication of diode device was possible gaps which exist between two consecutive sheets shown in Fig. 5.1 (a). From electron microscopic measurements, we observed that the size of a single continuous piece of BNNS is not enough to locate electronic connections on it in order to record measurements.

This would unavoidably result in serious contact or short cut problems between the over layer metal at the top of BNNSs and the metal layer at the bottom for BNNSs/metal based device. In our research, we overcome this challenge to slightly increase thickness of deposited sample where a certain number of BNNSs heavily overlapped one another (as shown in Fig. 5.1b) and possibly avoided gaps or contact problems. Therefore, around 200 nm thick sample consists of many overlapped BNNSs that covers entire substrate surface and it was easy to fabricate electronic connections on top of BNNSs/metal substrate.



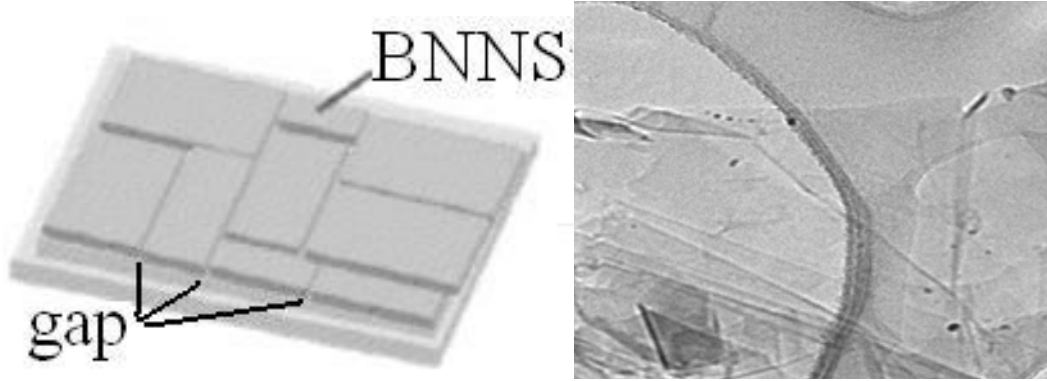


**Figure 5.1** (a) Schematic illustration of BNNSs segment with a large amount of gaps over substrate, (b) heavily overlapped BNNSs.

### 5.1.1 Development of BNNSs-Based Prototype Schottky Diode

Much attention paid in the fabrication of BNNSs-based Schottky diode. Two types of junction: pure BNNSs/metal and doped-BNNSs/metal, have been fabricated and tested. The fabricated device is shown in block diagram (Fig. 5.2). As, the entire surface of substrate was covered with randomly oriented BNNSs, we setup electrodes on the surface of BNNSs/Mo substrate by electronic soldering method. For the precise measurements of current versus voltage (I-V) characteristics, set-up is connected with a Keithley 6517A electrometer in order to characterize electronic properties of BNNSs.

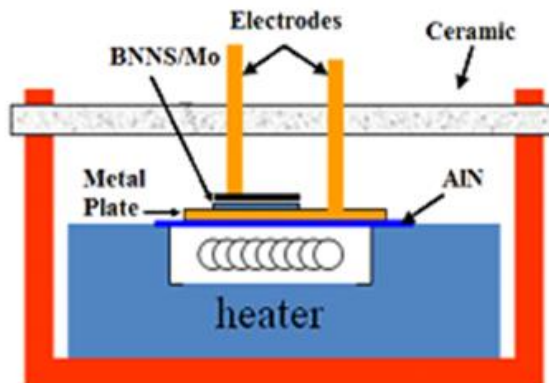


**Figure 5.2** Block diagram of the device prepared to analyze the characteristics of BNNSs-based Schottky diode.

### 5.1.2 I-V Characteristics of Carbon Doped BNNSs-Based Schottky Diode

So far, doping is a most feasible method to reconstruct the energy band-gap and produce the Schottky contact between the BNNSs and the metal surface. The doping process is completed by exposing nanosheets via cold plasma [1,2]. A low-pressure (10 Pa) CH<sub>4</sub> was used with dc plasma ignited between two electrodes. The samples were kept 5 cm away from the discharge zone to minimize any possible damage by energetic ions. The doped BNNSs were placed back to the device in order to analyze I-V characteristics of Schottky diode. The dopant atoms incorporate into the BNNSs that could possibly lead to the formation of different B<sub>x</sub>-C<sub>y</sub>-N<sub>z</sub> layered structure and improve the electronic and semiconducting properties of the material [3]. Theoretical and experimental investigations indicated that B<sub>x</sub>-C<sub>y</sub>-N<sub>z</sub> mixed phases are typical p-type semiconductors [4]. Moreover, the size of the active region between the BNNSs and the metal substrate is probably in the order of few nanometers. At such small size, addition of a single atom can drastically change the device behavior. I-V characteristics of BNNSs/metal junction recorded at room temperature are shown in Fig. 5.3. These characteristics are identical to that of typical PN junction diode characteristics.

The curve shown in Fig. 5.3 appear typical diodic behaviors: its tendency to conduct electric current in only one direction. Normally, the curve can be divided into four areas. At very large reverse bias, beyond the breakdown voltage (-73V), a process called reverse breakdown occurs that causes a large increase in current that usually damages the diode permanently. Here it should be mentioned that because the thickness of membrane of the BNNSs is less than 10 nm, experimental data indicate that the breakdown of electric field value is up to  $7.3 \times 10^7$  V/cm.

These characteristics are directly attributing the outstanding properties of BNNSs as a material for electronic applications. The second region, at reverse biases has only a very small reverse saturation current. In the reverse bias region for a normal P–N junction diode, the current through the device is very low (in few  $\mu\text{A}$  ranges). The third region is forward with forward bias voltage less than 45V, where only a small forward current is conducted. As the potential difference is increased up to or above  $V_d = 45\text{V}$  (forward voltage drop), the diode current becomes appreciable, and the diode presents a very low resistance.

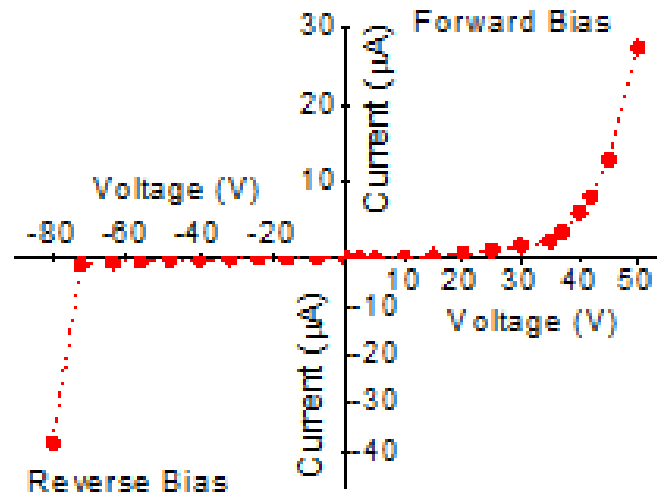


**Figure 5.3** I-V characteristics of BNNSs-based Schottky diode at room temperature.

### 5.1.3 Effect of Temperature in the I-V Characteristics of Schottky Diode

Current versus voltage (I-V) characteristics for the case of pure BNNSs/metal junction at different temperatures (25 °C, 50 °C, and 75 °C) are recorded as shown in Fig. 5.4a. Generally, high temperature would cause a decrease in the resistance of BNNSs, resulting in an increase of electric current at the certain voltage. At a fixed temperature, current increased almost linearly with the applied voltage (Fig. 5.4a). This indicates that the active region between the pure BNNSs and metal substrate has no Schottky contact. In order to produce Schottky contact

between the BNNSs and metal substrate, we doped BNNSs with carbon atoms. I-V characteristics of Schottky diode based on doped BNNSs at 25 °C and 75 °C are presented in Fig. 5b. It seems that variation of temperature does not obviously affect forward current by much. However at sufficiently high temperatures, a substantial amount of current can be observed.

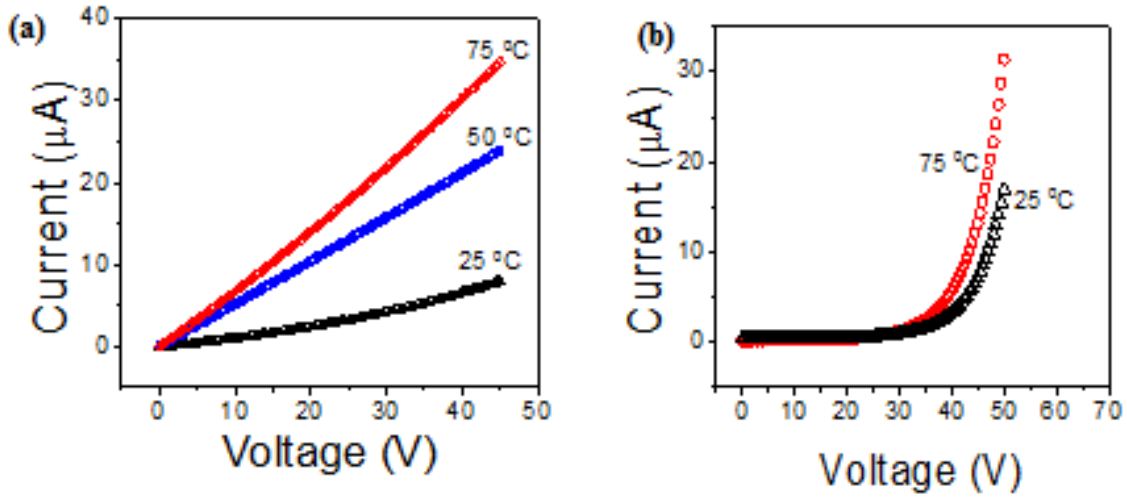


**Figure 5.4** Effect of temperature on I-V characteristics of Schottky diode based on (a) un-doped BNNSs, (b) doped BNNSs.

## 5.2 Hydrogen Plasma Modification in BNNSs

We also studied energy bandgap modification of rippled BNNSs by hydrogen plasma modification. Dramatic changes have been observed in transport properties in BNNSs, as evidenced by electrical measurements [5]. Considering BNNSs a wide bandgap material, a special measurement setup was made to ensure the electrical signal in the detectable range, which is shown in Fig. 5.5 (a). A mesh type copper pad, which serves as electrode, was used to contact to the BNNSs for the purpose of facilitating plasma treatment. The effective resistance between the two electrodes is only from BNNSs, which means the electron will vertically go through nanosheets when the voltage is applied between electrodes. It should be mentioned that the electrical signal from the in-plane BNNSs is out of our detectable range.

Typical changes induced by the hydrogen plasma treatment in electronic properties of nanosheets are illustrated in Fig. 5.5. Before plasma exposure, the contact resistance of nanosheets was about 1.8 M ohm. As a reference, nanosheets were exposed to pure Ar plasma. The nanosheets only showed very little change in their resistance. This behavior significantly changed after sheets were treated with atomic hydrogen plasma, which exhibits a strong time dependence of its resistivity during hydrogen plasma treatment. The resistance of nanosheets decreased by 38%, as shown in Fig. 5.5 (a). It typically required 250 s of plasma treatment to reach the saturation in measured characteristics, showing that nanosheets were processed with hydrogen plasma step by step.

Fig. 5.5 (b) show the logarithm of the electric conductivity versus the reciprocal temperature at hydrogen plasma treatment 0, 60, 120, 180, and 250 s, respectively. Namely, the cumulative electrical conduction ( $\sigma$ ) of a semiconducting substance is determined by the following equation [6]:

$$\sigma = \sigma_0 T^{3/2} \exp(-E_g/2kT) + \sigma' \exp(-\Delta E/kT) \quad (1)$$

where  $\Delta E$  is the ionization energy of the impurity level,  $k$  the Boltzmann's constant, while  $\sigma$  and  $\sigma'$  are constants. The two terms in the eq 1 correspond to the intrinsic and extrinsic conduction mechanism, respectively. The impurity and or the defect content affects the concentration of carriers, which is determined by the intrinsic properties of the pure semiconductor crystal [7]. In the intrinsic region, the temperature dependence of the conductivity is dominated by an exponential factor;

$$\sigma \propto \exp(-E_g/2k_B T) \quad (2)$$

Therefore, the plot of  $\log \sigma$  versus  $1/T$  gives a straight line in the intrinsic region, and the magnitude of the slope gives the energy gap [8]. The inset in Fig. 5.5 (b) shows the band-gaps of

h-BN membranes processed at 0, 60, 120, 180, and 250 s, respectively. Following the time, the band-gaps of h-BN membranes decreased from  $\sim 5.6$  eV at 0 s to 4.25 eV at 250 s, which is a signature of transition from insulating to semiconductive regime.

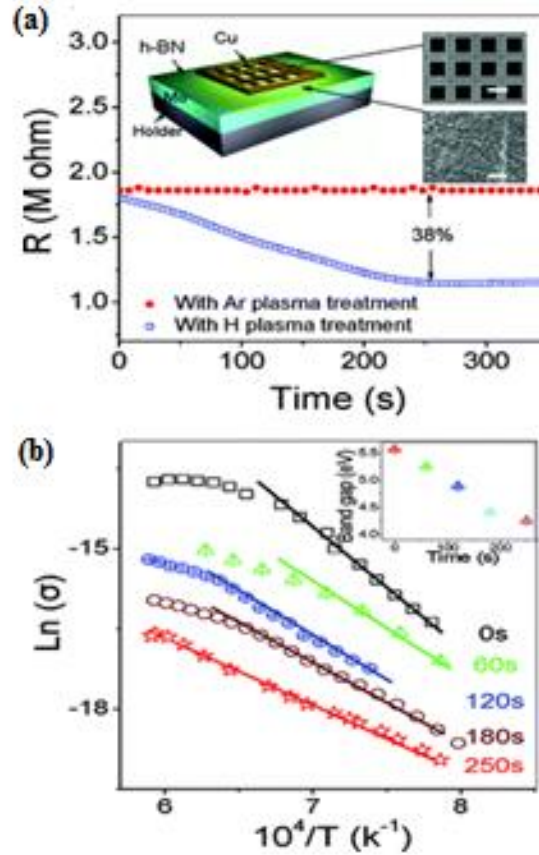


**Figure 5.5** (a) In situ measurement of resistance of the BNNSs with hydrogen plasma treatment as a function of time. Inset: illustration of the setup for measuring the electronic properties of BNNSs. (b) Logarithm of the electric conductivity of BNNSs plotted against the reciprocal temperature during hydrogen plasma treatment. The scale bars in the inset of a are 5  $\mu\text{m}$ .

### 5.2.1 I-V Characteristics of Surface Modified BNNSs

Figure 5.6 shows the I-V characteristics of the hydrogen plasma-treated BNNSs as a function of applied voltage. They have exhibited nonlinear behavior at room temperature after plasma treatment. The nonlinearity of the I-V curves in this system is probably due to the dipole formation at the interface, perturbation of the nanosheets beneath the metal, reaction of the metal

or BNNSs with unwanted impurities at the interface [9-12]. The level of nonlinearity varies with temperature, and the curves become practically linear at 200 °C, which is probably caused by the desorption of hydrogen atoms at higher temperature, leading to recover of nanosheets. The inset shows the I–V characteristics of untreated nanosheets, all of which have linear behaviors and little change can be observed with increasing temperature.

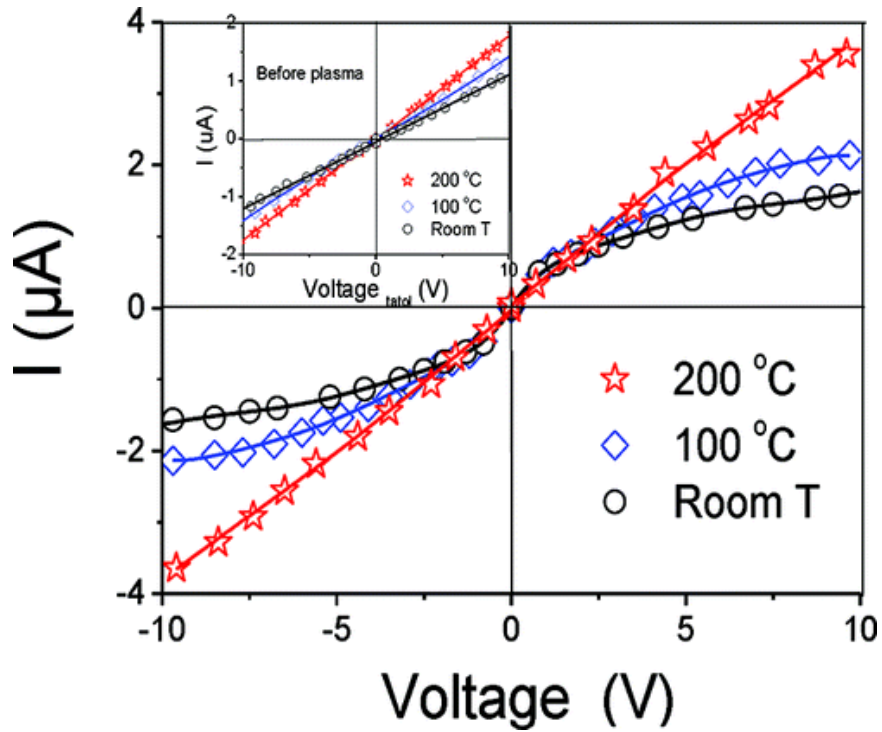


**Figure 5.6** I–V characteristics of a hydrogen plasma-treated h-BN membranes measured at room temperature, 100 °C and 200 °C, respectively. Inset: Temperature dependence of the I–V characteristics before plasma. From bottom to top: T = 200 °C, 100 °C, and room temperature.

### 5.2.2 Sideways and Top Down Measurements of I-V Characteristics

Electrical characterizations of BNNSs were also conducted in two different orientations of BNNSs e.g. side-ways and from top-down. These I-V properties of BNNSs based on measurements through a HP - Agilent 6268B Power Supply, a Keithley 6517A electrical meter,

and a HEWLETT 34401A electrical meter controlled by Labview program. Each data point in the I-V curves is the average of 8 measurements in order to reduce error in measurements. Current-voltage curves of BNNSs are shown in Fig. 5.7. Using a wire mode for resistance  $R=\rho l/A$  where the  $l$  is the wire length, and the  $A$  is its cross-sectional area, we can calculate the resistivity  $\rho$  (the constant of proportionality) of BNNSs. Experimental data measured from transversal direction (top-down) as shown in Fig. 5.7 (a) indicates that the obtained resistance is  $5.6 \times 10^{10} \Omega$  (one thousand electrical voltages yield  $0.18 \times 10^{-7}$  amp current) for  $2 \mu\text{m}$  thickness of BNNSs. Because the distance between the two electrodes is  $0.5 \text{ mm}$ , the cross-sectional area of the BN membrane is  $2 \mu\text{m} \times 5 \text{ mm}$ , the resistivity is then estimated around  $\rho=1.1 \times 10^6 \Omega\text{m}$ . In contrast for  $30 \text{ nm}$  thick BNNSs, we have the resistance of  $1.2 \times 10^{13} \Omega$  (one thousand electrical voltages yield  $0.0825 \times 10^{-9}$  amp current) where the area of the cross section is  $30 \text{ nm} \times 5 \text{ mm}$ , from which the resistivity is estimated around  $\rho=3.6 \times 10^6 \Omega\text{m}$ . Both data are in good agreement with each other. Similar resistivity value can also be obtained from the data of  $600 \text{ nm}$  of BNNSs.

The experimental data measured in longitudinal direction as shown in Fig. 5.7b, the obtained resistance is  $5 \times 10^6 \Omega$  (four electrical voltages yield  $0.72 \times 10^{-6}$  amp electrical current) for  $7 \mu\text{m}$  thick BNNSs. Since the area of cross section of the membrane is around  $5 \times 5 \text{ mm}^2$ , the resistivity is obtained around.  $\rho=8.4 \times 10^6 \Omega\text{m}$ . Based on these resistivity data above, one may expect that  $30 \text{ nm}$  thin BNNSs should have the resistance value around  $1.7 \times 10^4 \Omega$  but the actual resistance of the  $30 \text{ nm}$  thin BNNSs is only  $1.1 \text{ Ohm}$  (one electrical voltage yields  $0.9 \text{ amp}$  electrical current as seen in Fig. 5.7 (b)). Because the cross-sectional area is still  $5 \times 5 \text{ mm}^2$ , the resistivity is then obtained around  $\rho=4.2 \times 10^2 \Omega\text{m}$ . It is believed that spatially non-uniform the membrane would not possibly cause such big difference above. Large differences of the



resistivity / conductivity coefficients probably indicated that the BNNSs with different thickness would have very different scattering mechanisms or there is a special electrical channel such as quantum tunneling existed in the super thin BNNSs that affect their conductivity coefficients.

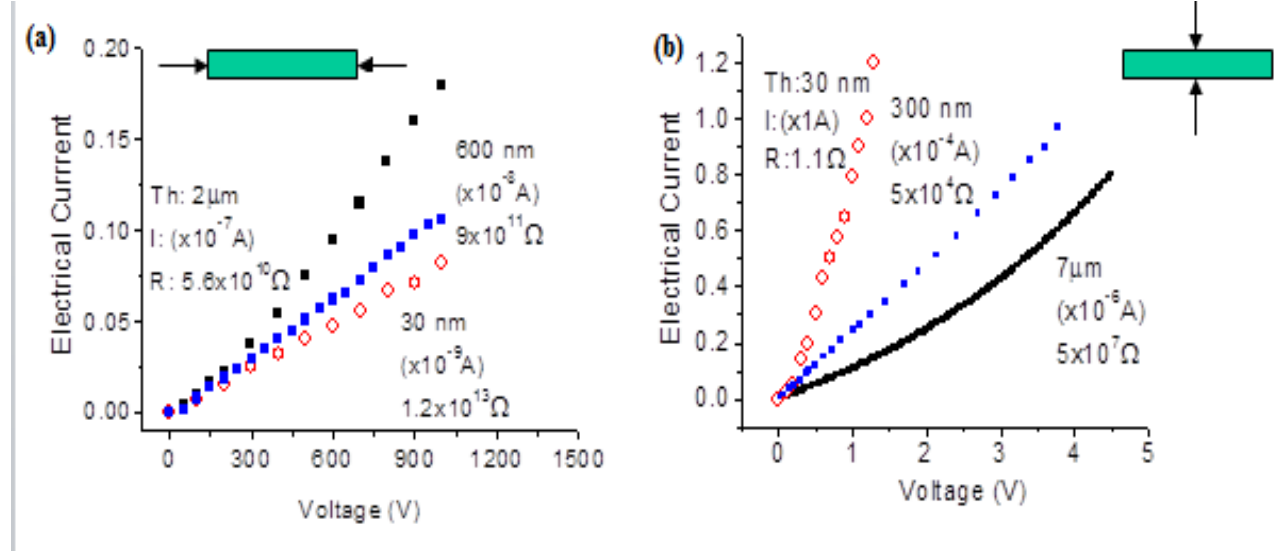
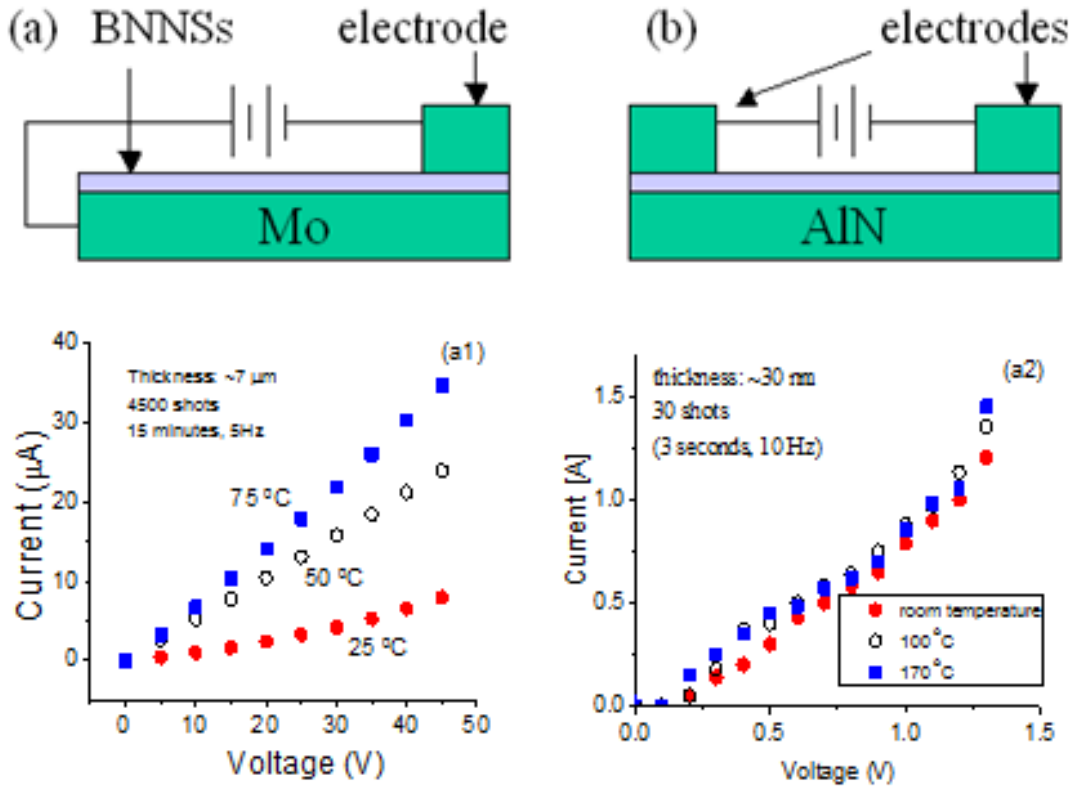


**Figure 5.7** Typical I-V properties of different thickness of BNNSs characterized from (a) longitudinal and (b) transversal directions. Th: thickness, I: electrical current; and R: resistance of the samples.

### 5.2.3 I-V Measurements of BNNSs/ Mo and BNNSs/AlN

I-V characteristics of BNNSs/Mo and BNNSs/AlN were also recorded based on a HP - Agilent 6268B Power Supply, a Keithley 6517A electrical meter, and a HEWLETT 34401A electrical meter controlled by Labview program. This time the experimental set up used is shown in Fig. 5.8 (a) and (b) where two types of substrates: metal molybdenum (Mo) and ceramic AlN wafer were used, respectively. Each data point in the I-V curves is the average of 8 measurements taken 1 second apart in order to reduce error in measurements. Current-voltage curves of 7 μm and 30 nm thick BNNSs respectively, on Mo substrate are shown in Fig. 5.8a1 and Fig. 5.8a2. Different thickness of the samples would result in different I-V characteristics.

Experimental data (a1 and a2) obtained from setup (Fig. 5.8a) indicates that 233 times of the decrease of BNNSs membrane in the thickness (from 7  $\mu\text{m}$  to 30 nm) result in  $\sim 105$  times of the increase of electrical current. Spatially non-uniform the membrane would make some contribution to the phenomenon above but it is not expected that would cause  $\sim 105$  of difference. Tentative interpretation is that the increases of the current is due to quantum tunneling effect that usually occurs in the case of super think films [13,14]. There is no obvious change on the I-V curves recorded due to temperature effect in the case of 30 nm BNNSs as shown in Fig. 5.8a2.



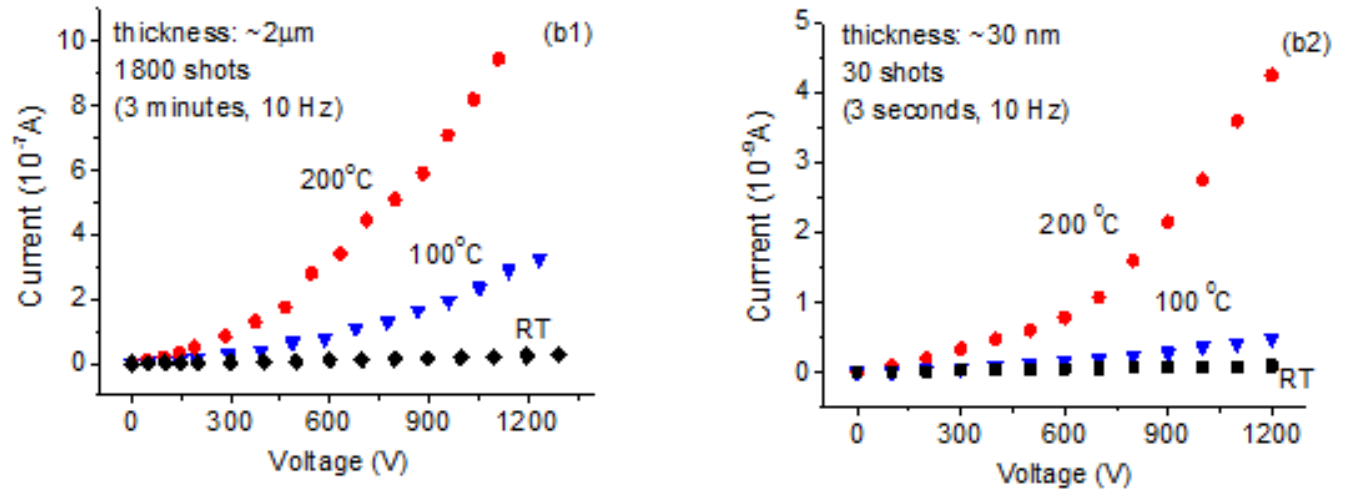


**Figure 5.8** Experimental setup for characterization of electrical properties of BNNSs on Mo (a) and AlN (b), respectively, typical I-V properties of BNNSs with (a1) membrane thickness of 7 nm and (a2) 30 nm on Mo substrates, and with membrane thickness of (b1) 2 nm and (b2) 30 nm on AlN substrates at different temperature.

#### 5.2.4 Resistivity Calculations

Using a simple wire mode for resistance  $R = \rho l / A$  where the  $l$  is its length, and the  $A$  is its cross-sectional area; we can estimate the resistivity  $\rho$  (the constant of proportionality) of BNNSs. From Fig. 5.8a1, the obtained resistance is  $4 \times 10^6 \Omega$  (ten electrical voltages yield  $2.5 \times 10^{-6}$  amp electrical current) at room temperature. Since the thickness of the BN membrane is 7 μm and the area of the cross section is around  $5 \times 5 \text{ mm}^2$ , the resistivity can be estimated around  $\rho = 7.1 \times 10^6 \Omega \text{m}$ . From Fig. 5.8a2, it is found that the resistance of the BNNSs is only 1 Ohm (one electrical voltage yields one amp electrical current as seen in Fig. 5.8a2). Because its membrane thickness is 30 nm and the cross-sectional area is around  $5 \times 5 \text{ mm}^2$ , the resistivity can be estimated around  $\rho = 4.2 \times 10^2 \Omega \text{m}$ . Large differences of the resistivity or conductivity coefficients probably indicated that the BNNSs with different thickness would have very different mechanisms that affect their resistances. Super thin BNNSs appear quasi-metal properties.

Effect of temperature on I-V properties for thick BN membrane is partially discussed in our papers [15]. However, in the present case for super thin BNNS sample, I-V properties remain nearly unchanged with temperature variation, indicating its stable properties.

Similar measurements are also conducted for BNNSs on ceramic substrate based on Fig. 5.8b setup. Fig. 5.8b1 shows typical I–V characteristics of the BNNSs with AlN substrate where physical properties of individual BNNS are nearly same as that in Fig. 5.8a1. This is in agreement with the previous experimental results that the substrates do not obviously affect properties of the synthesized BNNSs by much [16]. It is noticed slightly nonlinear relationships between the I-V curves appear, probably indicating that doping or surface modifications have occurred during the deposition of electrodes on the samples. Interest is that decreasing in the thickness down to 60 times from 2000 nm (Fig. 5.8b1) to 30nm (Fig. 5.8b2) (consequently, the cross-sectional area decreases down to 60 times as seen in Fig. 5.8b) would yield around 200 times of decreasing of electrical current at a fixed voltage.

Experimental data (Fig. 5.8b1) from Fig. 5.8b setup indicate that the obtained resistance is  $5.6 \times 10^{10} \Omega$  (one thousand electrical voltage yields  $0.18 \times 10^{-7}$  amp current) at room temperature. Because the distance between the two electrodes is 0.5 mm, the cross-sectional area of the BN membrane is  $2 \mu\text{m} \times 5 \text{ mm}$ , the resistivity is then estimated around  $\rho = 1.1 \times 10^6 \Omega\text{m}$ . In contract from Fig. 5.8b2, we have the resistance of  $1.2 \times 10^{13} \Omega$  (one thousand electrical voltages yield  $0.0825 \times 10^{-9}$  amp current) at room temperature where the area of the cross section is  $30 \text{ nm} \times 5 \text{ mm}$ , from which the resistivity is estimated around  $\rho = 3.6 \times 10^6 \Omega\text{m}$ .

### **5.2.5 Effect of Temperature on I-V Characteristics of BNNSs/AlN**

Effects of temperature on the electrical properties of BNNSs/AlN have also been studied. The data from Fig. 5.8b1 and 5.8b2 clearly show that the higher the temperature, the lower the

resistance is. This is similar to that in the case of the thick film (Fig. 5.8a1) but very different from that shown in Fig. 5.8a2. As we know that the resistivity/conductivity of BNNSs is actually determined by two factors: the concentration of free carriers available to conduct current and their mobility. There are two basic types of scattering mechanisms that influence the mobility of electrons and holes: lattice scattering and impurity scattering. Lattice vibrations cause the change of mobility with increasing temperature. However, the mobility of the carriers in a semiconductor is also influenced by the presence of charged impurities. Impurity scattering is caused by crystal defects such as ionized impurities. At lower temperatures, carriers move more slowly, so there is more time for them to interact with charged impurities. As a result, when the temperature decreases, impurity scattering increases and the mobility decreases. This is just the opposite of the effect of lattice scattering. The total mobility then is the sum of the lattice-scattering mobility and the impurity-scattering mobility. Therefore, effect from scattering always exists at any 3D bulk material or thick films (Fig. 5.8 a1). As a result, effect of temperature on the resistivity/conductivity of material can be easily identified.

#### **5.2.6 Effects of Temperatures on Resistivity of BNNSs of Different Thickness**

The effect of temperature on the resistivity of BNNSs of different thickness is presented in Fig. 5.9. In the 2D case, effect of temperature on the resistivity/conductivity depends on the direction of observation. Vibration and mobility caused by thermal energy in 2D only occur in the horizontal/transversal direction. If electrical current were directed to vertical/longitudinal direction as shown in Fig. 5.8a, scattering caused by temperature would not seriously affect electrical currents (Fig. 5.8 a2). Consequently, I-V curves would remain unchanged with the increase of the temperature. In contrast in the case with Fig. 5.8b experimental setup where the electrical current is directed in the horizontal/transversal direction, scattering caused by

temperature would unavoidably affect the electrical current, resulting in the variation of the resistivity/conductivity of the BNNSs as shown in Fig. 5.8b1 and 5.8b2.

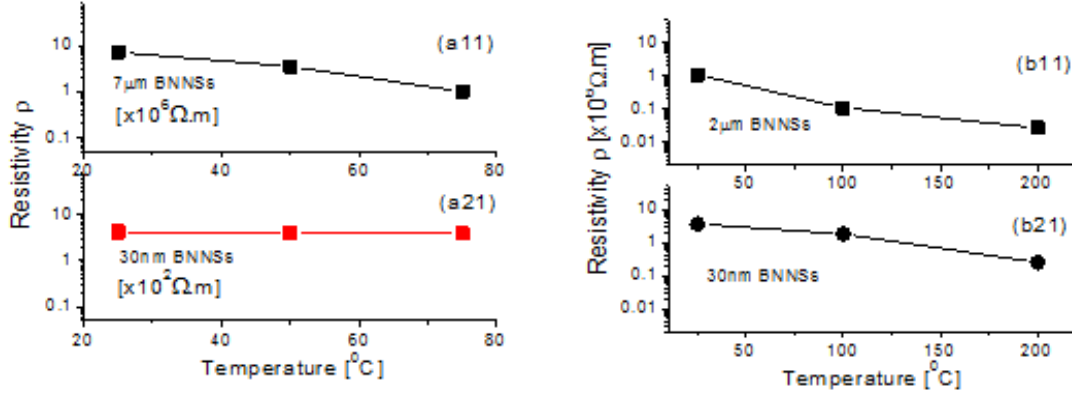


**Figure 5.9** Effects of temperatures on resistivity of different thickness (a11) and (a21) of BNNSs characterized using setup (Fig. 5.8a), and (a11) and (a21) by using setup (Fig. 5.8b), respectively.

### 5.3 Optical Measurements of BNNSs

#### 5.3.1 Cathodoluminescence Spectroscopy of BNNSs

To investigate optical properties of synthesized BNNSs, which are indicative of the material quality needed for developing a prototype DUV photo-detector device, cathodoluminescence (CL) was conducted at different temperatures. An example of the room temperature CL spectrum observed for studied BNNSs samples is shown in Fig. 5.10. The CL spectrum is dominated by an intense UV luminescence band peaking at 226.9 nm with a shoulder on the lower energy wing at ~233 nm and the featureless low intensity emission background at longer wavelengths. The comparison between normalized CL spectra measured with increased spectral resolution from 200 nm to 290 nm at 12 K and 300 K, respectively, is shown in the inset of Fig. 5.10. It is seen that the CL spectrum measured at 12 K shows several peaks located at ~215 nm, 220 nm, 222.6 nm, 226.5 nm and 233 nm, respectively. In reported here CL experiments the electrons beam diameter was  $\sim 1 \text{ mm}^2$  and probed/excited simultaneously

multiple BNNSs having distinct substrate-*h*-BN hetero-boundary conditions. As demonstrated by XRD [15] and Raman spectroscopy results, we believe, that studied BNNSs, in overall, are highly homogenous; however retain certain degree of inhomogeneity typical for nanoscale materials. Thus the observed CL spectra convolve spectral features of all individual BNNSs visualized with statistical probability reflecting the overall sample morphology. Tentatively, we assign the highest energy peak seen in CL spectrum at 215 nm to the strain free *h*-BN free exciton luminescence. Other CL peaks between 220 nm and 240 nm could be assigned, subject to further investigation, to excitons bound by impurities or defects, or a phonon replica of free exciton luminescence bands [17]. The deep UV CL band shape changes with increased temperature, the observed spectral features became less resolved, due to inhomogeneous broadening; however the peaks positions do not change significantly. Furthermore, the room temperature CL spectrum shows a broad band emission tail between 260 nm to 280 nm probably attributable to vacancies or residual stresses produced in different layers of the nanosheets [18]. However, at this time we cannot completely rule out that the shape of observed deep UV CL spectrum is also affected by the different morphologies of BN nano-material. Recently Watanabe *et al.* [19] investigated the low temperature CL of free standing *h*-BN single crystals grown by high temperature - high pressure method. Interestingly enough they reported on the observation of the CL spectra change caused by plastic deformation of free standing *h*-BN crystal. The evolution of the CL spectra exhibited red-shift of the strongest excitonic peak position from 215 nm to 227 nm at 300 K [19]. It was proposed that this effect is due to the exciton localized around glided planes lowering luminescence energy under applied pressure induced by the weak coupling between the *h*-BN  $sp^2$  layers as compared to that between B and N within a layer. Our BNNSs samples were synthesized on metal substrate and hence the *h*-BN is subjected to the

strain developed at substrate-*h*-BN hetero-boundary. Thus, we believe that majority of studied BNNSs are subjected to hetero-boundary strain whereas some of BNNSs are less plastically deformed (*e.g.* different orientation of BNNSs with respect to substrate). It was reported by Watanabe *et al.* [20] that the layered structure of *h*-BN could favor the self-trapped exciton formation because of stacking disorder. Two competing processes following the excitation were considered. In the first one the excited state lowers its energy by inducing a local distortion resulting in a self-trapped exciton formation. In the second process, the excited state lowers its energy by transfer from one site to a neighbor site forming so-called free exciton. Generally, low coordination number of atoms in the crystalline *h*-BN lattice favors a formation of self-trapped exciton [21]. The BNNSs are made of two dimensional well separated layers in which each atom is covalently bound to three neighbor ones. This low coordination number supports further the preferential formation of self-trapped exciton in BNNSs. Consequently, the observed CL spectra are dominated by a self-trapped exciton peak (in other words a red-shifted free exciton peak) at ~227 nm in studied temperature range whereas the free exciton peak of BNNSs subjected to reduced strain or strain-free is observed at ~215 nm in agreement with literature [19].



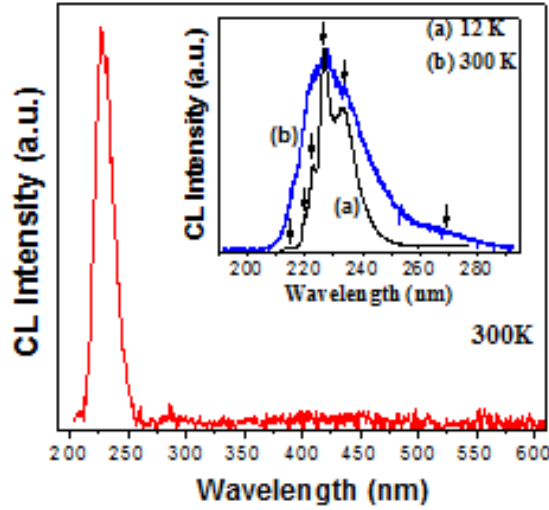
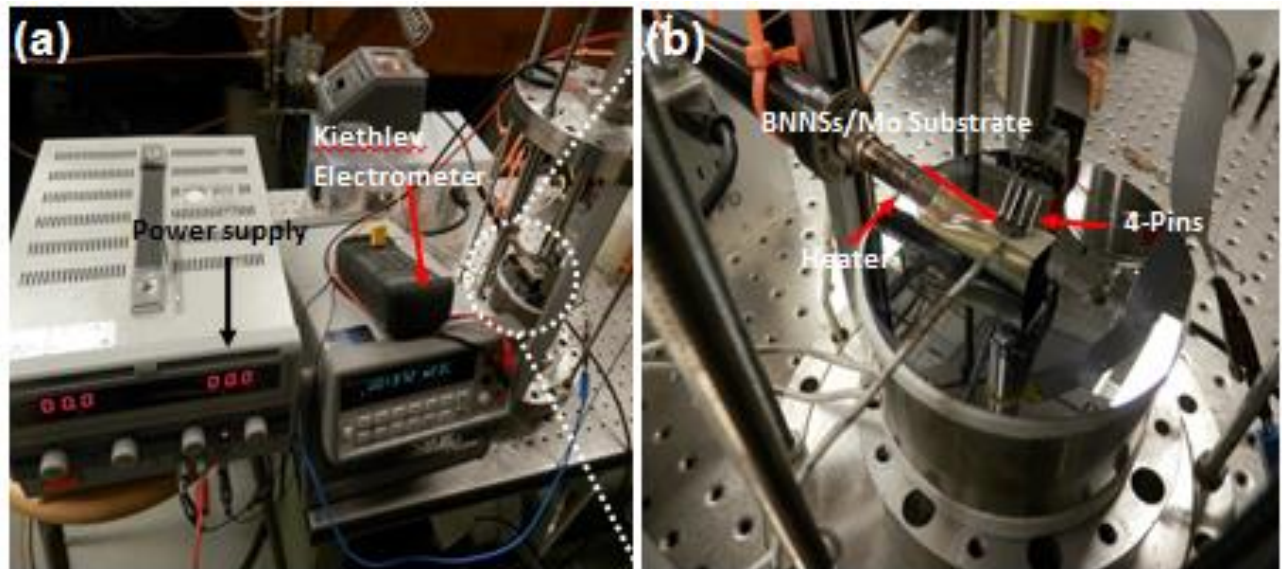


**Figure 5.10** CL spectrum of BNNSs excited by electron accelerated with 6 keV at 300 K. Inset shows comparison between normalized deep UV CL spectra of BNNSs measured at 12 K (a) and 300 K (b). Vertical arrows indicate excitonic recombination peaks and a deep level related emission band centered at 270 nm, respectively.

### 5.3.2 Fabrication of DUV Photo Detector

Development and assessment of prototype DUV detectors have been conducted by many groups in the past [19, 22-24]; however most of the results reported in literature considered bulk BN crystals and their optical properties studied using CL spectroscopy at room temperature. In this work, we support the CL results obtained for as synthesized BNNSs by developing a prototype DUV photodetector and demonstrating its performance in detecting UV photons across deep UV region. Figure 5.11 shows an experimental apparatus used to characterize a BNNSs-based semiconductor/metal-junction DUV photo detector device through the 4-pin electrodes approach. In typical experiment the BNNSs/Mo substrate is connected in series through a 4-pin electrodes head to a precise resistor, power-supply and a Keithley electrometer, respectively (Fig. 5.11a). Figure 5.11b shows the enlarged image of the 4-pins electrode probe head prior connecting to the surface of BNNSs sample. Figure 5.11b shows the schematic diagram of the

circuit used for testing DUV devices. The device response was investigated under different UV lights radiation keeping DUV detector bias conditions unchanged. Different pen-ray deep UV lamps emitting at 254 nm, 302 nm, and 365 nm wavelengths, respectively have been used with photon flux intensity  $\sim 2 \text{ mW/cm}^2$  on the surface of the test detector. The area of DUV detector exposed to UV irradiation was typically  $10 \text{ mm}^2$ . Figure 6d shows responses of the typical DUV detector to pulsed UV light stimulus. A rapid increase in the output electrical current is observed for irradiation with 254 nm indicating good initial-characteristic of the device in deep UV spectral range. Multiple BNNSs-based DUV-photo detector prototypes were fabricated and tested for repeatability and on-off switching performance under these conditions without any indication of failure of potential degradation. When the BNNSs-based DUV-photo detector was exposed to UVB (302 nm) and UVA (365 nm) radiation keep all other parameters the same as for UVC light no output signal from the detector was detected



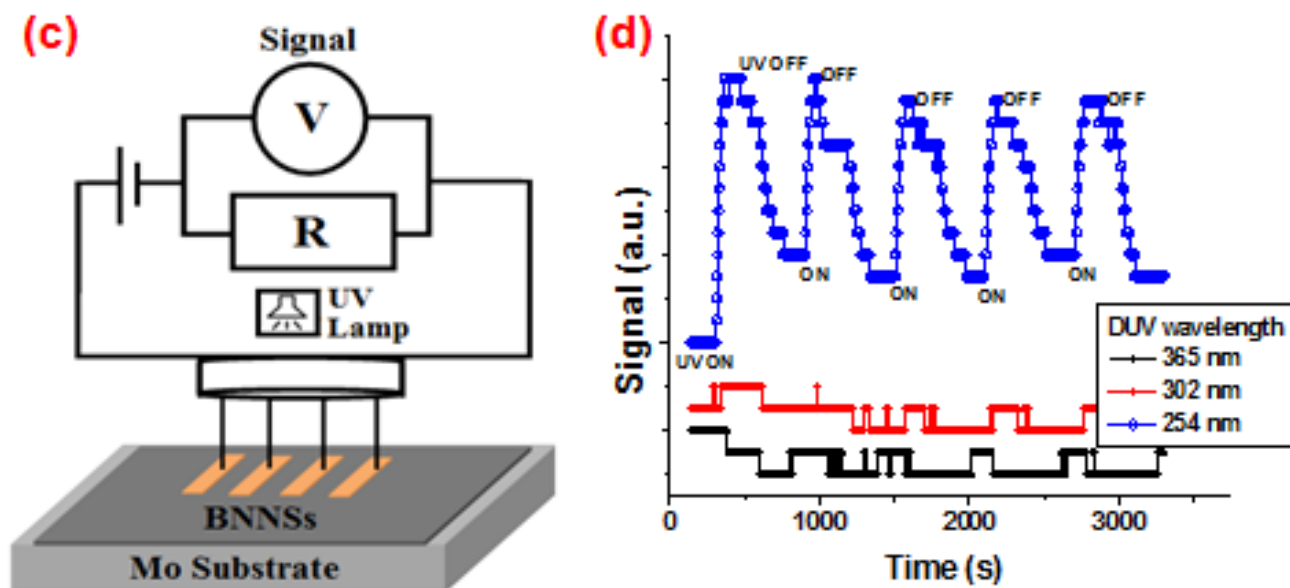


**Figure 5.11** (a) A photograph of the setup installed for DUV measurements. (b) Assembly of a four-pin detector probe/system, (c) A diagram of electrical circuit used for DUV tests, (d) Typical responses of a BNNs-based DUV-photo detector prototype under selected UV photos radiation.

It is clear from the response of fabricated BNNs-based DUV-photo detector to UV irradiation with different UV photons energy that fabricated BNNs material is rather free from deep mid-gap energy levels induced by impurities and/or defects absorbing 302 nm and 365 nm photons. The room temperature CL spectrum shown in Fig. 5.11 confirms that excitation with 254 nm photons is absorbed more efficiently due to the presence of a broad band emission tail extending up to 280 nm. Thus the photons with energy corresponding to the UVC region can be absorbed by BN mid-gap energy states promoting electronic transition across BN forbidden gap. It should be mentioned here that, close proximity of BNNs and metal electrode subjected to the strong external electric field effectively remove optically generated electrons increasing the overall sing BNNs-based DUV-photo detector sensitivity.

### 5.3.3 Sensitivity of DUV Photo Detector

We have evaluated the sensitivity of a developed detector by exposing its area ( $\sim 1 \text{ cm}^2$ ) to the UV light with intensity  $\sim 2 \text{ mW/cm}^2$  on the surface at room temperature. The calculated output power is  $\sim 2 \text{ }\mu\text{W}$  and the ratio between the output electrical power and the input optical power is  $\sim 1\%$ . We believe that these experimental parameters can be further improved by optimization of the photo-detector fabrication process (*e.g.* electrical contact).

### 5.3.4 BNNSs/Mo and BNNSs/Si based Prototypic DUV Photo Detectors

In order to carry on research on the fabrication of DUV detectors, two different prototypes DUV detectors were developed and tested. One is based on BNNSs/Mo junction and other is based on BNNSs/Si junction. The schematic illustrations of the electronic setup for prototypes DUV detectors are shown in Fig. 5.12 (a-b) where two types of substrates: metal (Mo, Cu) substrate and ceramic (AlN and Si) were used. The copper pads act as electrodes, the effective resistance between the two electrodes was only from the h-BN membranes that were serially connected to an external precise resistor, a switcher, and a power supply. Four-pin electrodes method (as explained in section 5.3.2) was modified and introduced to reduce the accumulative effect during measurements.

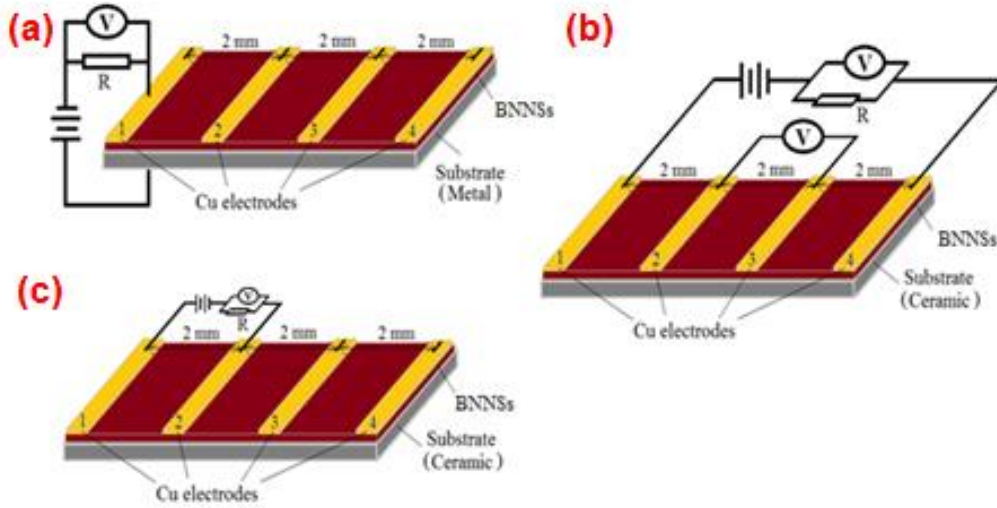


**Figure 5.12** (a-c) Schematics for different electronic setup used to collect DUV data.

Pen-Ray Deep UV lamps with wavelengths of 365, 304, 254 nm, respectively, produced by UVP, LLC were used as light sources for the characterization of prototypic BNNs-based DUV detectors above. Light intensity of UV lamps on the surface of the detectors was around  $\sim 2$  mW/cm<sup>2</sup>. The exposed area of detector to UV light is around  $\sim 10$  mm<sup>2</sup>. When the detector was exposed to UV light, the photonic energy of the UV light is absorbed that excites the valence electrons, resulting in its resistance variation. Detailed description of light source and light intensity can be found in literature [25]. Preliminary results already indicated there is not response or output when the BNNs based DUV-photo detector is exposed to 305 nm and 365 nm or longer wavelength of light irradiation of UV light sources. Therefore in the following experiments, the focused of experiments were just to monitor the response for UV light of wavelength of 254 nm.

### 5.3.5 DUV Detector based on Thin BNNs

Fig. 5.13 (a) shows response when the prototypic thin (340 nm prepared with 300 pulses of plasma beam) BNNs-based UV detector is cycled between “on” and “off” UV light source

(wavelength of 254 nm). The outputs of the detectors appeared well repeatable. Experimental data indicated that the response time and recover time is around 1.5 sec and 3 sec, respectively. Actual response time and recover time should be shorter. This is because time delay for reaching full intensity for UV lamps after switching on lamp, and florescence after switching off the lamp would affect the measurement results. Therefore, dynamic calibration of UV detectors was necessary. Relatively, the BNNSs/Mo based detector has poor response time and recover time. Comparing the data shown in Fig. 5.13 (a) and in Fig. 5.13 (b), ones can easily found that the BNNSs/Si based detector has higher sensitivity or quicker response than that of the BNNSs/Mo based detector. The difference between the two prototypes should be related to their interfaces between the BNNSs and substrates. Recently reported experiments/results showed there are no obvious differences of morphologies and crystalline structures of BNNSs prepared on the different surfaces of AlN ceramic, or Si wafer, or molybdenum substrates [16]. However, to carefully examine the cross section of the sample, differences of interfaces between the first over layer BNNSs and the substrates clearly visible. Three possible factors might determine the quality of interfaces: different lattice constants, surface energies, and flatness of the surface of the substrate. In general case, the quality of interface between the BNNSs and Si wafer is much better than that between the BNNSs/Mo. Since the BNNSs/Si based detectors have higher sensitivity, this indicates that the interface between the substrate and the BNNSs might dominate in detector properties.

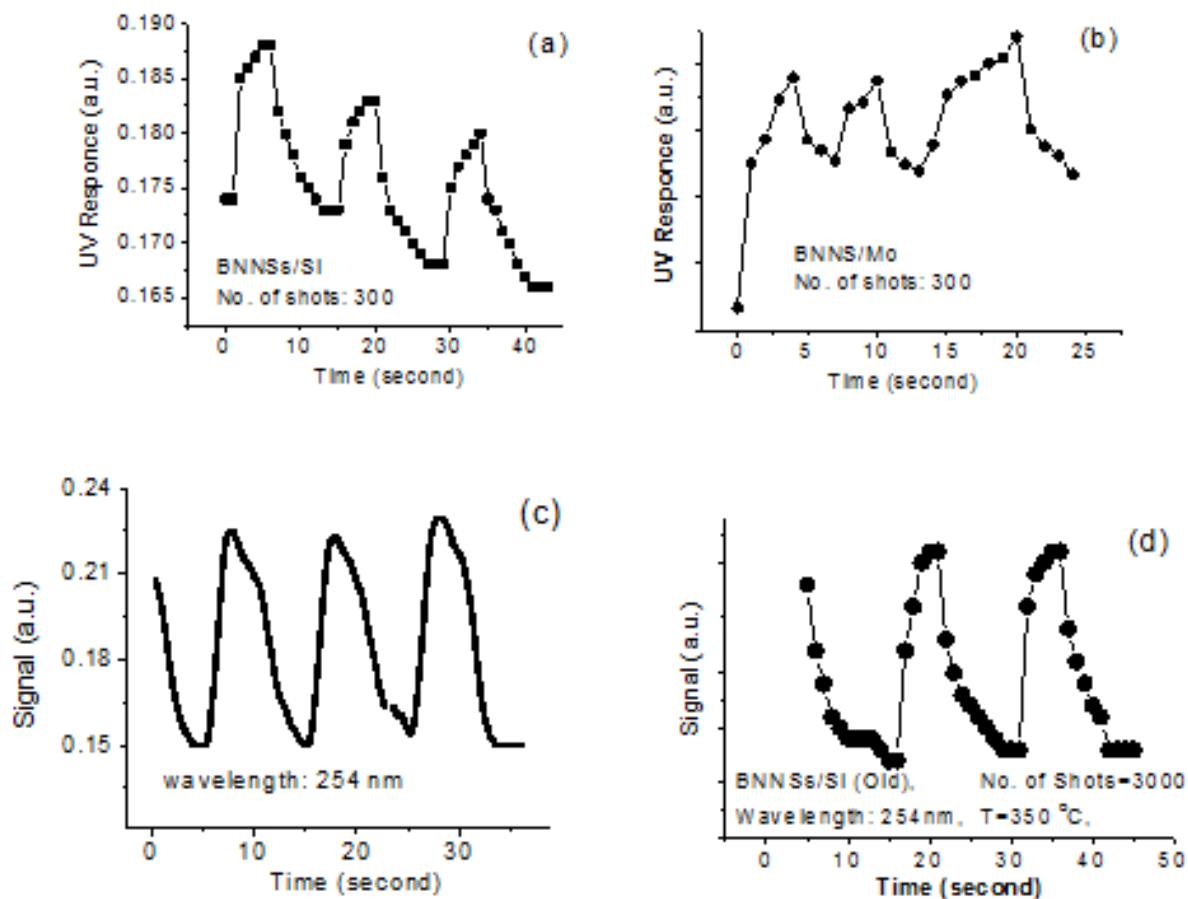


**Figure 5.13** Response curves for, (a) BNNSs/Si DUV detector and (b) BNNSs/Mo-based DUV detectors are cycled between “on” and “off” 254 nm UV light source. Comparison made between the responses of the detectors based on (c) fresh BNNSs samples and (d) 6-months old BNNSs samples.

### 5.3.6 DUV Detector based on Thick BNNSs

Fabrication and characterization of slightly thick (5  $\mu\text{m}$  prepared with 3000 pulses) BNNSs membrane based detector is also conducted and the results are shown in Fig. 5. 13 (c) with the same UV light source. An important stability or repetition feature is clearly visible from the data of cycled test. Two conclusions can be made after comparison of Fig. 5.13 (a) and Fig. 5. 13 (c): 1) thin BNNSs based detector has quicker/shorter response time (1.5 sec) than that (1.65 sec) of the thick BNNSs based detector, and 2) the thin BNNSs based detector has lower

sensitivity (4.2%) than that (22.2%) of the thick (5  $\mu\text{m}$ ) BNNSs based detector where the definition of the sensitivity is made as  $(I_{\text{max}} - I_{\text{min}})/(I_{\text{max}} + I_{\text{max}})$  and  $I$  is the output of electrical signal from the detector. The result above clearly indicates that at the level of enough sensitivity, super thin BNNS membrane - based detector should have quick response. No outstanding sensitivity is possibly attributed to two facts that 1) deep UV light has deep penetration length, and 2) tunneling effect of super thin BNNS would result in a poor conversion efficiency between the deep UV light and the electrical signal. In order to solve this problem, multi-layer structure has to be fabricated.

Studies of comparison of fresh sample and 6-months old BNNSs based UV detectors are also conducted as shown in Fig. 5.13 (c) and (d) during cycled between “on” and “off” 254 nm UV light source. As seen the average response time and the sensitivity of the detector remains nearly unchanged, indicating BNNSs based detectors have long life, reliability, and cost-effectiveness. In fact, BNNSs offers the best combination of resistance to oxidation, and resistance to chemical degradation with iron-based materials. It is an excellent material with wide band-gap semiconductor, high thermal conductivity, and very good transparency ranging from visible to microwave spectra. BNNSs have the advantage over diamond in its resistance of much higher temperatures in air without loss of its crystalline structure and without melting. All these factors have encouraged many recent experimental studies on growth, characterization, and applications of new BNNSs materials based on various techniques.

#### **5.4 Gas Sensing Properties of BNNSs**

In order to study the gas sensing properties of nanosheets, a prototype of BNNSs-based gas sensor is designed and fabricated. A good sensor has several important parameters for example, sensitivity, selectivity, response time and recovery time, as well as repeatability. To



investigate these properties in our sensor, the static and dynamic testing of the sensor device for different gases at the same concentration was performed. A chamber was employed to provide different gas concentration levels in incremental steps, while temperature remained unchanged at 150 °C. Each step was maintained at constant parameters till the voltage reading reached a steady value. The sensing mechanism is based on the resistance change caused by the reaction of the absorbed gas molecules at the surface of BNNSs. Basically, sensor comprises of chip (micrometer) scale metal fringes (electrodes), sensing element (BNNSs), a heater, power supply, and electric digit meter. Cycling tests of sensing behaviors of newly designed sensors are conducted in a calibrated apparatus [26]. Oxygen (O) and methane (CH<sub>4</sub>) gases are used independently as the targeted gasses for eight cycles, from which the response time ( $T_{res}$ ) and recovery time ( $T_{rec}$ ) of the sensor are investigated as shown in Fig. 5.14 (a,b).

The sensitivity (S) of the sensor is defined as,  $S(\%) = (|R_s - R_v|)/R_v$ , where  $R_s$  represents the resistance of the sensor when gas is introduced in the chamber and  $R_v$  is the resistance in vacuum [27]. When sensor is exposed with the gas (O or CH<sub>4</sub>), the corresponding change in resistance is recorded as shown in Fig. 5.14(a,b). The value for “S” is calculated from the cycle in which maximum change in the resistance is recorded. In the case of O gas at (2000 mtorr), maximum value of “S” was recorded around 1.5 when the output signal was stable, whereas  $T_{res}$  and  $T_{rec}$  were around 80sec and 110sec, respectively as shown in figure 3a. In contrast, for the case of CH<sub>4</sub> gas (Fig. 5.14 (b)), at the same gas concentration, the change in resistance of the sensor upon exposure of gas is much stronger. The relative intensity of the signal recorded for CH<sub>4</sub> is larger than that of recorded to O gas, indicating BNNSs-based sensor has high sensitivity ( $S \approx 7.8$ ) or selective properties. The possible reason is that methane molecules are polarized, thus they can easily be absorbed by the surface and grain boundaries of BNNSs and then change

the conductivity of BNNSs. Furthermore,  $T_{\text{res}}$  ( $\approx 10\text{-}15$  sec) and  $T_{\text{rec}}$  ( $\approx 15\text{-}20$  sec) are recorded down to few seconds. Actual  $T_{\text{res}}$  and  $T_{\text{rec}}$  should be even shorter than the observed value. This is because in the present case, time delay in switching on or off the valves of gas inlet and outlet, as well as low pumping capacity ( $7\text{m}^3/\text{h}$ ) affect the measurement results.

Eight cycles of experimental testing showed that the sensor has good repeatability. But it is noticed that in the first cycle when gas is introduced into the chamber, the response of the sensor is not unique. A tentative interpretation is that the contamination (humidity or dust particles) on the surface of BNNSs affects the sensitivity of the sensor. After first cycle, response and repeatability of the sensor in each cycle of gas “in” and “out” is almost identical. This is due to the fact that the impurities from the surface of BNNSs might be pumped out with the gas. When the gas is switched off, the resistance of the sensor drops slowly. There are two possible steps involved after switch off the gas. In the first step, gas molecules are pumped out from the chamber. During this interval of time (between the  $T_{\text{res}}$  and the  $T_{\text{rec}}$ ), large amount of gas is still adsorbed on the surface of BNNSs. Consequently, the conductivity or response of sensing material changes slowly as evidenced shown in each cycle. In the second step, continuous pumping results in quick desorption of gas molecules from the surface of BNNSs. Slight variation in the numbers of molecules on the surface of BNNSs can cause large change of electrical properties of BNNSs. That is why during this step, signal drops rapidly.

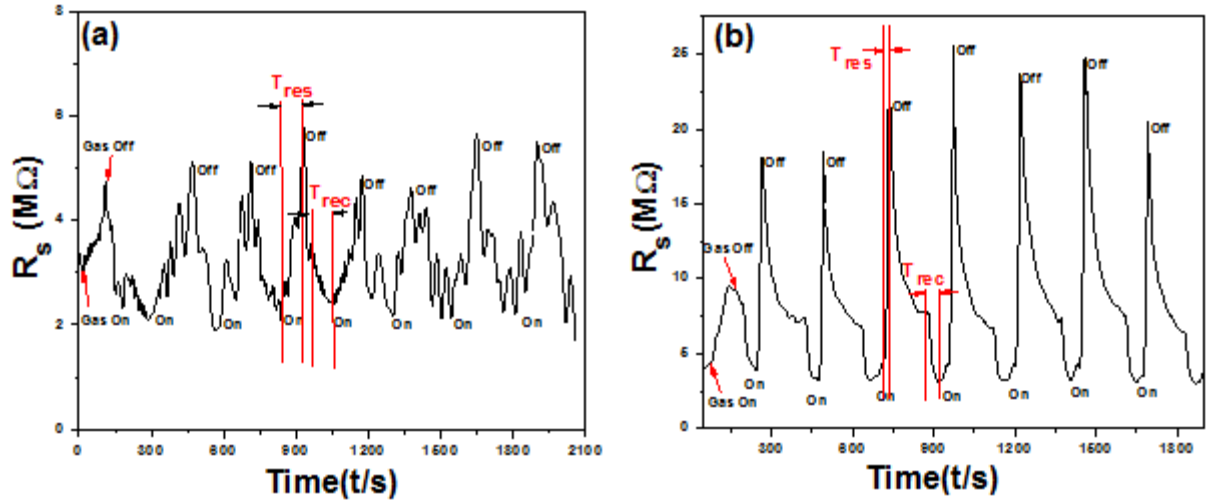


**Figure 5.14** Response of BNNSs-based gas sensor to, (a) O and, (b)  $CH_4$  gas.

BNNSs-based gas-sensors operate by measuring changes in electrical resistance of the BNNSs upon exposure to the gas. Though the exact mechanism is still to be investigated, it appears that free electrons can move easily through the surface and across the boundaries of BNNSs. Briefly, when gas is introduced in the chamber, it is adsorbed onto the surfaces as well as at the boundaries of BNNSs that removes free electrons, creating a potential barrier. This is manifested as an increase in resistance of the sensor as shown in curves (Fig. 5.14).

### 5.5 Field Emission Characteristics of BNNSs

To get inside into the optical response of the BNNSs-metal DUV photo-detector we have evaluated also the field emission properties of BNNSs. Figure 5.15 shows the field-emission characteristics (emission current density) of the BNNSs as a function of applied macroscopic electric field. The field emission characteristics were measured in a custom made system, in which a molybdenum rod of 3 mm O.D. (area:  $0.071 \text{ cm}^2$ ) serves as the anode. Using this configuration, the macroscopic surface electric field ( $E_s$ ) on the sample (*i.e.* cathode) can be estimated accurately by  $E_s = V/d_{CA}$ , where  $V$  is the voltage applied to the anode and  $d_{CA}$  is the

distance between the cathode and the anode controlled with a micropositioner with an accuracy of  $\pm 2 \mu\text{m}$ . All the measurements were taken at  $d_{\text{CA}} = 100 \mu\text{m}$  and at pressure not exceeding  $5 \times 10^{-7}$  Torr. The current was measured with a Keithley 6517A electrometer and the power supply used was a Stanford Research Systems PS350. Current lower than 1 pA was considered as the background noise. The turn-on field (the field necessary to produce a current density of 1 nA/cm<sup>2</sup>) is estimated in spite of the BNNSs sample.

The average turn-on electric field was calculated from the anode voltage and the spacing between the anode electrode and the sample surface. The electric field, at the emission current of  $\sim 1$  nA designated as a turn-on electric field for the BNNSs, is estimated to be 8.3 V/ $\mu\text{m}$  as shown in Fig. 5.15 (a). These results can be analyzed in terms of the Fowler-Nordheim (*F-N*) theory [28,29] which describes the electron emission current barrier by tunnelling process. The *F-N* plot where  $\ln(J/E^2)$  vs.  $(1/E)$  of *h*-BN samples is shown in Fig. 5.15 (b) [30]. The respective *F-N* equation is given by the expression:

$$J \propto \left( \frac{E_{\text{local}}^2}{\phi} \right) \exp\left( \frac{-B\phi^{3/2}}{E_{\text{local}}} \right) \quad (\text{Eq. 1})$$

where,  $\phi$  is the work function for *h*-BN, and  $B$  is a constant equal to  $-6.83 \times 10^3 \text{ V(eV)}^{3/2} (\mu\text{m})^{-1}$ .

The slop of *F-N* plot is given by the expression:

$$\beta = \frac{B\phi^{3/2}d}{\text{slope}} = \frac{-(6.83 \times 10^3)\phi^{3/2}}{\text{slope}} \quad (\text{Eq. 2})$$

where,  $\beta$  is the geometric field enhancement factor and  $d$  is the anode to cathode distance. This slope represents the combined effect of the work function and the enhancement of the local electric field. If the electron emission is controlled by the tunnelling mechanism, the *F-N* plot presents a nearly straight line with a negative slope suggesting the electron emission process due

to  $F-N$  tunneling [31,32]. Using work function ( $\phi = 6$  eV) for  $h$ -BN sample [33] the field enhancement factor was estimated to be  $\beta = 1040$  from the slope of  $F-N$  plot of BNNSs sample. The high value of  $\beta$  factor indicates that the few atomic layer of “white graphene” BNNSs is an excellent material for field emission applications.

Electron emission phenomenon can be understood well by considering geometrical feature of BNNSs *i.e.* emission from the surface and curled edges. Emission from surface of BNNSs depends on surface roughness and defects levels. In our case, surface of the BNNSs is highly flat having negligible structural defects making horizontal surfaces less effective for the electron emission process. On the other hand, curled or vertical edges of BNNSs could have high field emission [34,35]. Moreover, defects density in the BNNSs is considered to be higher on the edges of vertical nanosheets as compared to the surface of nanosheets. Also, the geometrical features of the BNNSs increased the extraction of electrons at lower threshold electric field (8.3 V/ $\mu$ A) and hence an increase in the enhancement factor was observed [36].

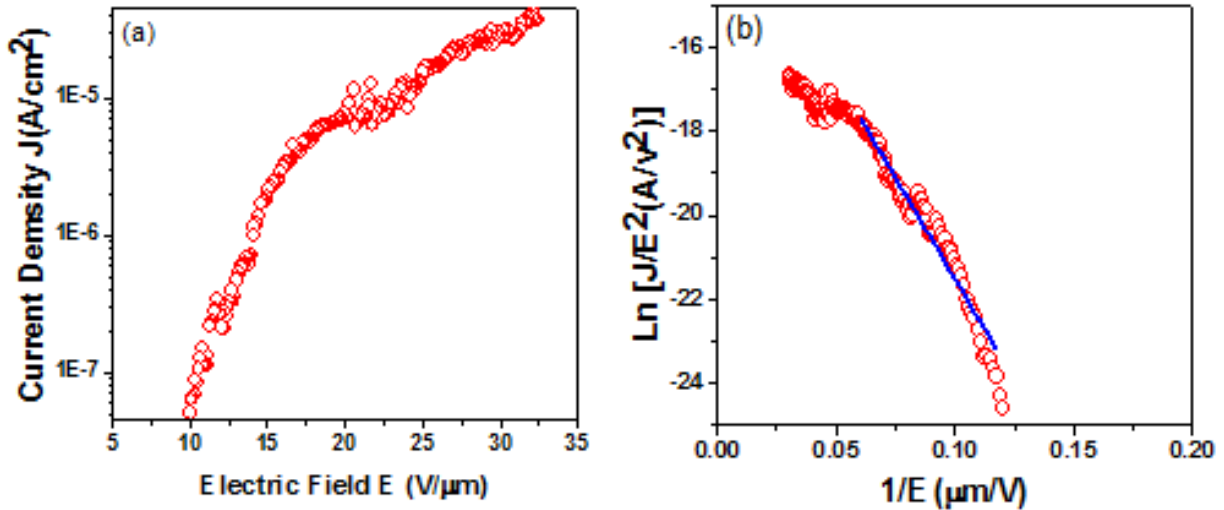


**Figure 5.15** Field emission characteristics of BNNSs emission current density (a) and  $F-N$  plot of nanosheets (b).

## 5.6 Conclusions

In summary, BNNSs material exhibits outstanding semiconducting properties and is a material of choice for developing, Schottky diode, DUV optical detectors and resistance based gas sensor. Carbon doping in BNNSs produce Schottky barrier diode whose forward and reverse electrical characteristics are in excellent agreement with the characteristics of a simple PN junction diode.

The output characteristics of Schottky diode highly dependent on thickness and alignment of BNNSs, evidenced from I-V measurements conducted from Schottky diode based on longitudinally or transverse laid BNNSs. Either vibration or mobility caused by thermal energy only occurs in the horizontal/transversal direction. Therefore, electrical current directed to vertical/longitudinal direction would not be affected by scattering. Consequently, the resistivity of BNNSs is extremely small, and this value remains nearly unchanged with the increase of the temperature. This could be attributed to quantum tunneling effect.

The prototype BNNSs-Mo based DUV-optical sensor was developed and shown very good response to UV light with wavelengths below 254 nm. It is concluded that fabricated device is only sensitive to photons with energy greater than 4 eV. Such sensors can be useful for extraterrestrial applications where broad spectrum of UV light is typically available. This confirms that the high quality BNNSs material may surpasses other more technologically developed semiconductor (e.g GaN, ZnO and diamond) for developing specific optical devices for aerospace applications.

Characterizations of the fabricated detectors indicate that the BNNSs/Si based detector has higher sensitivity or quicker response than that of the BNNSs/Mo based detector. The quality of the interface between the substrate and the BNNSs dominates in detector properties.

From the data of cycled test of different thickness based detectors, we conclude that thin BNNSs based deep UV detector has quicker/shorter response time (1.5s) than that (1.65s) of the thick BNNSs based detector, but 1<sup>st</sup> type of detector has lower sensitivity (4.2%) than that (22.2%) of the 2<sup>nd</sup> type of detector. From studies of comparison of fresh sample and 6-months old BNNSs based UV detectors; we conclude the BNNSs based detectors have long life, reliability, and cost-effectiveness. The evidence is that the response time and the sensitivity of the detector remains nearly unchanged for long period of time.

From rapid response of BNNSs based gas sensor to CH<sub>4</sub> gas and slow response to O gas indicated that BNNSs is an excellent material to sense gas of polar molecules chemistry.

## 5.7 References

- [1] Zhang H. X.; Feng, P. X. ACS Appl. Mater. Interfaces 2012, 4, 30.].
- [2] Yang, B. Q.; Feng, X. P.; Kumar, A.; Katiyar, R. S.; Achermann, M. J.; Appl. Phys D. 2009, 42, 195402.
- [3] Rubio, A. Nat. Mater 2010, 9, 379.
- [4] Song, L.; Liu, Z.; Reddy, A. L. M.; Narayanan, N. T.;Tijerina, J. T.; Peng, J.; Gao, G.; Lou, J.; Vajtai, R.; Ajayan, P. M. Adv. Mater. 2012, 1.
- [5] H. X. Zhang, and P. X. Feng; ACS Appl. Mater. Interfaces 2012, 4, 30–33; dx.doi.org/10.1021/am201435z.
- [6] Carpenter, L. G.; Kirby, P. J. J. Phys. D: Appl. Phys. 1982, 15, 1143.
- [7] Pejova, B.; Grozdanov, I.; Taunsevski, A. Mater. Chem. Phys. 2004, 83, 245.
- [8] Pejova, B.; Grozdanov, I.; Taunsevski, A. Mater. Chem. Phys. 2004, 83, 245.
- [9] Tan, Y. W.; Zhang, Y.; Stormer, H. L.; Kim, P. Eur. Phys. J. Spec. Top. 2007, 148, 15.
- [10] Barone, V.; Hod, O.; Scuseria, G. E. Nano Lett. 2006, 6, 2748.
- [11] Han, M. Y.; Ozyilmaz, B.; Zhang, Y.; Kim, P. Phys. Rev. Lett. 2007, 98, 206805.
- [12] Ozyilmaz, B.; Jarillo-Herrero, P.; Efetov, D.; Kim, P. Appl. Phys. Lett. 2007, 91, 192107.
- [13] A. I. Kingon, J.-P. Maria, S. K. Streiffer, Nature, 406, (2000) 1032; b) G. D. Wilk, R. M. Wallace, J. M. Anthony, J. Appl. Phys., 89, (2001) 5243.
- [14] M. Depas, R. L. Van Meirhaegue, W. H. Laflère, F. Cardon, Solid- State Electron, 37, (1994) 433.
- [15] Muhammad Sajjad, Gerardo Morell, and Peter Feng, “Advance in Novel Boron Nitride Nanosheets to Nanoelectronic Device Applications”, ACS Applied Materials & Interfaces 5 (11), (2013) 5051.
- [16] Muhammad Sajjad, Majid Ahmadi, Maxime Guinel, Yi Lin, Peter Feng, “Large-scale synthesis of single-crystal and polycrystalline boron nitride nanosheets”. Journal of Materials Science, 48(6), (2013) 2543.
- [17] K. Watanabe, T. Taniguchi, H. Kanda, Nature Materials 2004, 3, 404.
- [18] K. Watanabe, T. Taniguchi, T. Niiyama, K. Miya, M. Taniguchi, Nature Photonics, 2009, 3, 591.
- [19] K. Watanabe, T. Taniguchi, Int. J. Appl. Ceram. Technol 2011, 8, 977.
- [20] K. Watanabe, T. Taniguchi, T. Kuroda, H. Kanda, Appl. Phys. Lett. 2006, 89, 141902.
- [21] Y. Toyozawa, Elementary processes in luminescence. J. of Lumin. 1976, 13, 12.
- [22] Y. Kubota, K. Watanabe, O. Tsuda, T. Taniguchi, SCIENCE, 2007, 317, 932.
- [23] C. Attacalite, L. Wirtz, A. Marini, A. Rubio, Scientific Reports, 2013, 3, 2698.
- [24] S. Majety, X. K. Cao, R. Dahal, B. N. Pantha, J. Li, J. Y. Lin, H. X. Jiang, Quantum Sensing and Nanophotonic Devices IX, 2012, 82682R.
- [25] Muhammad Sajjad, Wojciech M. Jadwisienczak, and Peter Feng, “Nanoscale Structure Study of Boron Nitride Nanosheets and Development of Deep-UV Photo-Detector” Nanoscale; 6, (2014) 4577, DOI: 10.1039/C3NR05817D.



- [26] Feng, P. X.; Zhang, H. X.; Peng, X. Y.; Sajjad, M.; Chu, J. Review of Scientific Instruments 2011, 82, 043303.
- [27] Peng, X. Y.; Sajjad, M.; Chu, J.; Yang, B. Q.; Feng, P. X. Applied Surface Science 2011, 257, 4795.
- [28] Sugino, T.; Kimura, C.; Yamamoto, T. Appl. Phys. Lett. 2002, 80, 3602-3604.
- [29] Chen, Z. G.; Zou, J. J. Mater. Chem. 2011, 21, 1191-1195.
- [30] Gomer, R. Field Emission and Field Ionization. American Vacuum Society Classics, Woodbury/AIP, New York, 1993, 19.
- [31] Fowler, R. H.; Nordheim, L. W. Proc. R. Soc. London, Ser. A 1928, 119, 173.
- [32] Varshney, D.; Rao, C. V.; Guinel, M. J. F.; Ishikawa, Y.; Weiner, B. R.; Morell, G. Journal of Applied Physics 2011, 110, 044324-1—044324-6.
- [33] Chen, H.; Zhang, H.; Fu, L.; Chen, Y.; Williams, J. S.; Yu, C.; Yu, D. Appl. Phys. Lett. 2008, 92, 243105-243108.
- [34] Wang, S. G.; Wang, J. J.; Miraldo, P.; Zho, M. Y.; Outlaw, R.; Hou, K.; Zhao, X.; Holloway, B. C.; Manos, D.; Tyler, T.; Shenderova, O.; Ray, M.; Dalton, J.; Mcguire, G.; Appl. Phys. Lett. 2006, 89, 183103-183106.
- [35] Hou, K.; Outlaw, R. A.; Wang, S.; Zhu, M.; Quinlin, R. A.; Manos, D. M.; Kordesch, M. E.; Arp, U.; Holloway, B. C. Appl. Phys. Lett. 2008, 92, 133112-133115.
- [36] Eda, G.; Unalan, H. E.; Rupesinghe, N.; Amaratunga, G. A. J.; Chhowalla, M. Appl. Phys. Lett. 2008, 93, 233502-233504.

## Chapter 6

### Other Research Developed in this Thesis

In this thesis, we also study BN hard phase e.g. c-BN films similar to diamond like carbon film as in the case of carbon material. We introduced a simple approach to synthesize c-BN films at significantly low substrate temperature down to 450 °C using ferrous oxide ( $\text{Fe}_2\text{O}_3$ ) nanoparticles as catalyst. The catalyst helped to create reactive species of BN and transform the initially grown h-BN base layer into c-BN film.

Besides c-BN films, growth of low dimensional boron nitride nanostructure e.g. synthesis of BN nanowires, BNNTs and nanorods is demonstrated at different experimental conditions. To nucleate BN nanostructures, a short pulse laser plasma deposition technique has been applied.

The surface morphology of each film and nanostructures was analyzed with SEM and TEM microscope. Raman spectroscopy FT-IR and XRD techniques were used to analyze the crystalline structures of the samples. Evolutions of the vibrational modes of transverse optical and longitudinal optical phonons were observed. EDS spectroscopy investigations verified the dominance of B and N in the samples.

#### 6.1 Introduction

The synthesis of c-BN films has attracted extensive research interest due to their excellent physical and chemical properties, which are expected to be similar or superior to those of diamond films. Moreover, the unusual combinations of thermal, electrical and optical properties, as well as hardness, low thermal expansion, microwave transparency of c-BN make it a promising material for wide applications [1-5]. In general, c-BN films can be obtained from h-BN at high temperature 1200-2000 °C and pressure 2.5-7.5 GPa. For example, Endo et al. [6]

synthesized c-BN by  $\text{Ca}_3\text{B}_2\text{N}_4$  pyrolysis at 4.4-6.5 GPa and 1180-1800 °C. Hirano et al. [7] prepared c-BN at 1800 °C and 6.5 GPa. Yu et al. [8] synthesized BN nanotubes by means of excimer laser ablation at 1200 °C, whereas, Han et al. [9] nucleated BN nanotubes by substitution reaction from carbon nanotubes at 1500 °C. So far, there are few reports concerning the growth of c-BN at low substrate temperature.

We believe that low-dimensional systems interesting and worth pursuing as evidenced by the growth of carbon, silicon etc. nanostructures. Synthesis of BN nanowires, nanorods and nanotubes is also one example of 1D nanostructure. BN nanostructures have attracted great interest in material technology due to their applications and numerous properties i.e. good thermal conductivity, high hardness, low thermal expansion, high electrical resistance, microwave transparency, good thermal shock resistance, and chemically inertness [10-14]. There is a significant interest in the synthesis of nanostructured BN including nanowires, nanorods and nanotubes for nano materials research.

## **6.2 Preparation of Catalyst for the Synthesis of c-BN Films**

Syntheses of c-BN films are highly dependent on deposition conditions. With assistance of catalyst, laser plasma deposition normally yields differently crinkled films. The wrinkled structures or bend phenomenon could also possibly be caused by the residual stresses generated during the growth process. This phenomenon would become more evident if the higher temperature is set during the synthesis. However, to avoid such problems, in present thesis, we used catalyst support in the synthesis of c-BN films.

$\text{Fe}_2\text{O}_3$  nanoparticles are used as catalyst for the synthesis of c-BN films at significantly low temperature. The catalytic solution was prepared with 70 Wt. % acetone and 30 Wt. %  $\text{Fe}_2\text{O}_3$  nano-powders. Three polycrystalline silicon wafers ( $\text{S}_1$ ,  $\text{S}_2$  and  $\text{S}_3$ ) used as substrates were

individually prepared: S<sub>1</sub> with 1 drop, S<sub>2</sub> with 2 drops and S<sub>3</sub> with 3 drops of catalyst. Prior to the deposition, each substrate mounted onto the spin coating machine for the uniform deposition of catalyst layer.

### **6.3 Experimental Conditions**

A CO<sub>2</sub> pulsed laser deposition technique (CO<sub>2</sub>-PLD: wavelength: 10.6  $\mu\text{m}$ , pulse width: 1~5  $\mu\text{s}$ , repetition rate: 5 Hz, and pulse energy: 5 J, power density:  $2 \times 10^9 \text{ W/cm}^2$  per pulse) was used to irradiate a commercial pyrolytic hexagonal boron nitride target (2.00" diameter  $\times$  0.125" thick, 99.99% purity, B/N ratio  $\sim$  1.05, density  $\sim$  1.94 g/cc) [15-16]. The pressure in the deposition chamber was kept at  $2.66 \times 10^{-3}$  Pa. A set of substrates (S<sub>1</sub>, S<sub>2</sub> and S<sub>3</sub>) was placed together onto the substrate holder 3 cm away from the target. The laser beam was focused onto the target with an incident angle of 45 degrees relative to the target surface. A heater and a thermocouple were used to obtain and monitor the desired substrate temperature (450 °C). The duration for deposition was 10 minutes.

### **6.4 Low temperature synthesis of c-BN films**

#### **6.4.1 SEM and TEM Results**

SEM cross-sectional views of the films deposited onto substrates (S<sub>1</sub>, S<sub>2</sub>, and S<sub>3</sub>) are shown in Fig. 6.1(a-c). The thicknesses of the films on S<sub>1</sub>, S<sub>2</sub> and S<sub>3</sub> substrates were around 0.25  $\mu\text{m}$ , 0.85  $\mu\text{m}$  and 1.67  $\mu\text{m}$ , respectively. A considerable increase in the thicknesses of the films probably indicates that the high amount of catalyst would help to the formation of more BN layers. The experiments without using catalyst were also conducted. However, the observed properties of the film i.e. thickness, surface morphology and crystalline structure were similar to that of the sample prepared on S<sub>1</sub> substrate. This indicates that without catalyst or little amount of catalyst does not enhance film's properties.

Figure 6.1(d-f) shows plane-view SEM images of c-BN films. The morphology of the film on  $S_1$  substrate showed spontaneous nucleation of BN layers as indicated with the arrows in Fig. 6.1(d). The top layer of the film appeared smooth and flat. Few spherical particles were visible underneath the layers representing the transparency of the film for electron beam. These particles are probably related to the catalyst. The morphology of the film prepared on  $S_2$  substrate also showed the layer growth characteristics even though the surface was not flat (Fig. 6.1(e)). Further changes in the appearance and morphology of the film were recorded on  $S_3$  substrate (Fig. 6.1(f)). The film shows highly transparent glass-like appearance in which layers can be seen inside the sample. This indicated that with an increase of the amount of catalyst, more layers might be formed onto the substrate surface. The general interpretation is that during laser ablation of the target, high energy ions and clusters were formed which played an important role in surface heating of the substrate during the deposition of BN films. When BN ions and clusters came close to the substrate surface, the extra thermal activation besides the substrate heating was provided to the catalyst particles that reacted strongly with the incoming BN species and exchanged energy through collisions. This enhanced the creation small size crystallites that combined to form a well-shaped BN film [17]. Meanwhile, due to surface heating of the substrate, thermal vibrations enhanced the migration of the catalyst particles onto the surface of the initially grown layer. These catalyst particles supported the growth of next BN layer and so on. This is in agreement with the previous reports [18-23].

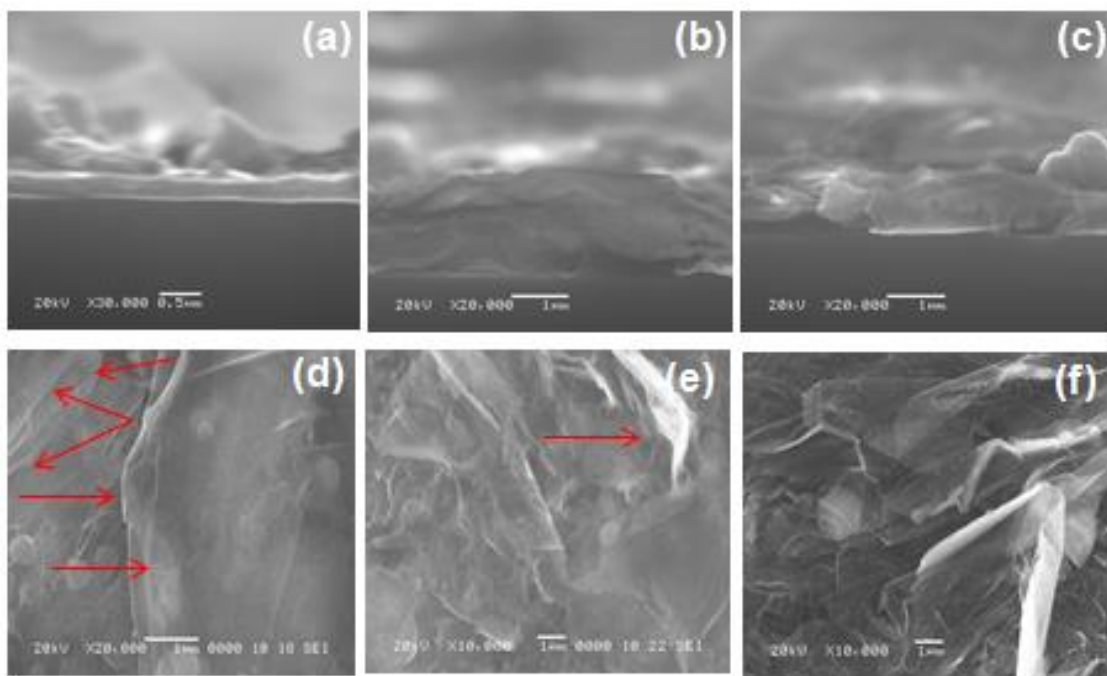


**Figure 6.1** c-BN films synthesized on  $S_1$ ,  $S_2$  and  $S_3$  substrate; (a-c) SEM cross sectional view, (d-f) top view SEM micrographs. The scalar bars are shown on the images.

#### 6.4.2 Raman, XRD and FT-IR Spectroscopy of *c*-BN Films

Figure 6.2 (a-c) shows typical Raman spectra of BN films. Two peaks were identified in the spectrum (Fig. 6.2 (a)) of the sample from  $S_1$  substrate. The broad spectral line centered at  $962\text{ cm}^{-1}$  is related to silicon vibration band and the intense peak at  $1365\text{ cm}^{-1}$  is assigned to B-N high frequency vibrational mode ( $E_{2g}$ ) within the h-BN layer. A tiny peak at  $1300\text{ cm}^{-1}$  related to longitudinal (LO) vibrational mode of c-BN can also be observed. This indicated that in the present case, h-BN phase was dominating in the film. The spectrum (Fig. 6.2(b)) corresponding to  $S_2$  substrate shows transverse optical (TO) and Longitudinal optical vibrational modes of c-BN at  $1065\text{ cm}^{-1}$  and  $1300\text{ cm}^{-1}$ , respectively. However, the vibrational mode related to h-BN was not observed. Similarly, TO and LO vibrational modes of c-BN films also appeared in the spectrum (Fig. 2.6 (c)) of the sample from  $S_3$  substrate. This experimental data suggested that

catalyst particles provided sufficient energy of exchange through collisions that transformed initially grown h-BN phase into c-BN phase. A tentative interpretation is that the extra collisions and heating would enhance the mobility of the catalyst particles on the surface of the substrate, and correspondingly the internal stress/strain built up that accelerated/catalyzed the transformation of  $sp^2$ -bonded h-BN base layer to  $sp^3$ -bonded c-BN film [24]. XRD spectra of the films are shown in Fig. 2.6 (d-f). A peak at  $2\theta \sim 26^\circ$  assigned to h-BN (002) phase was recorded from the sample synthesized on S<sub>1</sub> substrate (Fig. 2.6 (d)). No other phase was detected which indicates that the film composed of hexagonal structure. XRD pattern (Fig. 2.6 (e)) of the film prepared on S<sub>2</sub> substrate shows the peaks at  $2\theta = 44^\circ, 49^\circ$  correspond to c-BN (111) and (200) phases, respectively [25]. In contrast, intensity of the peak related to h-BN (002) phase reduced and a new peak appeared at  $2\theta \sim 39^\circ$  related to h-BN (001) phase. In the XRD pattern (Fig. 2.6 (f)) of the film from S<sub>3</sub> substrate, h-BN (002) peak completely vanished, whereas c-BN (111) and c-BN (200) phases became dominant, indicating the improvement of the crystallinity of c-BN phase. Some peaks marked with asterisk were also recorded in the XRD spectra but have not yet been identified. The phases in the films were also analyzed with FTIR spectra as shown in Fig. 2.6 (g-i). The  $sp^2$ -bonded h-BN is characterized in the sample prepared on S<sub>1</sub> substrate by two vibrational modes, one at  $1365\text{ cm}^{-1}$  for in-plane B-N stretching and other at  $805\text{ cm}^{-1}$  for the out of plane B-N-B bending [26] as shown in Fig. 2.6 (g). A tiny peak at  $1063\text{ cm}^{-1}$  related to  $sp^3$ -bonded c-BN peak was also observed. However, c-BN peak can be easily identified in the spectrum of the sample from S<sub>2</sub> substrate, whereas h-BN stretching mode was comparatively weak (Fig. 2.6 (h)). A significant increase in the intensity of c-BN peak was seen in the sample from S<sub>3</sub> substrate (Fig. 2.6 (i)), probably indicating that at high amount of catalyst, the sample has more c-BN content.

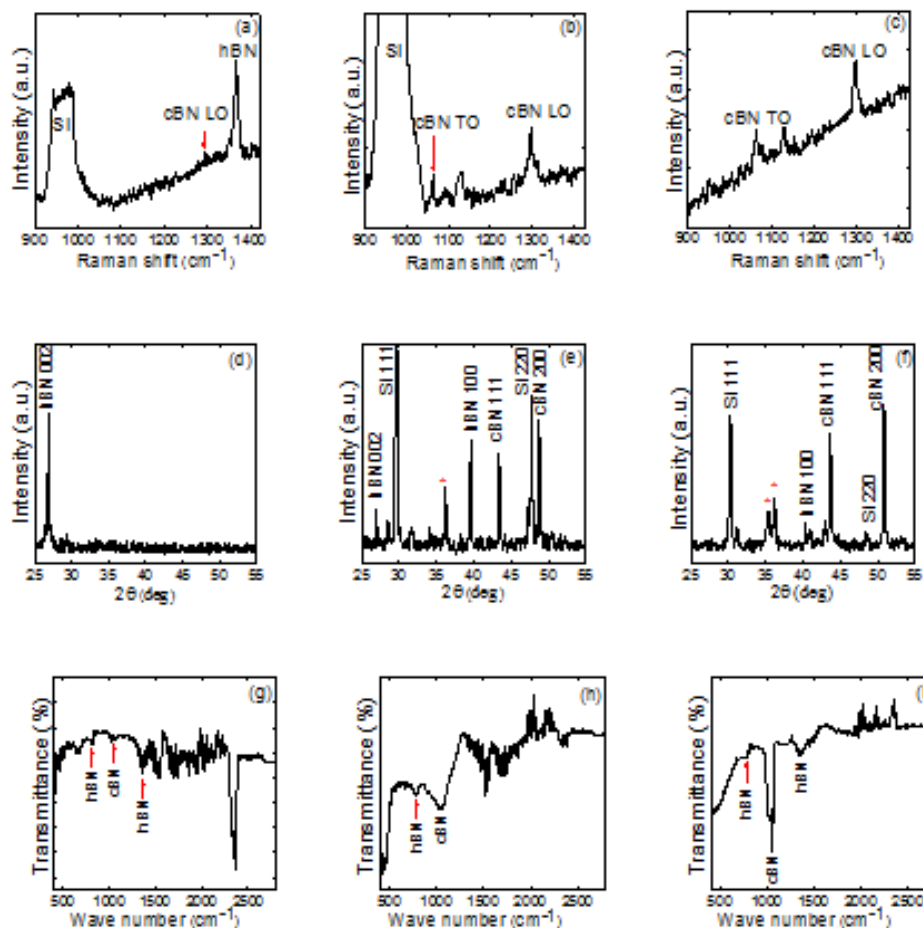


**Figure 6.2** (a-c) Raman spectra (d-f) X-Ray diffraction patterns and (g-i) FTIR spectra of c-BN films synthesized on  $S_1$ ,  $S_2$  and  $S_3$  substrates, respectively.

### 6.4.3 Elemental Analysis in c-BN Films

Typical result of EDS analysis of the sample from  $S_3$  substrate is presented in Fig. 6.3. The film mainly composed of B and N species. A small amount (total less than 10%) of other elements such as O and Fe were also identified that should be from the catalyst ( $Fe_2O_3$ ).



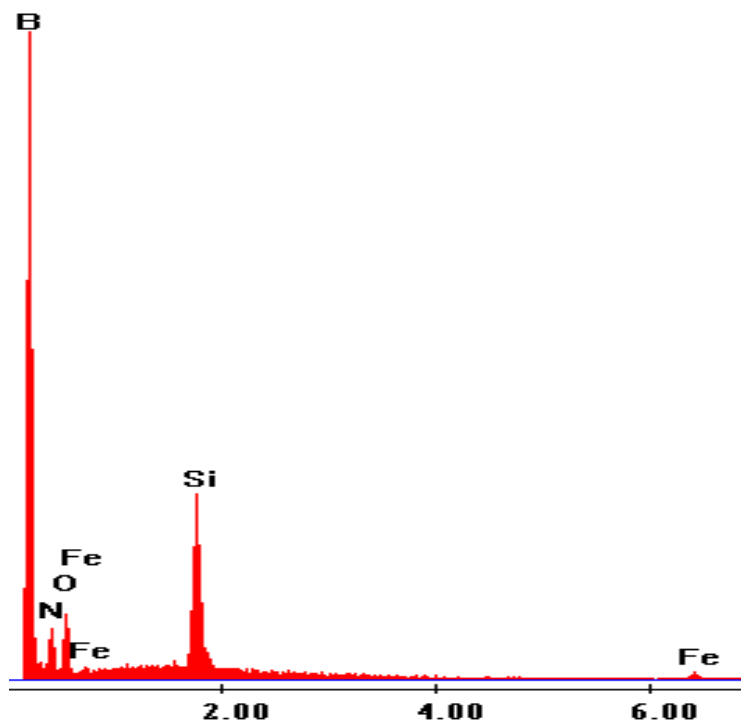


**Figure 6.3** EDS spectrum of c-BN film prepared on  $S_3$  substrate.

## 6.5 Synthesis Techniques for 1D Nanostructures

Several types of techniques were used to synthesize 1D BN nanostructures i.e. ion assisted physical vapor deposition (IVD) [27], arc jet or sputtering deposition and PLD technique etc. However, BN nanostructure prepared with other technique like CVD is poor due to the concentration of impurities, like H, Ar and O, depending on the deposition conditions applied. The metallic impurities, like tungsten (from filament) and ferrous (sputtering from stainless steel) are common in BN films [28]. These impurities may create structural disordering and effect the functioning of devices fabricated for electronics application. Some other possible effects i.e. shadowing at glancing angle of incidence, re-deposition of sputtering atoms and sputter effects of reflected ions have considerable attentions during the development of

nanostructures [29,30]. However, these physical phenomenon have minor effects in our present case of synthesis of nanostructures via laser ablation of solid target.

## **6.6 Experimental Conditions Applied**

For the synthesis of BN nanorods, short pulse laser plasma deposition technique is applied. An ArF Lambda Physics 1000 excimer laser (193nm, ~20ns, and 10 Hz repetition rate, and 200 mJ pulse energy) was used to irradiate BN target at  $2.0 \times 10^{-5}$  Torr in the chamber. The laser beam, focused with a 30 cm focal length fused silica lens, with incident at  $45^\circ$  relative to the target surface. The diameter of the focused spot of laser beam on the BN target was about 3 mm. The power density of the laser on the target was  $1.4 \times 10^8$  W/cm<sup>2</sup> per pulse. For smooth deposition, target was rotated with 200 rpm. Commercial Si and Mo materials were chosen as substrates because of their numerous electronic properties and extensive use in fabricating microelectronic devices. The substrates were placed at 3 cm away from the target. Substrates were heated to 550 °C and 650 °C. A thermo-couple was used to measure the temperature during deposition process. The error in temperature was around 10%. The description of operating mechanism and system is detailed elsewhere [31].

Prior to deposition, substrates were polished with diamond powder (diameter: <10nm), cleaned with acetone and methanol, and then rinsed with deionized water in sequence to remove impurities. The Si substrates were that were directly used after cleaning. The duration for each deposition was kept 20 minutes.

## **6.7 Nanostructures Characterizations**

Surface morphology of BN Nanostructures were characterized by using SEM microscopy whereas, crystalline structure and elemental analysis study was conducted using Raman spectroscopy, XRD analysis and EDX spectroscopy.

### 6.7.1 BN Nanowires

The synthesis of BN nanowires was composed on Si substrate and results are presented in Fig. 6.4. Figure 6.4a shows SEM images of 1D BN nanowires synthesized on Si substrates at 550 °C and 650 °C, respectively. We observed plenty of nanowires emerging out from a thick BN clusters as shown in Fig. 6.4 (a). The diameter of each nanowire was around 0.1  $\mu\text{m}$  with lengths around 2~5  $\mu\text{m}$ . The micro size of clusters present on the substrates surface (Fig. 6.4 (a)) were probably ejected from the target due to laser heating surface above the melting point with the subsequent fusion of the surface. Such effect was also observed in the earlier studies [13] using variety of the materials deposited by the laser ablation. In general the micro-clusters do not have enough thermal energy to be transformed into well-defined nanowires. Therefore, a high substrate temperature during deposition is related to yield well-defined nanowires. Fig. 6.4 (b) shows the surface morphology of BN sample prepared on Si substrate at 650 °C when other experimental parameters were kept unchanged. The enlarged one-dimensional fine tip nanowires were found on the substrate surface. The length of nanowire was around 100  $\mu\text{m}$ , whereas, the diameter of the nano-tips was around 50 nanometers. It was also observed that a single nanowire has two fine nanotips. Such kind of nanowires particularly, nanotips can be more sensitive for field emission applications. However, increasing the substrate temperature did not lead to better nanowires growth. Probably nitrogen atoms desorbed as nitrogen molecules ( $\text{N}_2$ ) from the substrate easily at high temperature [32]. This may cause problems in obtaining active N atoms to form BN nanostructure as well. This showed that an optimum substrate temperature was required to obtain high quality crystalline nanowires.

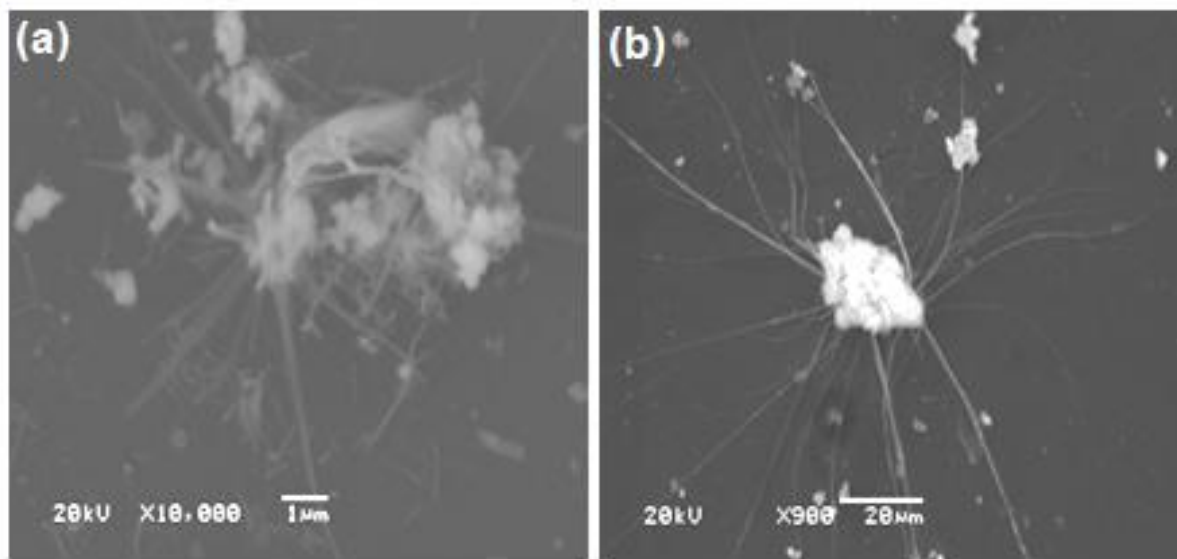


**Figure 6.4** SEM micrographs of BN nanowires synthesized on Si substrates (a) at 550 °C (b) at 650 °C. The scale bars are shown as 1 μm for deposition at 550 °C and 20 μm for the deposition at 650 °C substrate temperatures.

### 6.7.2 BN Nanorods

Following the same experimental parameters and steps, a new experiment was conducted on a Mo substrate in order to compare the nucleation of BN samples on silicon versus molybdenum substrates. Fig. 6.5 (a) shows the SEM micrograph of BN nanorods on Mo substrate at 550 °C. The micrograph revealed an island of boron nitride nanorods. The diameter of nanorods was around 0.2 μm. However, different nanorods have different lengths varying from 0.2 μm to 0.8 μm respectively. In contrast, the sample prepared at 650 °C has flower like nanostructure based on nanorods (Fig. 6.5 (b)). The nanorods were embedded uniformly on to the surface of substrate around the BN cluster. The micrograph revealed that a thick cluster was formed in the middle with large number of nanorods emerging all around from its base. Probably, the base of the cluster was in contact with the substrate and was at a high temperature compared to the top and middle part of it. Due to high temperature, first the cluster base was

broken and transformed into nanorods. However, the central part of the cluster did not get the required amount of heat in order to transform into desired nanorods.

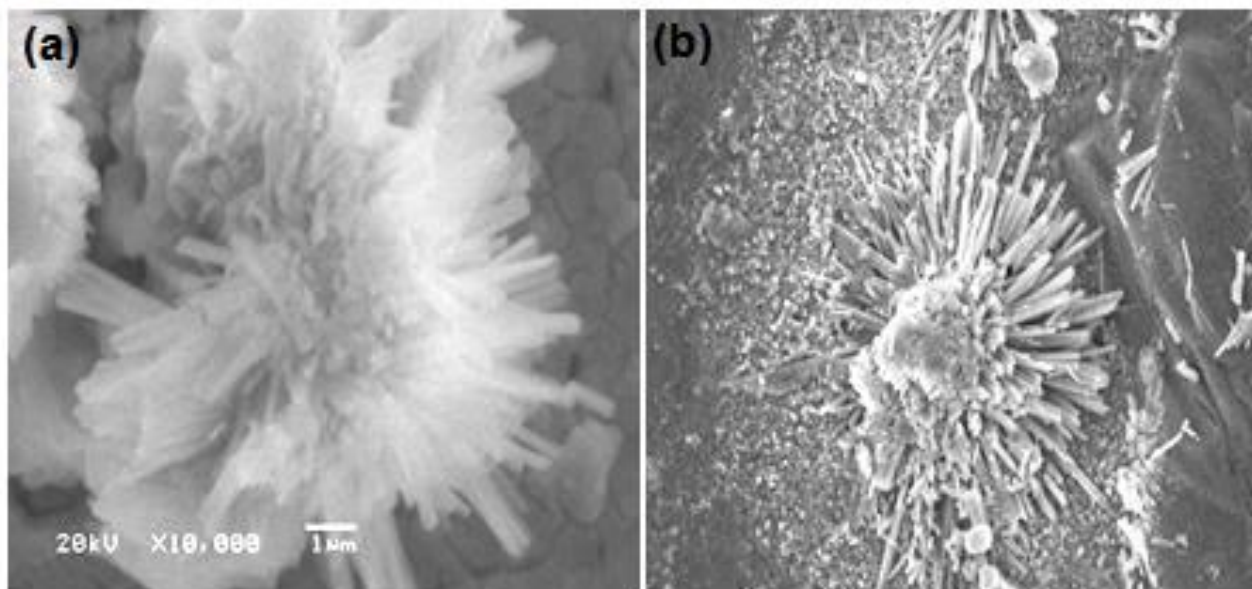


**Figure 6.5** SEM micrographs of BN nanorods synthesized on Mo substrates (a) at 550 °C and (b) at 650 °C. The scale bars are shown as 1  $\mu\text{m}$  for deposition at 550 °C and 20  $\mu\text{m}$  for the deposition at 650 °C substrate temperatures.

### 6.7.3 BNNTs

In our earlier experiments, we synthesized BN nanowires and nanorods without using catalyst. However, we were not able to synthesize BNNTs via PLD system without the support of catalyst. Therefore, in the present experiment, we used Ni nanopowder as catalyst and synthesized BN nanotubes.

Figure 6.6a shows the SEM images of BNNTs randomly distributed on entire surface of the substrate. In the magnified image (Fig. 6.6 (b)), one can clearly find out the nanotubes bending and scrolling. The diameter of each nanotube was around 0.5  $\mu\text{m}$  indicating multiwall nanotubes, however at this stage the length of a single nanotube wasn't estimated as the tubes have bending and scrolling geometry. Fig. 6.6(c) shows corresponding TEM images of bunch of

BNNTs. In the magnified TEM image of a single BNNT (Fig. 6.6 (d)), we observed hole indicated typical geometry of multiwall BNNT.

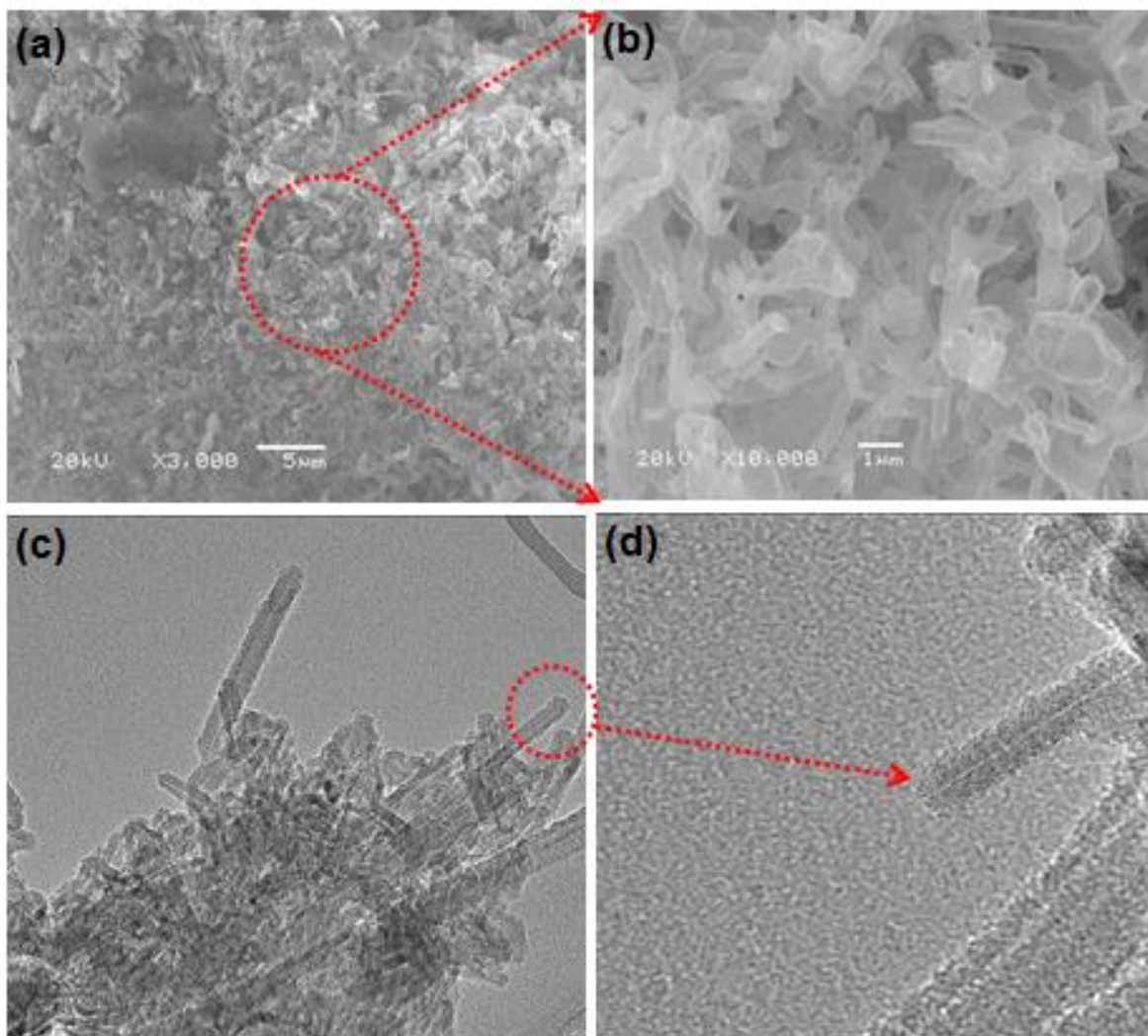


**Figure 6.6** (a) SEM images of BN nanotubes synthesized on Si substrate at 300 °C substrate temperatures, (b) magnified SEM image of BNNTs. (c,d) corresponding TEM and magnified TEM images of BNNTs.

## 6.8 Effect of Experimental Parameters in the Synthesis of BN Nanostructures

### 6.8.1 Effect of Substrate Temperature

Substrate temperature has significant effect in the synthesis of BN nanostructures. Following SEM images are one typical example. Fig. 6.7 shows SEM images of boron nitride

nanorods prepared on Mo substrates at different temperatures 400 °C, 500 °C, and 600 °C, respectively. In Fig. 6.7 (a), no obvious nanostructure was observed as the synthesis temperature was 400 °C. Fig. 6.7 (b) shows the SEM micrograph of nanorods prepared at 500 °C. Large numbers of randomly oriented nanorods were found. The length of these nanorods varies from 450 nm to 1.5 µm but their diameters were very similar, around 100 nm. After making comparison between Fig. 6.7 (a) and (b), we concluded that an increase of the substrate temperature might be helpful to yield better nanostructure. Therefore, experiment at 600 °C was conducted keeping other experimental parameters unchanged. The SEM image of the sample prepared is shown in Fig. 6.7 (c), where we found that BN nanorods become wider compared to that of grown at 500 °C substrate temperatures (Fig. 6.7 (b)). The diameter and length of the nanorods was recorded different from each other. However, the length varied from 1 µm to 4 µm approximately and diameter was around 0.1 µm to 0.6 µm respectively. The interesting point to be noticed not only the size of the nanorods but transparency was also increased at higher deposition temperature indicated that temperature plays important role in the crystallinity of the samples. These variations of nanostructures, as shown in Fig. 6.7, were obviously related with the thermal energy provided by the substrate to the sample during deposition process. The general interpretation was that during laser producing plasma of the target, high energy ions and clusters of BN were formed which play an important role of surface heating as well as etching during the deposition process. The ions, when they reach to the substrate surface, the extra thermal activation besides the substrate heating was provided to the sample by energy exchange through collisions between the active ions, clusters and atoms of BN. This helped to transform small sized nanorods. The incoming ions attach with the initially grown nanorod and hence well-shaped wide and large transparent nanorods appear.

It should be mentioned here that shadowing at glancing angle also play an effective role in growing nanostructures [33]. Such technique is capable of fabricating ordered arrays of nanostructures i.e. nanorods. It utilizes the flow of atoms or molecules and clusters impinging from surface of the target on to the substrate from an oblique angle in a vacuum which results in a deposited nanostructure showing nanorods morphology [34]. In the case of laser ablation of solid target, the angle of incidence of the laser beam on to the target controls the tilt of the column (plasma plume) and affects the degree of shadowing and hence the morphology and orientation of the deposited nanorods. However, in the present case, shadowing at glancing angle of incidence is less effective. The reason is this that we placed target and substrates parallel to each other. The plasma plume generated by laser pulses was perpendicular on the target surface as well to the surface of the substrates which minimizes the shadowing effects.

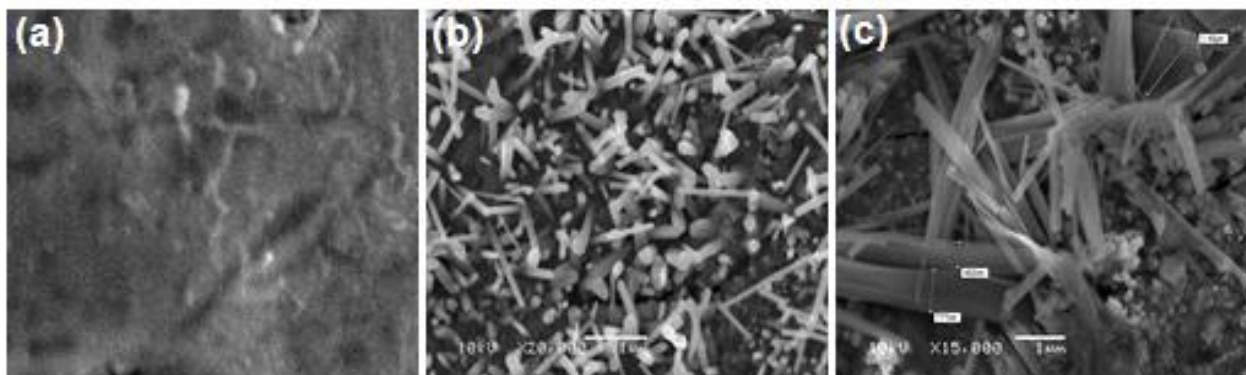


**Figure 6.7** SEM micrograph of BN nanostructure on Mo substrate at (a) 400 °C and (b) at 500 °C and (c) at 600 °C. The scale bars are 1  $\mu$ m.

### 6.8.2 Substrate Material Effect

Substrate material is another parameter that could affect the growth process and morphology of synthesized BN nanostructures. This we have studied by depositing BN nanostructures on two different substrates Si and Mo. The variation of nanostructure is related to



the strain from the misfit in lattices between boron nitrogen films and the substrate, which leads to structure transitions [35,36].

The misfit in lattices between initially grown films and substrate can be enhanced with increase in substrate temperature. The over-layers grow with stacking fault after a first coherent layer. When the film was much thicker than the critical thickness, the initial smooth surface of the film would become the fractal like structure, then enhanced, and eventually the thin film will be transformed into rod-shape structure.

## **6.9 Other Characterizations**

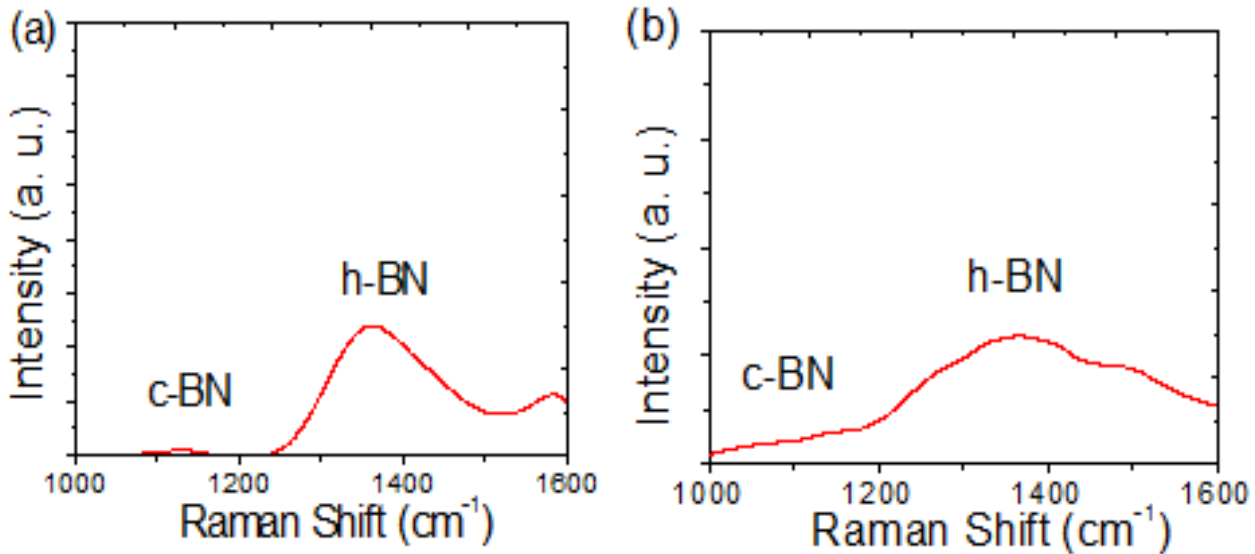
Besides scanning electron microscopy, we applied energy dispersive X-Ray spectroscopy (EDS) to analyze boron and nitrogen concentration in the samples. The crystal structures of BN samples were investigated using Raman spectroscopy and x-ray diffraction technique. The experimental results showed that the nanorods were hexagonal mixed with cubic, whereas the nanowires and nanotubes were hexagonal.

### **6.9.1 Raman Spectroscopy of BN Nanorods**

Raman spectroscopy is a powerful technique to analyze  $sp^2$  and  $sp^3$  bonding structures. Therefore, in our current study, the crystalline structures of BN nanorods were analyzed by Raman spectroscopy using triple monochromator (ISA J-Y Model T64000) with an excitation wavelength of 514 nm ( $Ar^+$  ion Laser). The microscope was used for focusing the laser beam onto the surface of samples. Fig. 6.8 (a) shows Raman spectrum of the BN film deposited at 400 °C. Two peaks at  $1054\text{ cm}^{-1}$  and at  $1358\text{ cm}^{-1}$  can be observed. The first peak is very weak that is assigned to vibrational mode of  $sp^3$  bonding related to c-BN phase. The second peak at  $1358\text{ cm}^{-1}$  is due to  $sp^2$  vibrational mode that represents h-BN phase. The results from the Raman characterization indicate that  $sp^2$  bond dominates inside the sample prepared at low substrate

temperature. Furthermore, crystalline structure is poor because the peak profile is extremely broad.

Figure 6.8 (b) and (c) show Raman spectra of BN nanostructures synthesized at 500 °C and 600 °C, respectively. From 500 °C to 600 °C, Raman peaks nearly remained unchanged but becomes much sharper whereas peak broadening is also reduced at 600 °C. Therefore, it may be concluded that crystal quality of BN nanorods possibly improved with the increase of substrate temperature. A tentative interpretation is that internal stress and thermal vibrations in nanostructure increases at higher temperature, resulting in partially transforming the sample into c-BN phase. It is found that the peak corresponding to h-BN exists in all Raman spectra. This may be due to the fact that Raman scattering efficiency for h-BN is much higher than that for c-BN [37]. The significant finding is that the influence of substrate temperature caused an increase of  $sp^3$  content in the sample that is in good agreement with the previous report [38].



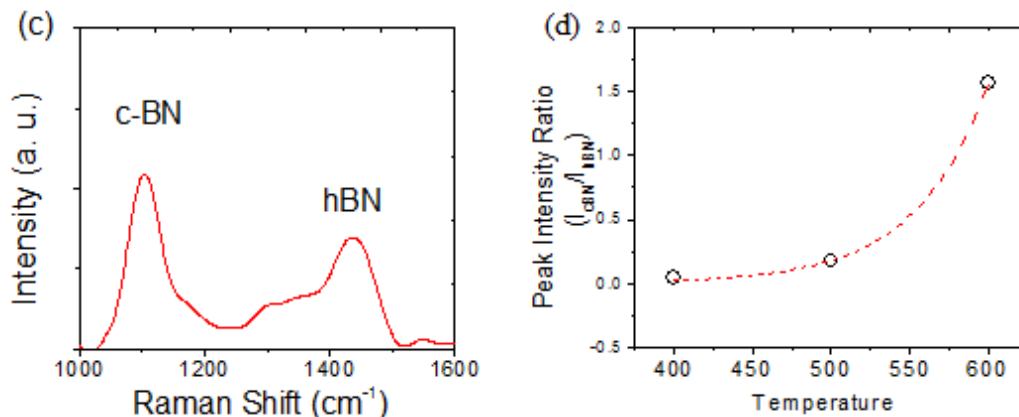


**Figure 6.8** Raman spectroscopy of BN nanostructure at (a) 400 °C, (b) 500 °C, and (c) 600 °C, respectively. (d) The peak intensity ratio ( $I_{\text{cBN}}/I_{\text{hBN}}$ ) as a function of substrate temperature.

Raman peak shifting and broadening of BN sample, from  $1362 \text{ cm}^{-1}$  to  $1432 \text{ cm}^{-1}$  for h-BN phase and from  $1065 \text{ cm}^{-1}$  to  $1103 \text{ cm}^{-1}$  in the case of c-BN phase is also observed as shown in Fig. 6.8 (c). In particular for c-BN, it is a so-called reststrahlen band and has an intrinsic broadness [39].

However, the shift in the Raman peaks towards higher number (as shown in Fig. 6.8c) is due to small amount of impurities or because of crystalline disorder. Fig. 6.8 (d) shows the fraction of peak intensity ratio ( $I_{\text{cBN}}/I_{\text{hBN}}$ ) as a function of substrate temperature. The ratios ( $I_{\text{cBN}}/I_{\text{hBN}}$ ) from the samples increased with substrate temperatures from 400 °C to 600 °C. At 600 °C, c-BN phase already dominates the sample.

It is well known that re-deposition of the sputtered material is also an important issue of manufacturing of nanoscale structures. In most of the cases re-deposition of the sputtered material is seen as a contamination with unwanted species [35]. In our case i.e. laser ablation of solid target, sputtering took place very less and hence the re-deposition. The evidence was that the impurities were low in the samples as detailed in the EDS.

From literature [38], BN phase change could occur only at higher substrate temperature. Thus the temperature threshold is a fundamental condition for post-nucleation of c-BN. This threshold must be related to the initial h-BN growth stage or the onset of the nucleation process of the c-BN phase.

### 6.9.2 XRD Analysis

The crystallographic structures of the selected BN samples were also examined using XRD technique. No obvious XRD spectral lines were observed from the sample prepared at 400 °C. This result is in agreement with the data recorded from Raman characterization, indicating low temperature of deposition yields amorphous BN thin film. In contrast, high temperature of deposition yields much better quality of crystalline structures that have been confirmed by XRD shown in Fig. 6.9. The peak observed at 26° is due to h-BN phase, whereas the peak centered at 40.7° is of Mo substrate. A XRD peak marked at 29° (Fig. 6.9 (a)) was related to substrate and another peak located at 37° (in Fig. 6.9 (b)) was also observed that may be from impurity contribution. These impurities may belong to chamber or substrate holder as explained in EDS spectra.

XRD pattern in Fig. 6.9 (a) also shows the peak at 44° has relatively very low diffraction intensity, suggesting less content of c-BN (111) phase inside the sample. The peak position for c-BN (111) phase is as well reported in literature [40]. The XRD results of the sample prepared at 600 °C are shown in Fig. 6.9 (b). The peak appeared at 26° vanishes whereas the signal of the peak at 44° becomes much stronger. The changes of XRD signals reveal that  $sp^3$  content is increasing with substrate temperature. The XRD intensity ratios between c-BN peak at 44° and h-BN peak at 26° increased from 0.19 (Fig. 6.9(a)) to 23.94 (Fig. 6.9 (b)), indicating the

evolution of the crystalline structure from h-BN to c-BN domination inside the sample following an increase of substrate temperature.

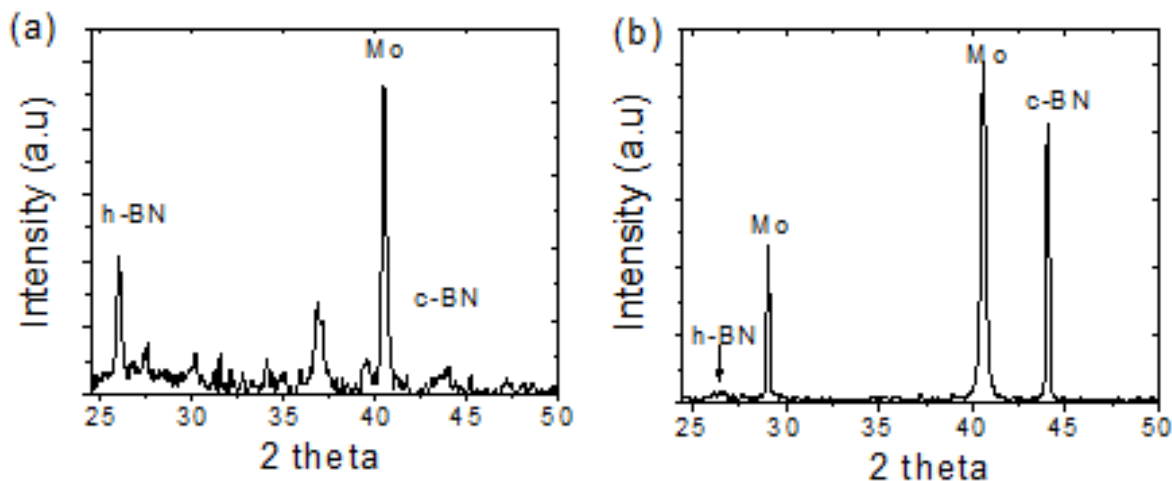


**Figure 6.9** X-Ray diffraction pattern of BN nanostructure on Mo substrate (a) at 500 °C (b) at 600 °C.

Some interpretation related with sputter effects of reflected BN ions can also affect the crystalline structures of nanorods. However, in laser ablation technique, such effects have minor contributions in distorting the structure of BN samples. The effects of reflected ions took part in growth mechanism of nanostructures as explained in the case of glancing angle of incidence. In general, reflected ions affect surface roughness, morphology of the nanorods, and their structure evolution if the energy of the scattered ions is more than 200 eV [41]. The ions that reflect from normal incidence of the substrates were very low in energy, might be even less than 5 % of incidence ions energy. Hence, in present case of laser ablation technique, low energy reflected ions do not affect the crystalline structure by much.

### 6.9.3 EDS Spectroscopy

EDS technique was used for elemental analysis of BN samples and it was observed that the atomic ratio of the B and N in nanorods strongly relies on substrate temperatures. For

example at 500 °C, atomic concentrations of boron and nitrogen were 74.93 At% and 12.10 At%, respectively. At 600 °C, it became 78.12 At% for boron and 19.29 At% for nitrogen. Since, surface of the samples were B-rich BN, high content of boron in EDS spectra were obtained. The increase in atomic percentage also showed that boron and nitrogen species became more reactive at high temperature. Few percentage of impurity elements i.e. 0.34 At% oxygen and 2.24 At% carbon was also found in nanostructured BN samples. Weak oxygen signal from EDS spectra was probably due to oxygen contamination when transferring the sample in air from the deposition chamber to characterization chamber and carbon contamination was possible from deposition chamber via scattered laser pulses.

#### **6.10 Conclusion**

In summary, c-BN films were synthesized using catalyst at low substrate temperature down to 450 °C. A large amount of the catalyst helped producing thick BN films. From XRD data, it was concluded that the hexagonal structure dominates in the sample prepared with a small amount of catalyst, whereas cubic phase dominated in the case of a large amount of the catalyst. Both FTIR and Raman spectra confirm the results obtained from XRD measurements.

The BN nanostructures were also synthesized and it was concluded that the morphology and dimensions of nanostructures change with the change in substrate temperatures. At 500 °C, large numbers of randomly oriented nanorods were found. The length of these nanorods varies from 450 nm to 1.5 µm. At 600 °C, the BN nanorods become wider. Both Raman spectra and X-ray diffraction spectra show that the content of h-BN phase decreases with an increase of substrate temperature, whereas content of c-BN increases. Moreover, BN nanorods transform into crystalline phases at higher substrate temperature.

## 6.11 References

- [1] Y.H. Xiong, C.S. Xiong, S.Q. Wei, et.al., *Applied Surface Science*, 253 (2006) 2515-2521.
- [2] E. Knittle, R.M. Wentzcovitch, R. Jeanloz, et.al., *Nature* 337 (1989) 349.
- [3] J. Widany, Th. Frauenheim, Th. Kohler, et.al., *PHYSICAL REVIEW B*, 53 (1996) 8.
- [4] S. Nakano, M. Akaishi, T. Sasaki, et. al., *Mater. Sci.Eng. A* 209 (1996) 26.
- [5] R. H. Wentorf, *J. Chem. Phys.* 26 (1957) 956.
- [6] T. Endo, O. Fukunga, M. Iwata, *J. Mater. Sci.* 16 (1981) 2227.
- [7] S. Hirano, T. Yogo, S. Asada, S. Naka, *J. Am. Ceram. Soc.* 72 (1989) 68.
- [8] D.P. Yu, X.S. Sun, C.S. Lee, et al., *Appl. Physics. Lett.* 72 (1998) 1966.
- [9] W.Q. Han, Y. Bando, K. Kurashima, T. sato, *Appl. Phys. Lett.* 73 (1998) 3085.
- [10] Y.H. Xiong, C.S. Xiong, S.Q. Wei, et.al., *Applied Surface Science*, 253 (2006) 2515-2521.
- [11] E. Knittle, R.M. Wentzcovitch, R. Jeanloz, et.al., *Nature* 337 (1989) 349.
- [12] J. Widany, Th. Frauenheim, Th. Kohler, et.al., *PHYSICAL REVIEW B*, 53 (1996) 8.
- [13] S. Nakano, M. Akaishi, T. Sasaki, et.al., *Mater. Sci.Eng. A* 209 (1996) 26.
- [14] R. H. Wentorf, *J. Chem. Phys.* 26 (1957) 956.
- [15] P.X. Feng, H.X. Zhang, *Int Journal of Refractory Metals and Hard Materials* 27 (2009) 823-828.
- [16] H.X. Zhang, P.X. Feng, V. Makarov, B.R. Weiner, G. Morell, *Material Research Bulletin*, 44 (2009) 184-188.
- [17] M. Sajjad, H.X. Zhang, X.Y. Peng, P.X. Feng, *Phys. Scr.* 83 (2011) 065601 (4pp).
- [18] Takashi Taniguchi and Shinobu Yamaoka, *New Diamond and Frontier Carbon Technology*, Vol. 10 (2000) No.5.
- [19] L. Escobr-Alarcon, E. Camps, B. Rebollo, E. Haro-Poniatowski, M. A. Camacho-lopez, S. Muhl, *Superficies y Vacio* 11 (2000) 36-39.
- [20] H. Zeng, C.Y. Zhi, Z. Zhang, X. Wei, X. Wang, W. Guo, Y. Bando, D. Golberg, *Nano Lett.* 10 (2010) 5049-5055.
- [21] J. Yu, L. Qin, Y. Hao, S. Kuang, D.X. Bai, M. Y. Chong, W. Zhang, G.E. Wang, *ACS Nano* 4 (2010) 414-442.
- [22] Y.C. Zhi, Y. Bando, C.C. Tang, H. Kuwahara, D. Golberg, *Adv. Mater.* 21 (2009) 2889-2893.
- [23] W.J. Zhang, S. Matsumoto, *J. Mater. Res.* 15 (2000) 2677.
- [24] X. Y. Peng, M. Sajjad, J. Chu, B. Q. Yang, P. X. Feng, *Applied Surface Sciences* 257, 4795 (2011).
- [25] W.J. Zhang, S. Matsumoto, *Chemical Physics Letters* 330, 243 (2000).
- [26] R. Geick, C. H. Penny, and G. Rupprecht, *Phys. Rev.* 146, 543 (1966).
- [27] W. Fukarek, *Journal of Vacuum Science and Technology A: Vacuum, Surfaces and Films*, 19 (2001)2017-2024.
- [28] M.F. Plass, W. Fukarek, A. Kolitsch, et.al., *Thin Solid Films* 305 (1997) 172.
- [29] Cameron F. Abrams and David B. Graves, *J. Vac. Sci. Technol. A* 16(5) (1998) 3006-3019.
- [30] Hans Hofsas, Kun Zhang, *Appl. Phys. A* 92 (2008) 517-524.
- [31] M.F. Plass, W. Fukarek, A. Kolitsch, et.al., *Thin Solid Films* 305 (1997) 172.

- [32] M. Grunze, C.R. Brundle, D. Tomanek, Surf. Sci. 119 (1982) 133.
- [33] Smith, D. O. Appl. Phys. 30 (1959) 264.
- [34] Knorr, T. G. and Hoffman, R. W. Physical Review 113 (1959) 1039.
- [35] H. Hofsass, H. Feldermann, R. Merk R, et.al., Appl. Phys. A 66 (1998) 153.
- [36] P.X. Feng, X.P. Wang, H.X. Zhang, et al. J. Physics D: Appl. Phys. 40 (2007), 5239-5245.
- [37] S. Reich, A. C. Ferrari, R. Arenal, et.al., J. Phys. Rev. B 71 (2005) 205201.
- [38] J. Ye, H. Oechsner, S. Westermeyr, J. Vac. Sci. Technol. A 19(5) (2001) 2294.
- [39] O. Kutsay, C. Yan, Y.M. Chong, Q. Ye, I. Bello, W.J. Zhang, J.A. Zapien, Z.F. Zhou, Y.K. Li, V. Garashchenko, A.G. Gontar, N.V. Novikov, S.T.Lee, Diamond and Related materials 19 (2010) 968-971.
- [40] Huoping Xin, Yiqing Chen, Xiaohong Shi, Huaping Xu, Chenglu Lin and Shichang Zou, Thin Solid Films, 266 (1995) 173-175.
- [41] Cameron F. Abrams and David B. Graves, J. Vac. Sci. Technol. A 16(5) (1998) 3006-3019.



## **Chapter 7**

### **Summary and Future Work**

#### **7.1 Summary of Contributions**

The research presented in this thesis have contributed significantly towards advancing the current state of knowledge by providing unprecedented details on 2D nanomaterial: the dynamics of nanoscale material synthesis, atomic scale characterization, crystal structure evolution, free standing ultrathin nanosheets fabrication, nanoscale structure study, layered structure characterizations, structural modification, band-gap engineering of nanosheets and their applications from basic electronic to optoelectronic devices fabrications. The size, shape, thickness, density, and alignment of the BNNSs were well reported and explained in this thesis. The important advancements are briefly summarized in this section.

##### **7.1.1 Synthesis Ultrathin Boron Nitride Nanosheets**

Controlling experimental parameters and detecting the atomic layers BNNSs at molecular scale is of fundamental importance in realizing the next-generation of 2D nanomaterials systems. Unlike graphene, there was no established method to obtain large scale of single- or few-layer BNNSs. This deficiency has been removed in our current thesis research. We installed and upgraded CO<sub>2</sub>-pulsed laser plasma deposition system and introduced new experimental parameters that worked for us perfectly and we achieved large amount of high quality, few atomic layers boron nitride nanosheets at significantly low substrate temperature down to 300 °C and at short interval of deposition time (e.g. 3-5 sec).

Chapter 3 reported on a novel approach to synthesize nanosheets using short pulsed laser plasma deposition technique and control on plasma plume resulted in guided ions assisted layer-by-layer deposition of BNNSs with highest reported yields till date. The as synthesized sheets of BN monolayers exhibited extensively honeycomb rings which were utilized to interpret overall crystal structure, and also applied for nanomaterial device fabrication demonstrating their ability to act as excellent nano-templates. There were the first time ever reported studies on gas sensing properties and experimental approach for the fabrication of DUV sensor based on synthesized BNNSs and formation of their nano-constructs. This work has the potential to advance ongoing research efforts in 2D materials towards studying atomic thin sheets other than graphene from basic to advance applications.

With the variation of deposition parameters such as introducing background gas as deposition environment, we controlled the thicknesses of nanosheets, while quality and purity of the sample were still very high. For background gas, we chose  $H_2$  gas which transformed in to  $H^\pm$  ions and it effectively etched substrates from residual oxygen resulted in pure BNNSs formation. Beside successfully synthesized BNNSs, much attention was paid in crystal structure characterization. TEM characterized large area, flat and transparent BNNSs while, high resolution transmission electron microscopy (HRTEM) identified the sheets to be mostly defect-free and to have the characteristic honeycomb crystal lattice structure based on six-membered  $B_3-N_3$  hexagon. From HRTEM measurements, we clearly distinguished between the bright and slightly dull dots related to B and N atoms arranged in a typical honeycomb network structure, similar to C-C atoms in graphene. HRTEM, electron diffraction, X-ray diffraction, Raman scattering, fast Fourier transform and Fourier transform infrared spectroscopy clearly identified hexagonal BN structure.

In this thesis, we also revealed nanostructuring of composite BNNSs used to provide new electronic and optical functionalities. BNNSs were used to study their applications in different areas of nano-electronic device technology, e.g. fabrication of prototype Schottky diode, deep ultraviolet photo detector (DUV) and resistance based gas sensor. In the case of Schottky diode, carbon elements were used to functionalize BNNSs and current versus voltage characteristics of were recorded at different temperatures (25 °C, 50 °C, 75 °C) represented that doping in BNNSs brought a significant change in the output current of diode. BNNSs were also treated with hydrogen plasma, which exhibited distinct and pronounced changes in its electronic properties after the plasma treatment. The band-gaps of the few layers BNNSs reduced from  $\sim 5.6$  eV to  $\sim 4.25$  eV, which is a signature of transition from the insulating to the semi-conductive regime. It was concluded that with the engineered of 2D materials by attaching other atoms or molecules significantly changes electronic properties.

Data obtained from BNNSs-based DUV photo-detector device indicated that BNNSs are highly sensitive to deep UV light source. Response time and recover time were also estimated which are expected to be further shorter if we have digital control on several experimental parameters. Gas sensing properties of BNNSs-based gas sensor indicated that BNNSs are truly an effective material that can be used as resistance based gas sensor operates in extreme high temperature and toxic environment where properties of conventional sensors fall short. It is therefore summarized that BNNSs are highly attractive for range of applications in material science and nano-electronic device technology.

Similar to diamond like carbon, BN is also fashionable in cubic structure. In this thesis, we synthesized cubic BN films at significantly low substrate temperature (450 °C) using ferrous

oxide ( $\text{Fe}_2\text{O}_3$ ) nanoparticles as catalyst. While by using nickel and cobalt nano-particles as catalyst helped in producing BN nanotubes.

## **7.2 Future work**

In addition to these works, we propose to initiate a potential project on graphene and its twin BNNSs by designing a compact layer structure on detecting visible light using graphene-platform for photo-voltaic applications. The following sections present an overview of these projects.

### **7.2.1 Overview**

In this section we present the preliminary studies on a potential graphene work that revisits the sensitivity of graphene to visible region and applies it to detect the visible light.

BNNSs are receiving great research attention as a substrate material for high-performance graphene electronics because it has an atomically smooth surface, and lattice constant similar to that of graphene. Therefore, deposition of graphene on atomically flat layers of BNNSs for tunable electronic properties will be a potential project. In the first step, we will synthesize BNNSs via PLD technique. In the second step, BNNSs samples will be transferred to another chamber to deposit graphene using chemical vapor deposition method. BNNSs as substrate material will help to grow wrinkle free graphene on its surface and it will also improve charge transport properties in graphene. Graphene/BNNSs will provide relatively smooth surface, free dangling bonds and absence from charge traps. As BNNSs has similar lattice constant to that of graphene, it will tune its band gap that will lead graphene to several other electronic applications so far graphene lacks due to its zero band gap.

The single atom thick quasi planar sheets of graphene functions as an ultra-sensitive electrical platform due to the high carrier charge density and the low-scattering  $\text{sp}^2$ -bound-carbon

lattice-structure. The single atom thickness with a high density of p-electrons on the surface makes graphene ultrasensitive to surface events which can either change the carrier density or produce scattering sites. The interest is to functionalize graphene for device fabrication using BNNSs as substrate material and investigated the effect of nanoscale-scale material on the fundamental electrical properties of the base graphene by characterizing electronic and optoelectronic properties under visible light.

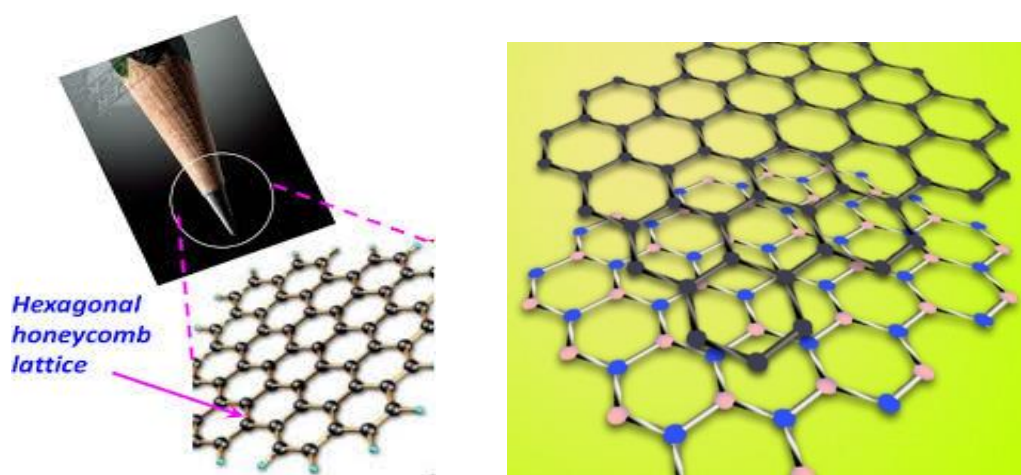


**Figure 7.1** Schematics illustration of graphene on BNNS.

Layered materials e.g. graphene [1-3] and BNNSs [4] are playing excellent role in a variety of key scientific fields including materials science, condensed matter physics, molecular electronics and spintronics, tribology, chemistry and solar cells. Graphene is receiving significant attention since 2004 when it was mechanically isolated into single atomic layers graphene [1]. The carbon (C) atoms in graphene are arranged in a 2D-planar hexagonal honeycomb crystal lattice structure (Figure 7.1) and are bounded together by strong covalent bonds ( $sp^2$  bonding), while weak van der Waals forces hold the layers together. On the other hand, BNNSs have been

considered a counterpart of graphene due to its similar crystalline structure and identical lattice parameter to that of graphene [1]. The compact nanostructures of these two material e.g. graphene/BNNSs will be an interesting approach towards new research based on 2D nanomaterials.

The objective of this work is to introduce new method to isolate 2D layered materials e.g. graphene on BNNSs for various electrical applications. The experimental set up is simple and cost effective, which satisfies the requirements of commercial applications. The development of creative and innovative methods and processes will be required for handling and integrating them into device architectures, which requires a fundamental understanding of the chemistry and physics of these materials in order to manipulate them as desired.

### **7.2.3 Existing Research**

BNNSs have been tested for numerous applications in electronics and optoelectronics. For example, BNNSs are considered an excellent dielectric material. Moreover, BNNSs have also been reported as superb substrate material for graphene based electronic devices. An example is shown in Fig. 7.2 in which significant increase in output current recorded when graphene deposited on BNNSs substrate [6].

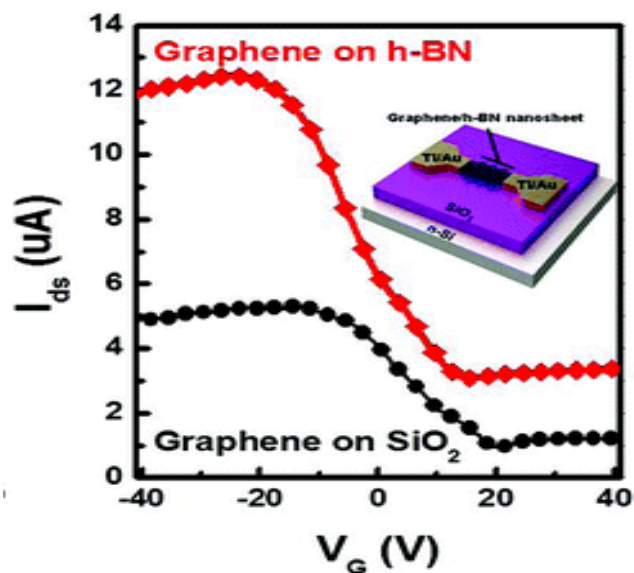


**Figure 7.2** I-V characteristics of graphene placed on  $SiO_2$  and BNNSs.

Large area BNNSs have been produced by using short pulsed laser produced plasma deposition (SSP-LPP) techniques. Based on the SSP-LPP technique, we previously synthesized various types of BNNSs structures as shown in Fig. 7.3 (a,b) [7].

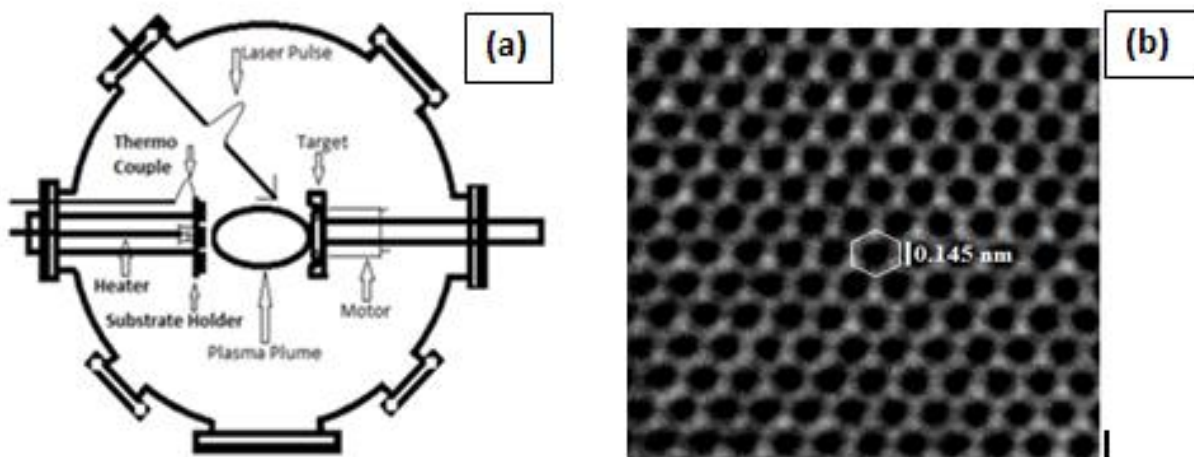


**Figure 7.3** (a) Schematic of SSP-LPP technique. (b) Electron microscopic images of BNNSs prepared by PLD technique.

### **7.3 Closing Remarks**

In principle, the family of 2D nanomaterials presents a gamut of perspectives that enable reexamination of older research problems and avenues of studying newer ones. The knowledge we have obtained in this work has significantly contributed to the evolving story on the science of 2D BNNSs. The results presented here are continuity of the research presented by other researchers and we have improved and expanded upon the work from synthesis to applications enclosed in this thesis. The application fields discussed here have been an extremely fruitful area of electronic and opto-electronics research and have expanded at a rapid pace. The 2D nanomaterial family discovered since the discovery of graphene and today it is a familiar territory over the wide research areas. Starting from the science of graphene that has introduced the most; recent research on other members BNNSs is the continuity of 2D materials and their applications.



## 7.4 References

- [1] K. S. Novoselov, A. K. Geim, S. V. Morozov, D. Jiang, Y. Zhang, S. and I. V. Grigorieva, A. A. Firsov, Electric field effect in atomically thin carbon films, *Science* 306, p. 666, 2004. doi:10.1126/science.1102896.
- [2] A. S. Mayorov, R. V. Gorbachev, S. V. Morozov, L. Britnell, R. Jalil, L. A. Ponomarenko, P. Blake, K. S. Novoselov, K. Watanabe, T. Taniguchi, A. K. Geim, Micrometer-scale ballistic transport in encapsulated graphene at room temperature, *Nano Lett.* 11, p. 2396, 2011. doi:10.1021/nl200758b.
- [3] J. Moser, A. Barreiro, A. Bachtold, Current-induced cleaning of graphene, *Appl. Phys. Lett.* 91, p. 163513, 2007. doi:10.1063/1.2789673.
- [4] Zeng H, Zhi C, Zhang Z, Wei X, Wang X, Guo W, Bando Y, Golberg D (2010) White Graphenes: Boron Nitride Nanoribbons via Boron Nitride Nanotube Unwrapping. *Nano Lett.* 10: 5049-5055. doi: 10.1021/nl103251m.
- [5] Kang Hyuck Lee, Hyeon-Jin Shin, Jinyeong Lee, In-yeal Lee, Gil-Ho Kim, Jae-Young Choi, and Sang-Woo Kim; *Nano Lett.*, 2012, 12 (2), pp 714–718; DOI: 10.1021/nl203635v.
- [6] M. Sajjad, G. Morell, and P. X. Feng. *ACS Appl. Mater. Interfaces* (May 2013) DOI: dx.doi.org/10.1021/am400871s.

## PUBLICATIONS

### Thesis Related Publications

- 1) **M. Sajjad**, W. M. Jadwisienczak, and P. X. Feng; *Nanoscale*, 2014, 6, 4577.  
“Nanoscale Structure Study of Boron Nitride Nanosheets and Development of Deep-UV Photo-Detector”  
DOI: 10.1039/C3NR05817D
- 2) **M. Sajjad**, G. Morell, and P. X. Feng. *ACS Appl. Mater. Interfaces* (May 2013) DOI: dx.doi.org/10.1021/am400871s  
“Advance in Novel Boron Nitride Nanosheets to Nano-Electronic Device Applications”
- 3) **M. Sajjad**, X. Y. Peng, J. Chu, H. X. Zhang, P. X. Feng, *J. Mater. Res.* Vol. 28, No. 0, 2013.  
“Design and Installation of CO<sub>2</sub>-pulsed laser plasma deposition system for the synthesis of mass product nanostructures”.
- 4) **M. Sajjad**, and X.P Feng, *Materials Research Bulletin* 49 (2013) 35–38.  
“Study the Gas Sensing Properties of Boron Nitride Nanosheets”
- 5) **M. Sajjad**, M. Ahmadi, M. J-F Guinel, Y. Lin, P. X. Feng. *J Mater Sci.* (2012); DOI 10.1007/s10853-012-7044-4  
“Large scale synthesis of single-crystal and poly-crystalline boron nitride nanosheets”.
- 6) **M. Sajjad**, P. X. Feng, *Appl. Phys. Lett.* 99 (2011).  
“Low temperature synthesis of cubic boron nitride films”
- 7) **M. Sajjad**, H. X. Zhang, X. Y. Peng, P. X. Feng, *Phys. Scr.* 83 (2011) 065601.  
“Effect of substrate temperature in the synthesis of BN nanostructures”.
- 8) P. X. Feng, **M. Sajjad**, *Materials Letters* 89 (2012) 206–208.  
“Few-atomic-layer boron nitride sheets synthesis and applications for semiconductor diodes”
- 9) P. X. Feng, H. X. Zhang, X. Y. Peng, **M. Sajjad**, and J. Chu, *Review of Scientific Instruments*. 82, 043303 (2011).  
“A novel compact design of calibration equipment for gas and thermal sensors”
- 10) P. X. Feng, **M. Sajjad**  
“Structures of atomic-thin boron nitride membrane” (under review in journal of *Nanotechnology*)
- 11) Feng, Peter; Sajjad, Muhammad; Li, Eric; Zhang, Hongxin; Chu, Jin; Aldalbahi, Ali; Morell, Gerardo,  
“Fringe Structures and Tunable Bandgap Width of 2D Boron Nitride Nanosheets" (Under review in *ACS Applied Materials & Interfaces*)

### Other Publications

- 1) Jin Chu, Xiaoyan Peng, **M. Sajjad**, Boqian Yang, Peter X. Feng, *Thin Solid Films* 520 (2012) 3493–3498. “Nanostructures and sensing properties of ZnO prepared using normal and oblique angle deposition techniques”
- 2) X.Y. Peng, **M. Sajjad**, J. Chu, B. Q. Yang, P. X. Feng, *Applied Surface Science*, 257 (2011) 4795–4800.  
“Studies of structural evolution and sensing properties of ZnO nanocrystalline films”.

- 3) Xiaoyan Peng, Jin Chu, Sajjad Muhammad, Peter Feng, *International Journal of Material Research*, (2012), DOI: 10.3139/146.110749.  
“Study of the structural evolution of crystalline zinc oxide films prepared by PLD technique”,

#### CONFERENCE PROCEEDINGS

- 1) M. Sajjad, P. X. Feng,  
“Electron microscopic characterization of multi-layer boron nitride nanosheets” *MRS Online Proceedings Library*, Volume 1549/2013, Copyright © Materials Research Society 2013 DOI: <http://dx.doi.org/10.1557/opl.2013.859>
- 2) M. Sajjad, H. X. Zhang and P.X. Feng, *MRS Online Proceedings Library*, Volume 1307/mrsf10-1307-cc05-13.  
“Synthesis and Comparison of BN nanostructure prepared on Si and Mo substrates by Laser Plasma Deposition Technique”.
- 3) H. X. Zhang, M. Sajjad, and P. X. Feng, *MRS 2010 Proceeding of Spring Meeting*, San francisco, April.5-9, 2010. Paper #: 1259-S14-10 DOI: 10.1557/PROC-1259-S14-10)  
“Growth, Characterization, and Comparisons of Few-layer Boron Nitride and Graphene Sheets”